THE STRATOSPHERIC SOLAR AUREOLE

by

John Allen Eddy

B.S., United States Naval Academy, Annapolis, Maryland, 1953

A thesis submitted to the Faculty of the Graduate School of the University of Colorado in partial fulfillment of the requirements for the Degree

Doctor of Philosophy

Department of Astro-Geophysics

1961

This Thesis for the Ph.D. degree by

John Allen Eddy

has been approved for the

Department of

Astro-Geophysics

by

_____

_____

Date _____

ACKNOWLEDGMENTS

Every phase of the work of this thesis was supported financially by the Office of Naval Research under contract Nonr-393(05). The project director was Dr. Gordon Newkirk, who was also my thesis advisor. I am indebted to him for the opportunity to assist in the Coronascope project and for patient help and direction for a period of more than four years.

My graduate study in Astro-Geophysics was made possible by fellowships from the High Altitude Observatory, sponsored in part by the Institute for Solar-Terrestrial Research and the Ford Foundation. I also held tuition scholarships from the Graduate School of the University of Colorado. I am grateful for the opportunity this gave me to work toward the Ph.D. degree.

The success of the Coronascope experiment was due largely to the unselfish and untiring work of the HAO team that spent the summer of 1960 in Minneapolis. Christiaan Heynekamp, Howard Hull, Robert Lee, Charles Garcia, James Robb, and Robert Cooper were members of this group. Equally important was the long and masterful shop work of Leon Lacey and others on the HAO staff in Boulder.

The pointing frame used for our balloon flights was generously loaned to the High Altitude Observatory by Princeton University. I am also indebted to Prof. Martin Schwarzschild and the Princeton Observatory balloon group for the opportunity of working with them on one of the Stratoscope I flights in the summer of 1959.

The Coronascope flights were conducted by General Mills, Inc. of Minneapolis; I thank the personnel of the balloon division for their part in the success of the experiment.

I am deeply grateful to Prof. Zdenek Sekera of the University of California for his understanding advice and kindly personal interest in my thesis, and for providing his table of Rayleigh calculations in card form for computer use.

David Lewis and Jim Winkelman wrote and carried out the computer program for the Rayleigh interpolation on the CDC-1604 computer at the National Bureau of Standards. The Mie calculations were performed on the IBM-1620 computer made available to me by the National Center for Atmospheric Research. I thank Miss Astrik Deirmendjian for her help in using this computer.

Prof. Walter Roberts, Prof. Bernhard Haurwitz, and Prof. Julius London advised me in the writing of my thesis and read the first drafts. I sincerely appreciate the time and help they gave me.

I am obligated to Mrs. Barbara Hill for the care and speed with which she typed the final copy. As a special and undeserved favor to me she doubled her regular workload in order to type my thesis.

Finally I acknowledge the indispensable assistance of my wife, Marjorie, for assistance in the work of this thesis and for many years of patient encouragement and support.

ABSTRACT

Two unmanned balloon flights in the autumn of 1960 obtained the first observations of the solar aureole at stratospheric altitudes. The purpose of this thesis is to report the spectral observations obtained on one of these flights and to interpret them in terms of atmospheric aerosol content.

The theory of light scattering by small particles is summarized to develop the formulae needed to interpret the aureole data. Included are the Rayleigh law for small particles, the Chandrasekhar solution of the planetary scattering problem, and the Mie theory for large particle scattering. The apparatus employed in the balloon experiment is described in some detail; the principal instrument is an external occulting coronagraph called the flying coronagraph. The spectral observations are presented and described, and the limits of accuracy are discussed. Observations cover the wavelength range from 0.37μ to 0.79μ, at the scattering angle 2°.4, and over the altitude range from 42,000 ft. to 80,000 ft. The data are interpreted in terms of two atmospheric scattering components: a Rayleigh component due to atmospheric molecules, and a Mie component due to spherical aerosols. The Rayleigh contribution is calculated for each observed brightness point using the tables of Coulson, Dave, and Sekera. The difference between the observed and Rayleigh brightness is called the residual brightness and is interpreted as due to scattering by a size distribution of aerosols above the point of observation. A residual brightness is found at all altitudes which is 30% or more of the theoretical Rayleigh brightness. Families of non-unique particle distributions are found that satisfactorily explain the observations. The

allowed particle size distributions are expressed as $dN(a)/d\log a = a^{-\delta}$, where N is the particle population and a is the particle radius. The data indicate values of $\delta = 8$ or larger. This finding is supported by recent aerosol sampling measurements of Junge and Manson; it contradicts earlier estimates that proposed $\delta = 3$. The findings of this study suggest that the form of the particle size distribution changes with altitude, becoming a steeper function of particle radius at higher altitudes. One of the allowed particle distributions is interpreted in terms of micrometeorites and an upper limit of meteoric flux is derived.

TABLE OF CONTENTS

TABLE OF CONTENTS (cont.)

LIST OF FIGURES

CHAPTER II

CHAPTER III

CHAPTER IV

LIST OF FIGURES (cont.)

CHAPTER V

LIST OF FIGURES (cont.)

CHAPTER V (cont.)

LIST OF TABLES

CHAPTER I

CHAPTER II

CHAPTER III

CHAPTER IV

CHAPTER V

CHAPTER I

Introduction

"It is notable that the atmosphere, which was of a perfect purity near the earth, was grey and misty above our heads, and the beautiful blue sky seen from the surface did not exist for us, although the weather was calm and serene, and the day the most beautiful that could be. The sun did not seem dazzling to us, and its heat was diminished owing to our elevation." Thus Robertson described the brightness of the sky he saw from the basket of a balloon 20,000 feet over Hamburg on a summer morning in 1803 (Marion, 1874). His observation was of dubious value, however, since he was only partly conscious when he made it. It was, nevertheless, the first observation of the sky at that great altitude.

A summary of more recent and quantitative measurements of high-altitude sky brightness is given in Table 1 at the end of this chapter. Several of them, such as those of Luckiesh that were made with "a compact instrument of special design which need not be described", are of little more value than the recollection of Robertson. Many are only relative measurements. Only four represent observations made near the disk of the sun, and, of these, none was made above the tropopause. There is a good reason why sky brightness observations near the sun are of unique value, and an equally good reason why few have been made.

The sky in the vicinity of the sun exhibits a sharp increase in brightness, beginning at an angular distance of about 10° from the sun and increasing up to the limb; within this halo of brightness the blue of the sky changes to white. This phenomenon is the solar aureole. It is the manifestation of forward scattering of sunlight by non-molecular particles that lie near the line-of-sight of the sun. The glow around a streetlamp on a foggy night is a good example of an aureole, though

caused by somewhat larger particles. The non-molecular particles that explain the solar aureole are atmospheric aerosols. In size these particles range between molecules and cloud droplets; they may be of terrestrial or meteoric origin. Particles of aerosol size scatter incident radiation predominantly forward, and they scatter all wavelengths with nearly equal efficiency --- hence the small diameter and white color of the aureole. Particles of smaller, molecular size scatter with weaker angular preference and favor the short wavelengths; they produce the blue background sky. In a polluted atmosphere the aureole is pronounced, while in the purer, high-altitude air it is less distinct. In an atmosphere composed only of gaseous molecules there would be no aureole. As a consequence the aureole is a sensitive indicator of the aerosol content of the atmosphere. Deirmendjian (1957, 1959) has given a thorough discussion of the theory of the aureole and its relation to atmospheric turbidity. The aureole brightness at a given height in the atmosphere gives evidence of all particles above that height, including those in the highest atmospheric regions. Moreover, by observing the aureole at a number of different altitudes we can differentiate the observations and obtain a particle height distribution. Thus the study of the aureole and its altitude variation can give valuable information on the particulate matter in the upper atmosphere.

Observations of the aureole are difficult to make, and for this reason there are few data available. The difficulty stems from the large brightness difference between the aureole and the adjacent solar disk. At low altitudes the sun is at least a million times brighter than the aureole; in the stratosphere it is a hundred million times brighter. If any of the direct solar rays enters the measuring device the aureole

brightness will be swamped in sunlight that is scattered in the instrument. The problem might be compared to filling a thimble from Niagara Falls without getting your hand wet. Fortunately, it is not that hopeless, and a number of clever optical devices have proven successful for ground measurement of the aureole. Van de Hulst (1952) gives early data obtained by Rosenberg, Dorno, and De Jong. More extensive measurements are given by Volz (1954) and by Volz and Bullrich (1961). Newkirk (1956) used a modified Lyot coronagraph to make observations from sites in the Rocky Mountains. Recently, Sekihara and Murai (1961) have obtained aureole measurements with a spectrophotometer in Japan.

The problem of measuring the aureole becomes more difficult when one considers airborne observations. The necessity of guiding the instrument accurately for long periods under adverse circumstances presents a serious complication. To the Niagara Falls problem is added the handicap of going over the falls in a barrel, filling the thimble, and still keeping dry! The first aureole measurements from above the ground were made by Evans (1948a) who aimed a hand-held coronagraph at the sun through a hole in the side of an airplane while he visually estimated the brightness. The second attempt at high-altitude aureole measurements was made from a manned balloon (Cooper, Eddy, and Newkirk, 1960); on this flight R. H. Cooper pointed a photographic modification of the Evans instrument from an open gondola at 38,000 feet.

The third attempt is reported in this thesis. It involved the use of an unmanned and automatic coronagraph that was carried by balloon to an altitude of 80,000 feet. Two balloon flights, under the name Project Coronascope, were made from Minneapolis in the autumn of 1960. The project was sponsored by the Office of Naval Research and directed by Dr. Gordon A. Newkirk. The Coronascope flights were successful in

obtaining, accurately, and over a considerable height range, the first measurements of the stratospheric aureole. It is significant that these data were secured two years after the start of the nuclear test ban, at a time when the upper atmosphere was in its "natural" state, essentially free of anthropogenic particles. I have reduced and interpreted the Coronascope measurements of the spectral brightness of the sky; Dr. Newkirk is carrying out the analysis of the angular scattering data. The combined analysis will be published as a separate report.

The purpose of this thesis is to present the Coronascope spectral observations, to explain how they were obtained, and to interpret them by means of the theory of light scattering.

My thesis is primarily observational. The number of months spent interpreting the observations is approximately equal to the number of years spent gathering them. I feel that my interpretation adds interesting new material in fields where it is sorely needed; yet the real value in this work is in the data themselves. I hope they will see other use; they were taken from the sky at no small cost.

Table 1. Day Sky Brightness Measurements above Sea Level

Reference	Altitude (Thousands of feet)	Angle from sun (degrees)	Wave-length (microns)	Field of Scan (degrees)	Method	Scale*	Vehicle
Measurements far from the sun:							
Luckiesh (1919)	0-20	Various	White	?	Visual	Relative*	Aircraft
Teele (1936)	0-72	Various	White	10	Photoelec.	Relative	Balloon
Tousey and Hulbert (1947)	0-20	8	White	4	Photoelec.	Absolute*	Aircraft
Hulbert (1948)	0-10	Various	White	?	Visual	Absolute	Aircraft
Packer and Lock (1950)	18-38	15-60	.35-.67	2.5	Photoelec.	Relative	Aircraft
Miley, Cullington, and Bedinger (1953)	328-440	Various	.42-.64	?	Photoelec.	Relative	Rocket
Berg (1955)	244-720	Various	Red,Blue	5	Photographic	Relative	Rocket
Boileau (1960)	20	Various	White	5	Photoelec.	Absolute	Aircraft
Duntley, Boileau, Gordon, and Harris (1960)	6-20	Various	White	5	Photoelec.	Absolute	Aircraft
Stakutis (1960)	0-90	Various	White	12,180	Photoelec.	Absolute	Balloon
Wallace (1961)	0-124	Various	.30-.90	12	Photographic	Relative	Balloon

Table 1. (cont.) Day Sky Brightness Measurements above Sea Level

Reference	Altitude (Thousands of feet)	Angle from sun (degrees)	Wave-length (microns)	Field of Scan (degrees)	Method	Scale*	Vehicle
Measurements near the sun:							
Evans (1948a)	0-30	2	White	6	Visual	Absolute	Aircraft
Volz (1954)	0,6.5	0.2-120	0.3-0.8	<1	Photographic and Photoelec.	Absolute	(Ground)
Newkirk (1956)	5-12	0.25-3	0.4-0.83	<1	Photographic	Absolute	(Ground)
Cooper, Eddy, and Newkirk (1960)	38	2	0.54	<1	Photographic	Absolute	Balloon

*Relative: brightness measurements of one point in the sky relative to another.

*Absolute: brightness measurements of sky points relative to the brightness of the sun or to a standard lamp.

CHAPTER II

THEORY OF LIGHT SCATTERING

A. Introduction

1. Historical Summary

Why is the sky blue? Middleton (1960) has given some interesting answers from the history of science: Leonardo da Vinci suggested the filtering of outer darkness by white air; Clausius proposed scattering of sunlight by atmospheric water bubbles; Chappuis called on ozone. The correct answer was given by Lord Rayleigh in 1871, who explained the day sky brightness as sunlight scattered by molecules of atmospheric gases. Although others had proposed the same explanation before Rayleigh, he was the first to give it mathematical formulation and to study the phenomenon in detail. Rayleigh's law, as it has come to be known, explains the scattering of light by a particle whose dimensions are much smaller than the wavelength of the incident light. The complex problem of radiative transfer in a planetary atmosphere that scatters according to the Rayleigh law was solved by Chandrasekhar (1950); his solution gives an exact description of the brightness and polarization of a pure molecular atmosphere in which radiation is scattered without being absorbed. Recently Coulson, Dave, and Sekera (1960) have published an extensive table of numerical calculations of the Rayleigh-Chandrasekhar solution. Approximate solutions that allow for absorption have been given by Dave and Sekera (1959), Larsen (1959), and Sekera and Dave (1961).

Scattering by larger, non-molecular, spherical particles (including aerosols) is explained by the theory published in 1908 by Mie. The combined problem of Rayleigh and Mie scattering in a turbid atmosphere has been discussed by many authors (van de Hulst, 1952; Volz, 1954; Deirmendjian and Sekera, 1956; Deirmendjian, 1957, 1959; Sekera, 1957; Kano, 1958),

although no exact solution has been given. Sky brightness observations can be explained satisfactorily in terms of the Rayleigh-Chandrasekhar theory with an additive correction for Mie scattering. My interpretation of the aureole brightness in Chapter V uses this method.

In this chapter I shall review the Rayleigh law, the Chandrasekhar solution, and the Mie theory to present the formulae that will be used to explain the observed sky brightness in Chapter V. I shall not discuss the mathematical formulation since it can be found in many textbooks; my references were Chapters 1, 4, 6, and 9 of van de Hulst (1957); Chapter 10 of Chandrasekhar (1950), and Chapter 13 of Born and Wolf (1959).

There is no standard notation used in the literature of light and radiative transfer. The symbols that I have adopted in this and subsequent chapters are defined and summarized in Appendix I; they are in general the symbols with c.g.s. units used by van de Hulst (1957). In discussing the observations, however, I have used kilofeet to express altitude (1 kft. = 1000 feet), since our altimeter was calibrated in feet. A conversion scale (kilofeet to kilometers) is given inside the back cover.

2. Definitions

Scattering is one form of the extinction of light; another form is absorption. As used here scattering is the diffusion or redistribution of a beam of light without change in wavelength; absorption is the conversion of light to another form of energy. Both processes attenuate a light beam in its passage through a medium. Scattering can change the wavelength distribution of a light beam by selectively diffusing certain quanta more than others. As used here scattering does not include the

change in frequency of an incident wave caused by quantum transitions within the scattering molecules (Raman effect).

Before we can consider scattering by a group of particles we must inquire about collective scattering effects. If interference phenomena link the scattering of adjacent particles, these phenomena must be considered in a rigorous scattering theory. The Rayleigh and Mie theories are based upon the assumption of independent scattering: this implies that individual particles are sufficiently far apart to preclude permanent systematic relations between the phases of light scattered by each of them. In this case the intensities of scattered light can be added without regard to phase. Van de Hulst (1957) gives the following criterion for this condition: independent scattering prevails if the mutual distance between particles is at least three times their radii. For atmospheric molecules and aerosols this condition is easily fulfilled; for certain colloidal solutions it is not. The classification of scattering as independent or dependent should not be confused with the classification as single or multiple, which distinguishes between two kinds of independent scattering. Table 2 outlines the difference. In the table, d is the interparticle distance, a is the particle radius, and τ is the scattering optical depth.

Table 2

Scattering Classification	Meaning	Criterion (acc. to van de Hulst)
INDEPENDENT	Particles are far enough apart to cancel systematic phase relations between waves scattered by adjacent particles	$d \geqslant 3a$
DEPENDENT	Scattering is by cooperative effects of particles, and depends upon phase relations between scattered waves	$d < 3a$
SINGLE	Each particle is exposed to only the unscattered incident beam	$\tau < 0.1$
MULTIPLE	A large part of the light reaching individual particles has suffered scattering by another particle.	$\tau \geqslant 0.1$

The Rayleigh-Chandrasekhar theory discussed in Section B treats independent, multiple scattering. The Mie scattering discussed in Section C is independent, single scattering.

B. The Rayleigh Law and Chandrasekhar's Solution

1. The Rayleigh Law

The name Rayleigh scattering has been given to the restricted case in which the linear dimensions of the scattering particle are much smaller than the wavelength of the incident light. This restriction allows one to treat the scattering particle as exposed to a homogeneous field; the variation of the field across the particle in a given instant need not be considered. The scattering can be described in this case using basic electromagnetic principles. The incident light wave, considered as an electric field, induces a dipole moment in the scattering particle. The particle then reradiates the energy, behaving as an oscillating dipole. If the particle is homogeneous and if the incident light is unpolarized, the intensity of the reradiated field at a distance r and scattering angle Θ from the incident direction can be described by

$$I = \frac{8\pi^4 |\alpha|^2 (1 + \cos^2 \Theta)}{\lambda^4 r^2} I_o \qquad (1)$$

where α is the polarizability of the particle, I_o is the incident intensity, and λ is the wavelength of the incident light. Equation (1) is a statement of the Rayleigh law. We see that the illuminance scattered according to the Rayleigh law is inversely proportional to the fourth power of the wavelength and that the angular dependence is expressed by the phase function $(1 + \cos^2 \Theta)$.

The Rayleigh size restriction, written in terms of particle radius a and particle refractive index m, is

$$2\pi a |m| \ll \lambda$$

or

$$x |m| \ll 1 \qquad (2)$$

where $x = 2\pi a/\lambda$ is the particle size parameter. Penndorf (1960) has shown that the upper size limit of the Rayleigh law for all refractive indices is $x = 0.5$. Hence for the spectral region covered in my study (0.37 - 0.79 μ) we can apply the Rayleigh law to any particle whose radius is less than 0.03 μ. This includes all atmospheric molecules as well as very small aerosols.

Equation (1) gives Rayleigh's law for the intensity of light scattered by a single particle or molecule. The formulation for the case of an atmosphere composed of many particles is, of course, much more complex. If the scattering process is single scattering we can express the total scattered intensity by a simple sum of terms like (1). The more general case is multiple scattering, for which the methods of the theory of radiative transfer are required. Since the multiple Rayleigh scattering theory has been solved in numerical form (Coulson, Dave, Sekera, 1960) I have used the multiple scattering theory in the interpretation of the Coronascope data.

2. Chandrasekhar's Solution of the Planetary Scattering Problem

Chandrasekhar (1950) applied the Rayleigh law to a sunlit planetary atmosphere to specify the intensity and polarization of emergent sky radiation. His solution, given in the form of an intensity vector whose components are the four Stokes parameters, is for the case of observations made in a direction specified by a zenith angle Z (or $\mu = \cos Z$) and an azimuth angle ϕ. The direction of the solar radiation is specified by $\mu_o = \cos Z_o$ and $\phi_o = 0$. The ground beneath the observer is assumed to reflect radiation according to Lambert's law of reflection with an albedo A. The optical depth at the point of observation is specified by τ. Figure 1 gives an illustration of the planetary scattering

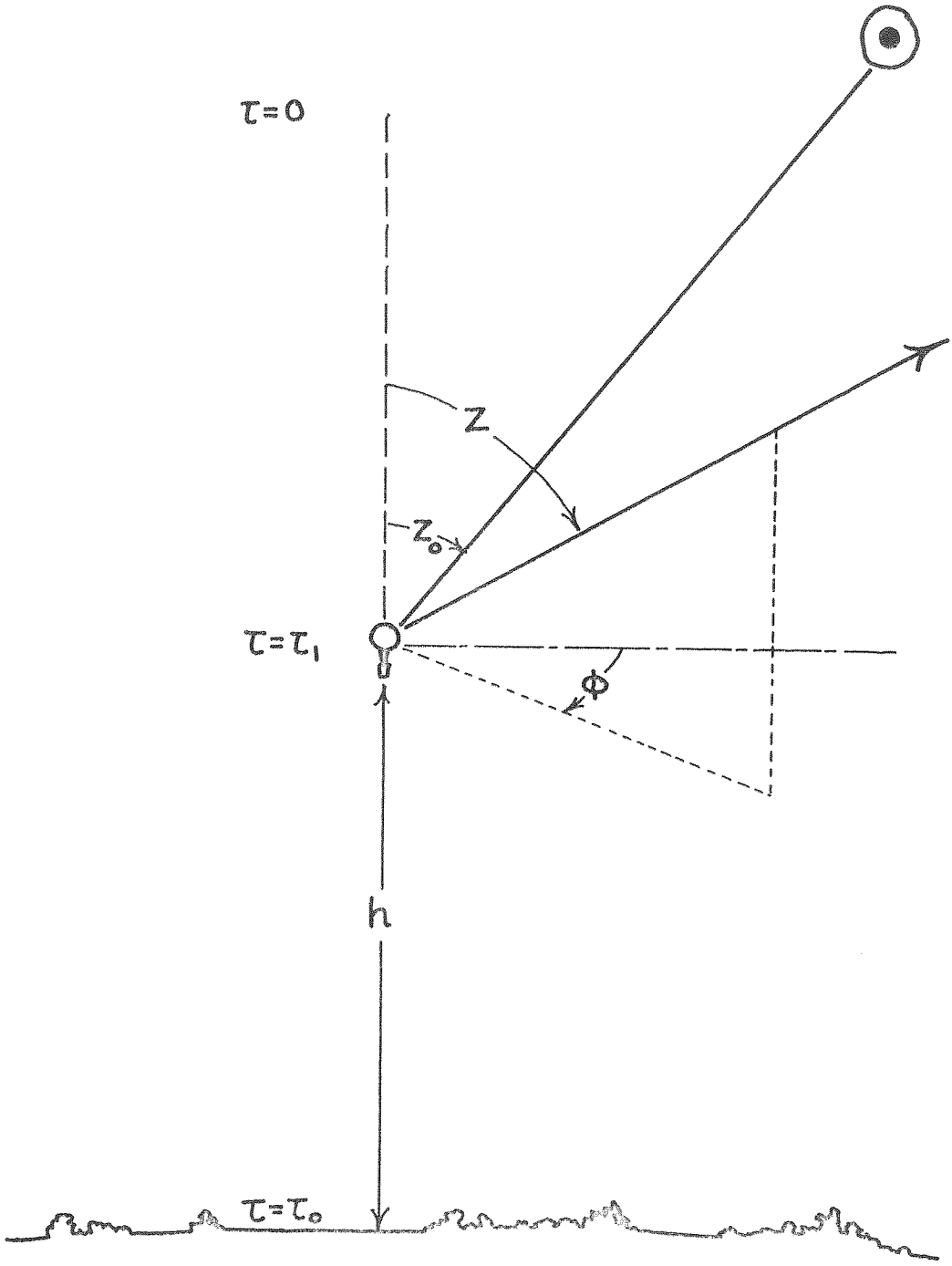

Figure 1

The planetary scattering problem for an elevated observer.

problem for the case of an elevated observer at height h above sea level. The atmosphere is assumed to be a plane-parallel medium in which radiation is scattered according to Rayleigh's law without being absorbed.

Chandrasekhar uses an equation of transfer,

$$\mu \frac{dI}{d\tau} = I - J \tag{3}$$

to describe the change of sky intensity, I, with optical depth, τ, in the atmosphere. The source function, J, is divided into two parts: one describes the multiple scattering of skylight and the ground reflection; the other component describes the direct solar flux as attenuated by the atmosphere. Chandrasekhar's solution of the transfer equation is given in the form of functions that satisfy four sets of simultaneous, non-linear, integral equations.

The first complete numerical calculation of the Chandrasekhar solution was published in 1960 by Coulson, Dave, and Sekera. Their method of solution was to solve Chandrasekhar's integral equations for a wide range of conditions by a technique of successive approximations. Their results are given as numerical values of the Stokes parameters of emergent sky radiation, tabulated as a function of selected values of the five arguments τ, μ_o, μ, ϕ, and A. The solution tabulated is for the case of an atmosphere illuminated at the top by a net flux πF_o of parallel, unpolarized solar radiation, where $F_o = 1$. The point of solution in the atmosphere is fixed by the optical depth, τ, a function of height and of wavelength. The direction of observation is fixed by μ_o, μ, and ϕ. For observations made above the earth the albedo A must be defined as the combined reflectivity of the ground and atmosphere beneath the observer.

I have used the Coulson, Dave, and Sekera calculations to obtain the background Rayleigh sky brightness in my interpretation of the Coronascope observations, discussed in Chapter V. The relation between the observed brightness and the tabulated intensity is derived below.

The photometric measurements of the aureole made by the Coronascope instrument are in units of sky brightness, B (ergs $cm^{-2} sec^{-1} steradian^{-1}$), relative to the mean brightness $B_\odot$ of the solar disk at the point of observation and at a given wavelength. Coulson, Dave, and Sekera tabulate a total sky intensity or illuminance, I (ergs $cm^{-2} sec^{-1}$) that results from an extraterrestrial solar illuminance of π ergs $cm^{-2} sec^{-1}$.

The apparent brightness of the sky, B, measured by a photometer that accepts radiation from a solid angle ω_{inst} is related to the sky illuminance I by

$$B = \frac{I}{\omega_{inst}} \tag{4}$$

The apparent brightness of the sun, $B_\odot$, measured by the same instrument at a point in the atmosphere where the optical depth is τ and at a time when the solar zenith distance is Z_o is

$$B_\odot = \frac{I_\odot \; e^{-\tau/\mu_o}}{\omega_{inst} \; \omega_\odot} \tag{5}$$

where $I_\odot$ is the illuminance incident on the top of the atmosphere and where $\omega_\odot$ is the solid angle subtended by the sun at the point of observation. Hence the ratio of sky to sun brightness measured by the photometer is

$$\frac{B}{B_\odot} = \frac{I \; \omega_\odot \; e^{\tau/\mu}}{I_\odot} \tag{6}$$

Since Coulson, Dave, and Sekera take $I_{\odot} = \pi$, the relation between observed brightness and their tabulated intensity is

$$\frac{B}{B_{\odot}} = \frac{I\ \omega_{\odot}\ e^{\tau/\mu_o}}{\pi} \tag{7}$$

C. The Mie Theory

1. Single Particle Theory.

Scattering of light by particles of size larger than the Rayleigh limit must be treated by rigorous optical methods. Light that is incident on a large particle does not constitute a homogeneous field as in the Rayleigh theory; individual rays of the incident beam must be considered, and the shape of the particle becomes an important parameter of the problem. The scattering theory employed in the large particle case must allow for the reflection and refraction of individual geometrical rays as well as diffraction effects.

A general solution of the problem of scattering by large particles was given in 1908 by Mie. The scattering theory derived by Mie applies to homogeneous particles of spherical shape and arbitrary size; for very small particles it is approximately equivalent to the Rayleigh law.

Since the Mie theory is restricted to spherical particles we must ask at the outset if it is indeed applicable to scattering by aerosols. The answer is yes, for reasons given below:

a. Practically all stratospheric aerosols are less than one micron in radius (Junge and Manson, 1961); possible error due to the spherical approximation is least for small radii.

b. A spherical shape is a reasonable approximation for randomly oriented microscopic particles whose exact shapes are unknown.

c. Atmospheric optical phenomena such as rainbows, the glory, and the aureole, that result from aerosols can be explained by the spherical particle theory (Minnaert, 1954; van de Hulst, 1957).

d. Aerosols that are of meteoric origin can be expected to be spherical due to melting and to random erosion in space.

Mie's theory presents an expression for the intensity scattered by a homogeneous isotropic particle that is exposed to an incident monochromatic plane wave. It presents an exact solution of Maxwell's equations for the scattered field at a point far from the scattering particle. The point of solution is defined by a scattering angle Θ and a radius vector r, which is measured from the scattering particle.

For the case of unpolarized incident light of intensity I_o, the scattered intensity or illuminance I in a direction Θ is given by the Mie theory as

$$I(\Theta) = \frac{\sigma_\Theta (m,x)}{r^2} I_o \qquad (8)$$

where σ_Θ is the angular Mie scattering cross section of a particle of refractive index m and size parameter $x = 2\pi a/\lambda$. The dimension of σ_Θ is cm^2 $steradian^{-1}$. It is defined in such a way that the energy scattered by a particle in a direction Θ equals that incident on an area σ_Θ. Figure 2 shows values of $\log \sigma_\Theta$ as a function of particle radius a for m = 1.33 and $\Theta = 2^{\circ}.4$ for the wavelengths used in my study.

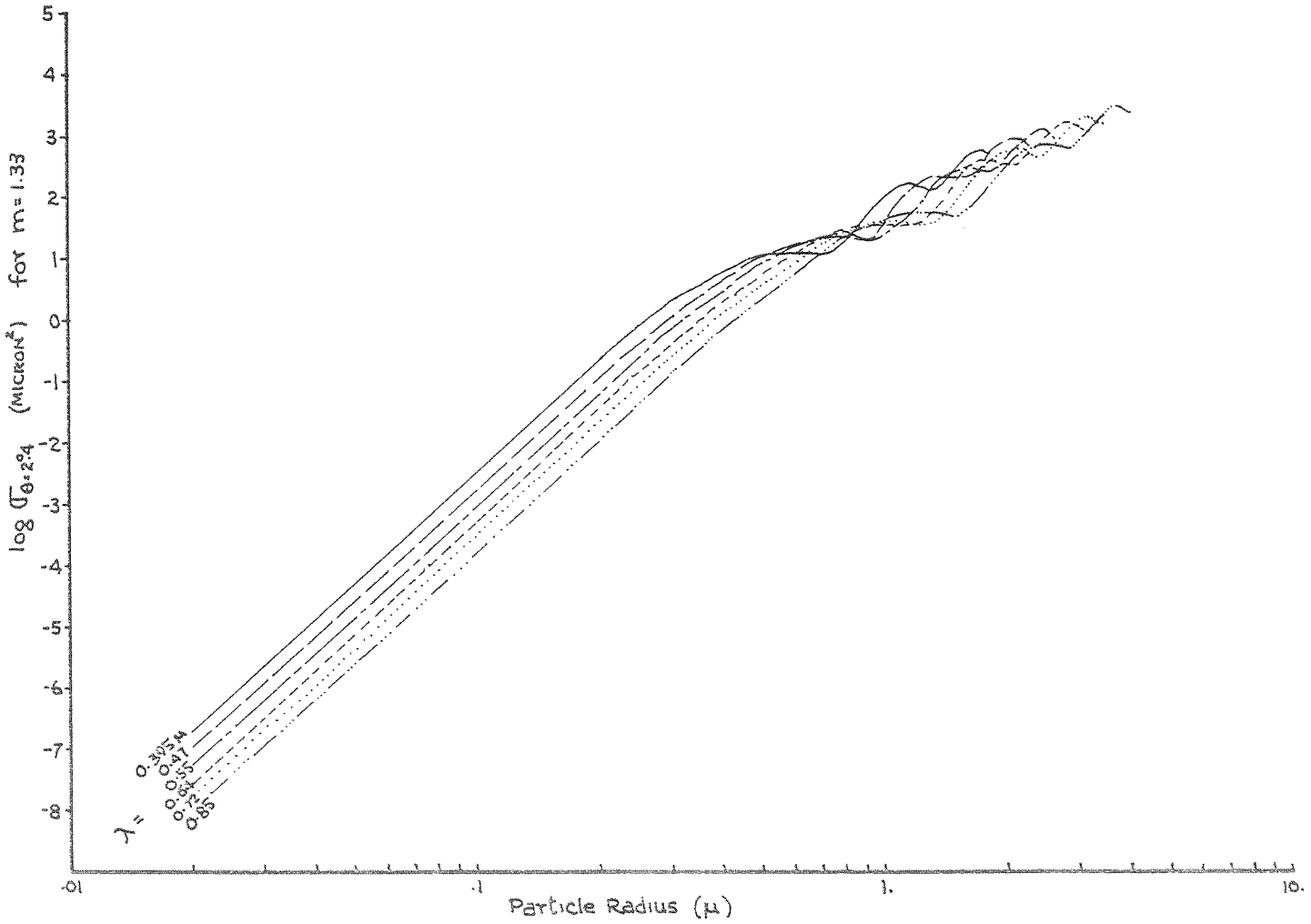

Figure 2

Angular Mie scattering cross sections for m = 1.33 and $\theta = 2^{\circ}4$ (Penndorf, 1954a)

Computations of the function σ_Θ exist in the literature for a range of arguments Θ, x, and m. A bibliography of published numerical Mie coefficients is given on pages 167-171 of van de Hulst (1957); it includes work done through 1957. The Mie coefficients that I have used were taken from Penndorf (1954a, 1960).

The treatment of large-particle scattering in Chapter V uses the Mie theory for spherical particles. Further, I have considered only the case of single scattering, a simplification that is justified by the small optical depths and low particle concentrations in the stratosphere. In the single scattering approximation we consider only the direct solar flux on the atmospheric particles. This direct flux provides by far the predominant illumination on aerosols; moreover, the predominance of the direct illumination is further enhanced in our case since in the aureole we observe forward Mie scattering.

2. Sky Brightness due to Mie Scattering

Consider a small element of unit volume in the atmosphere in which there are N identical Mie particles, each of which scatters the incident solar illuminance I_o according to the relation (8). Then, according to the assumption of single scattering, the total illuminance scattered by the unit volume will be

$$I\ (\Theta,m,x) = \frac{\sigma_\Theta(m,x)}{r^2}\ I_o\ N \qquad (9)$$

Suppose now that a photometer is at a distance r from the scattering element. The unit scattering volume subtends a solid angle $\omega = 1/r^2$ at the photometer. The photometer itself accepts radiation from a solid angle $\omega = \omega_{inst}$. The brightness, B (ergs $cm^{-2} sec^{-1} steradian^{-1}$) detected

by the photometer is

$$B(\theta,m,x) = \frac{I(\theta,m,x)}{r^2\ \omega_{inst}}$$

or

$$B(\theta,m,x) = \frac{\sigma_\theta(m,x) I_o N}{\omega_{inst}} \qquad (10)$$

Now consider the case shown in Figure 3. A photometer is at the point 0, which is defined by a height h_o above sea level and an optical depth τ_o. The solar zenith angle is Z_o. The azimuth angle of the sun is immaterial. We seek an expression for the brightness of scattered light that reaches the photometer from a direction defined by a zenith angle Z and an azimuth angle ϕ from the solar meridian. The direction of observation is the line OP; it does not necessarily lie in the zenith-observer-sun plane. The azimuth angle ϕ is equivalent to the scattering angle θ for directions near the sun and for particles within the terrestrial atmosphere, to the extent that solar rays can be considered to strike the atmosphere in parallel paths. For the remainder of this derivation we take $\theta = \phi$.

The point Q lies on OP at a height h where the total optical depth is τ. Imagine a volume element at Q which has unit cross section normal to the solar direction. Its length along the solar direction is dS cm.; its volume is dS cm^3. The solar illuminance incident on the unit area face of the volume element is

$$I_o' = I_o e^{-\tau \sec Z_o} \qquad (11)$$

where the unprimed I_o expresses the solar illuminance incident on the top of the atmosphere ($\tau = 0$.)

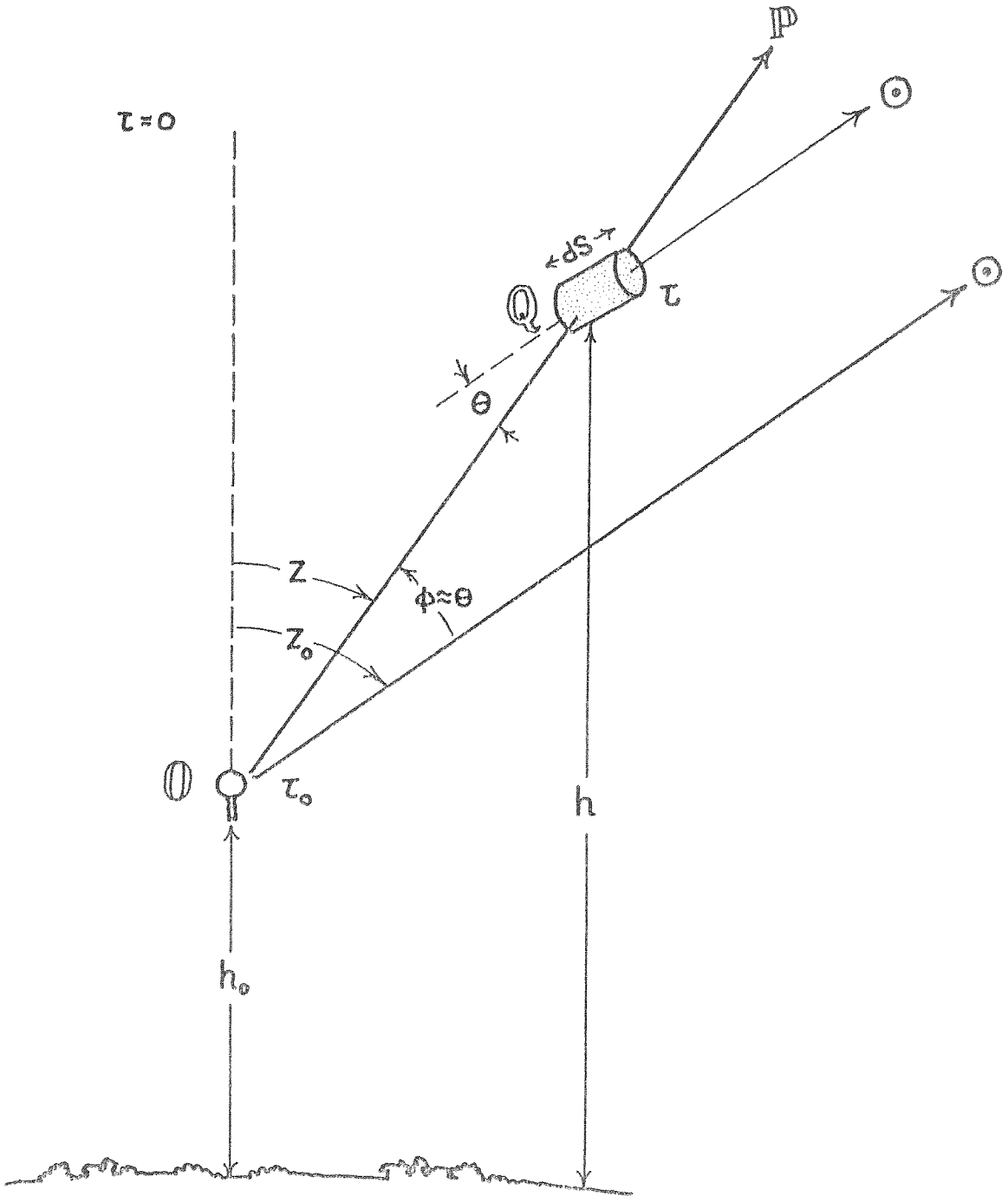

Figure 3

Atmospheric scattering by a volume element dS.

Using Equation (10) we can express the brightness scattered in the direction Θ by the volume element as

$$dB(\Theta, m, x) = \frac{\sigma_\Theta(m, x)\, I_o N e^{-\tau \sec Z_o}}{\omega_{inst}} \, dS \qquad (12)$$

where N is the number of particles per cm^3. The total brightness received by the photometer from the direction OP is obtained by integrating Equation (12) along OP from the point 0 to the top of the atmosphere. This is equivalent to an integration along the zenith direction from point 0 to the top of the atmosphere for a constant scattering angle Θ. The integration must also include atmospheric attenuation that occurs between the scattering particle and the observer. This attenuation can be expressed in terms of the differential optical depth $(\tau_o - \tau)$ between points 0 and Q as

$$e^{-(\tau_o - \tau)\sec Z}$$

so that the total scattered brightness received at 0 is

$$B(\Theta,m,x,h_o) = \int_{h_o}^{\infty} e^{-(\tau_o - \tau)\sec Z} \, dB \qquad (13)$$

By means of Equation (12) and the relation $dS = dh \sec Z_o$ we obtain

$$B(\Theta, m, x, h_o) = \frac{I_o \sec Z_o}{\omega_{inst}} \sigma_\Theta (m, x) e^{\tau \sec Z - \tau \sec Z_o - \tau_o \sec Z} \int_{h_o}^{\infty} N dh \qquad (14)$$

In taking the exponential term outside the integral in Equation (14) we have ignored the altitude dependence of the Mie scattering optical depth. This is justified by the small value of τ.

For the case of observations made at zenith angles near that of the sun, $Z = Z_o$ and Equation (14) takes the simpler form

$$B(\Theta,m,x,h_o) = \frac{I_o \sec Z_o}{\omega_{inst}} \sigma_\Theta (m,x) e^{-\tau_o \sec Z_o} \int_{h_o}^{\infty} N dh \qquad (15)$$

We note that for the case $Z = Z_o$ there is no dependence on the height of the individual scattering particles. A particle at the top of the path contributes the same scattered intensity as one that is near the observer.

The integral in Equation (15) covers a linear path that extends from the height of the observer to the top of the atmosphere. We can simplify the formulation by defining a particle density N'(a) as

N'(a) = the number of particles (of radius a cm.) enclosed in the column of cross section 1 cm^2 that extends from the observer to the top of the atmosphere.

I shall henceforth refer to N'(a) as column density, or particles per cm^2 column. With this definition we can rewrite Equation (15) as

$$B(\Theta,m,x,h_o) = \frac{I_o}{\omega_{inst}} \sec Z_o \, \sigma_\Theta(m,x) e^{-\tau_o \sec Z_o} N'(a) \qquad (16)$$

The brightness of the sun, recorded by the same photometer under the same conditions is

$$B_\odot (h_o) = \frac{I_o \, e^{-\tau_o \sec Z_o}}{\omega \ \omega_{inst}} \qquad (17)$$

Consequently the brightness ratio is given as

$$\frac{B}{B_\odot} = \omega_\odot \sec Z_o \, \sigma_\Theta (m,x) \, N'(a) \qquad (18)$$

This brightness ratio is defined for a certain wavelength λ that is fixed by the size parameter $x = 2\pi a/\lambda$ in the scattering cross section.

Equation (18) expresses the sky brightness that results from Mie scattering by a number $N'(a)$ of particles all of radius a. A more realistic case is that in which the column is populated by a variety of particles with a certain size distribution. In this case the total column population is given by

$$N' = \int_{a_{min}}^{a_{max}} N'(a)\, da \tag{19}$$

where the minimum and maximum particle radii are given by a_{min} and a_{max} respectively. The expression for sky brightness due to Mie scattering in this case is

$$\frac{B}{B_\odot} = \omega_\odot \sec Z_o \int_{a_{min}}^{a_{max}} \sigma_\Theta\,(m,x)N'(a)da$$

or

$$\mu_o \frac{B}{B_\odot} = \omega_\odot \int_{a_{min}}^{a_{max}} \sigma_\Theta(m,x)N'(a)da \tag{20}$$

Here we have assumed that the particles are all of the same refractive index. If particles of more than one index of refraction populate the column a sum of equations such as (20) must be used.

Equation (20) will be used in Chapter V to interpret the non-Rayleigh sky brightness.

CHAPTER III

APPARATUS

A. Introduction

In Chapter IV I report spectral sky observations made during one of the stratospheric balloon flights of Project Coronascope. The basic instrument in the Coronascope experiment was an externally-occulting coronagraph called the flying coronagraph. This instrument and auxiliary equipment were carried by balloon to a maximum altitude of about 80 kft. in an unmanned gondola. At a preset time during ascent the flying coronagraph was released from a stowed position in the gondola frame and pointed at the solar disk. The instrument continued to point at the sun for about six hours; during this time the balloon ascended to maximum altitude, floated there for about two hours, and then descended through the lower stratosphere. The rate of descent was controlled by remote ballasting and valving. Sky brightness data were recorded both photographically and photoelectrically throughout the period of automatic pointing. At a selected point in the flight trajectory the gondola was separated from the balloon and allowed to descend to the ground by parachute. During the parachute descent the coronagraph was returned to the stowed position within the gondola in order to reduce landing damage. Successful flights were conducted on 10 September 1960 and 3 October 1960. Figure 4 is a photograph of the Coronascope gondola on the launch truck. Figure 5 is a photograph of the 3 October launch scene. A report of the flight details is contained in the final report of the balloon contractor (General Mills, Inc., 1960).

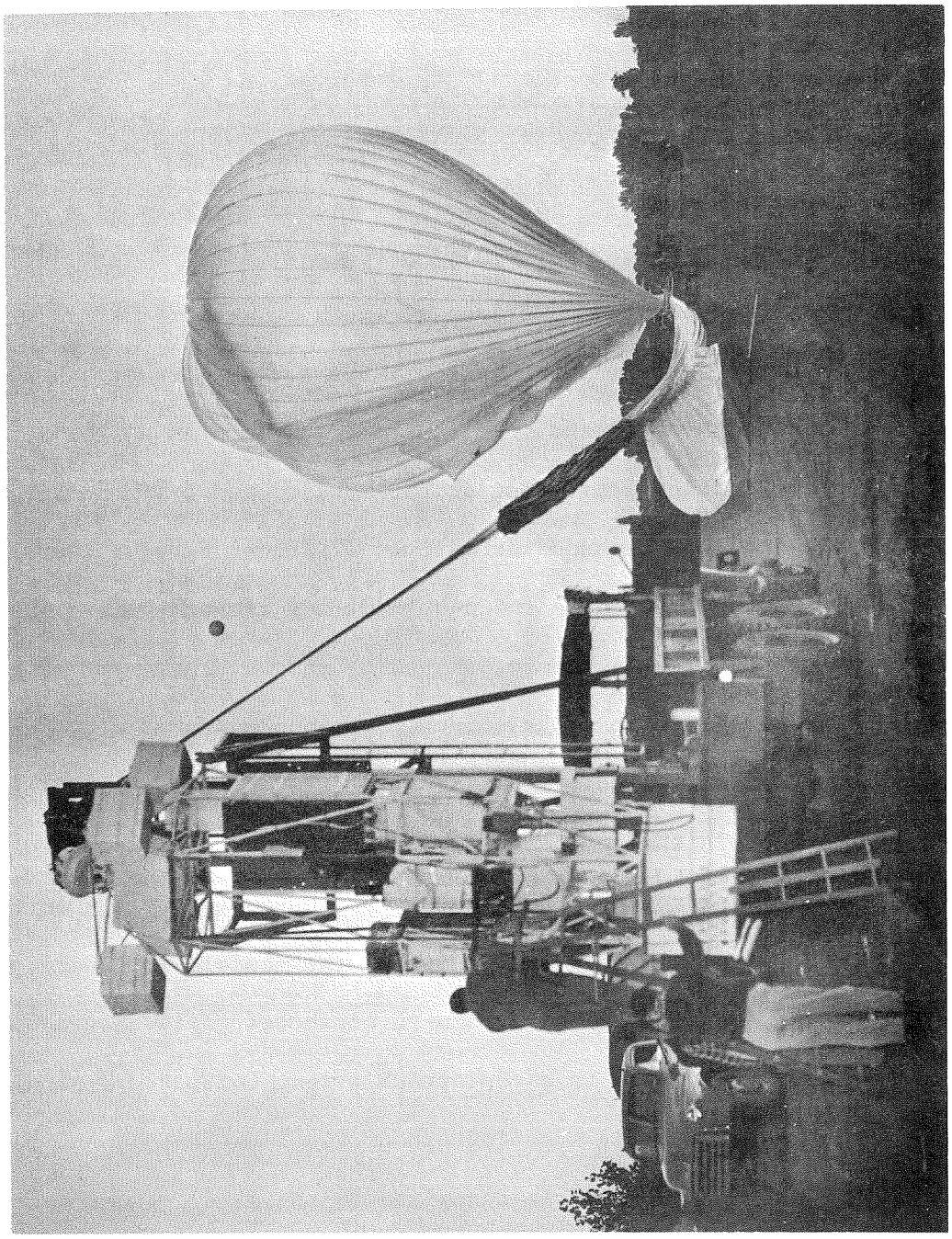

Figure 4

Coronascope gondola on the launch truck

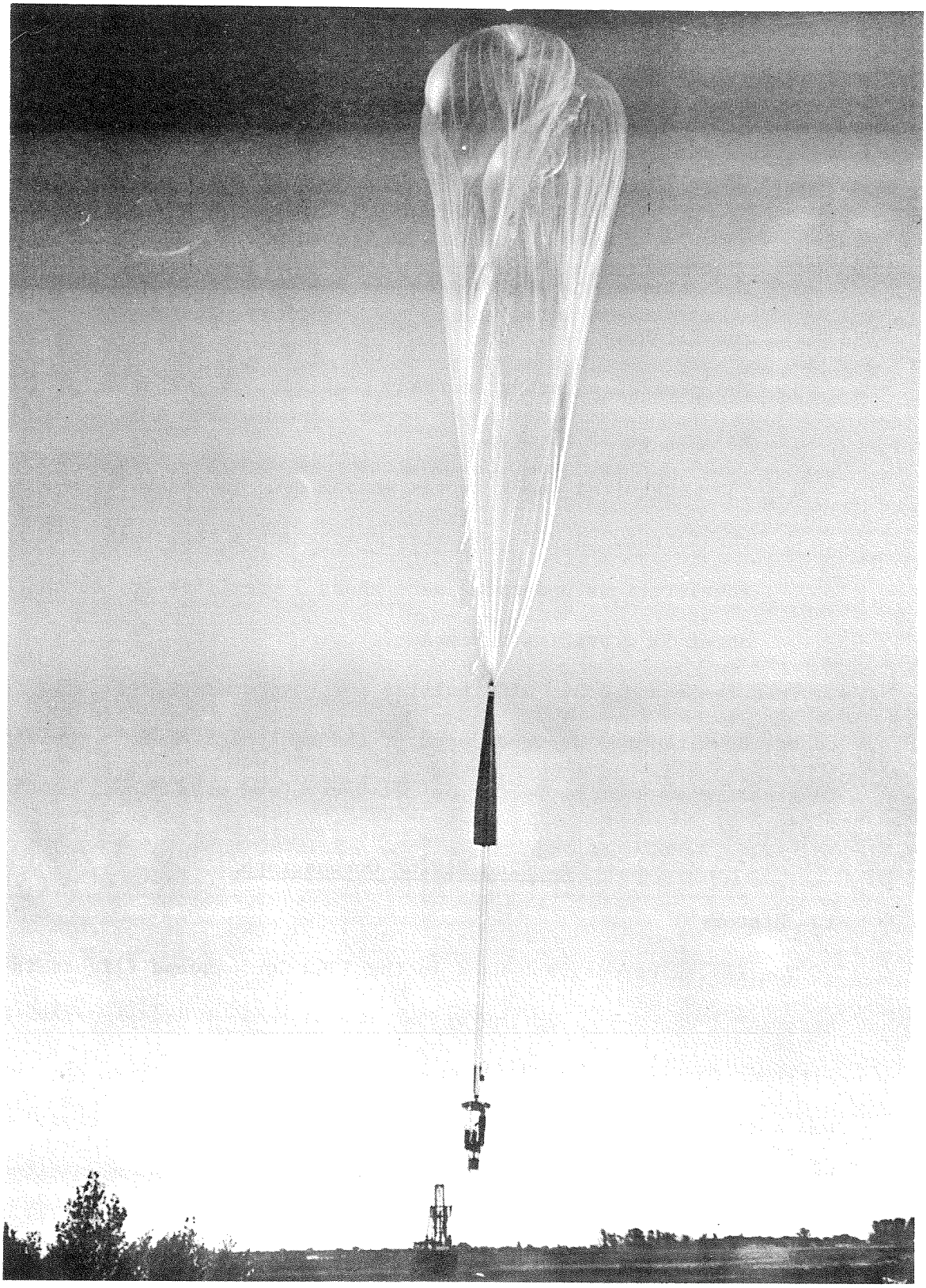

Figure 5

Launch, 3 October 1960

The design and construction of apparatus used to carry out the Coronascope mission were made difficult by many factors. Some of them were:

1. The low values of sky intensity to be recorded, especially in the long wavelength region at peak altitude, where sky brightness is as low as 10^{-8} $B_{\odot}$.
2. The extreme changes in pressure and temperature encountered during the flight.
3. The precise pointing accuracy required, for exposure periods as long as 25 minutes.
4. The mechanical shock forces encountered in the various phases of the flight. Acceleromometer measurements indicated that the accelerations undergone were about 3 gravities on launch, and about 5½ gravities on impact.

That these and other difficulties were overcome successfully is a tribute to Dr. Newkirk, who designed most of the equipment, and to the capable and imaginative work of R. H. Lee, L. B. Lacey, and many others on the HAO staff.

B. The Flying Coronagraph

1. History

The flying coronagraph used in the 1960 Coronascope flights is an instrumental descendant of the visual sky photometer designed for the High Altitude Observatory in 1946 by Evans (1948b). The visual sky photometer was a small, portable, Lyot coronagraph with an external occulting disk. It was used to measure sky brightness on the ground and at altitudes to 30 kft. from an aircraft (Evans, 1948a). The first major modification of the visual sky photometer was called the photographic sky photometer; it also was designed by Dr. Evans. This modification permitted photographic photometry of sky brightness in several wavelength regions. The photographic

sky photometer has been described by Newkirk (1956) who used it for a program of aureole observations made in the Rocky Mountains. The photographic sky photometer was later modified by Dr. Newkirk for use in a manned balloon gondola; it was used by Mr. R. H. Cooper in a manned flight to an altitude of 38 kft. in 1959. (Cooper, Eddy, Newkirk, 1960). The flying coronagraph flown in the 1960 Coronascope flights was a further modification of the photographic sky photometer. Since there is no current description of the flying coronagraph in the literature, I shall describe it briefly here, with the note that it was not designed by me.

2. Description

The flying coronagraph is a spar, about seven feet in length, on which are mounted a photoelectric sky photometer (P.E.P.) and a photographic sky photometer (P.S.P.). In operation it is oriented so that the axis of the spar points at the center of the sun.

The P.E.P. records sky brightness at a point 10°.3 from the sun, at an effective wavelength of 0.52μ. The P.E.P. also controls the exposure times of the P.S.P.

The P.S.P. employs a 35 mm. camera to record data from three sources: a wide-angle (periscope) photometer, a sky spectrograph, and an infrared coronagraph. The periscope records linearly-polarized sky brightness of wavelength 0.44μ at five fixed angles from the sun. The spectrograph and IR coronagraph are described below. I have not discussed the periscope portion of the P.S.P. since my thesis does not concern angular sky brightness data.

There are four optical paths through the photographic sky photometer: a) a main coronagraph beam, b) a photometric standardization beam, c) a guiding beam, and d) a beam for shutter control. A schematic diagram of

the instrument is given in Figure 6, to which reference is made in this section. The axis of each beam points to the center of the solar disk; in the figure sunlight comes from the left.

a) Main Coronagraph Beam

The external occulting disk D_1 shades the first aperture A_1 and keeps direct sunlight from passing into the instrument. Its diameter (19 mm.) subtends an angle of 42' of arc at the focal plane of the camera. The objective lens L_1 forms an image of D_1 on an internal occulting disk D_2. The internal occulting disk is slightly larger than the projected image of the external disk and therefore intercepts most of the diffracted light around the D_1 image. The slit of the sky spectrograph lies in the same plane with D_2. The slit is 0.5 mm. in width and 5.5 mm. long; it receives skylight from a radial region of the sky extending from 1° to 3½° from the center of the sun. A field lens L_2 forms an image of the aperture A_1 on the Lyot aperture stop A_2 to eliminate light at the edge of A_1. The same lens also forms an image of the sky on the focal plane of the camera. The mirror M_1 is an image-divider that deflects the image of the slit toward mirror M_2 and passes the other side of the sky image to the focal plane. The sky image that passes M_1 is intercepted by an infrared filter that lies directly in front of the film plane.

The filtered beam registers on the film an image of the sky seen in the near infrared, extending from 1 to 11 solar radii (about 6°). A Wratten Filter No. 89B was used on the 3 October 1960 flight, with effective wavelength 0.79μ. Figure 7 shows the wavelength-sensitivity curves for the filter-film combination.

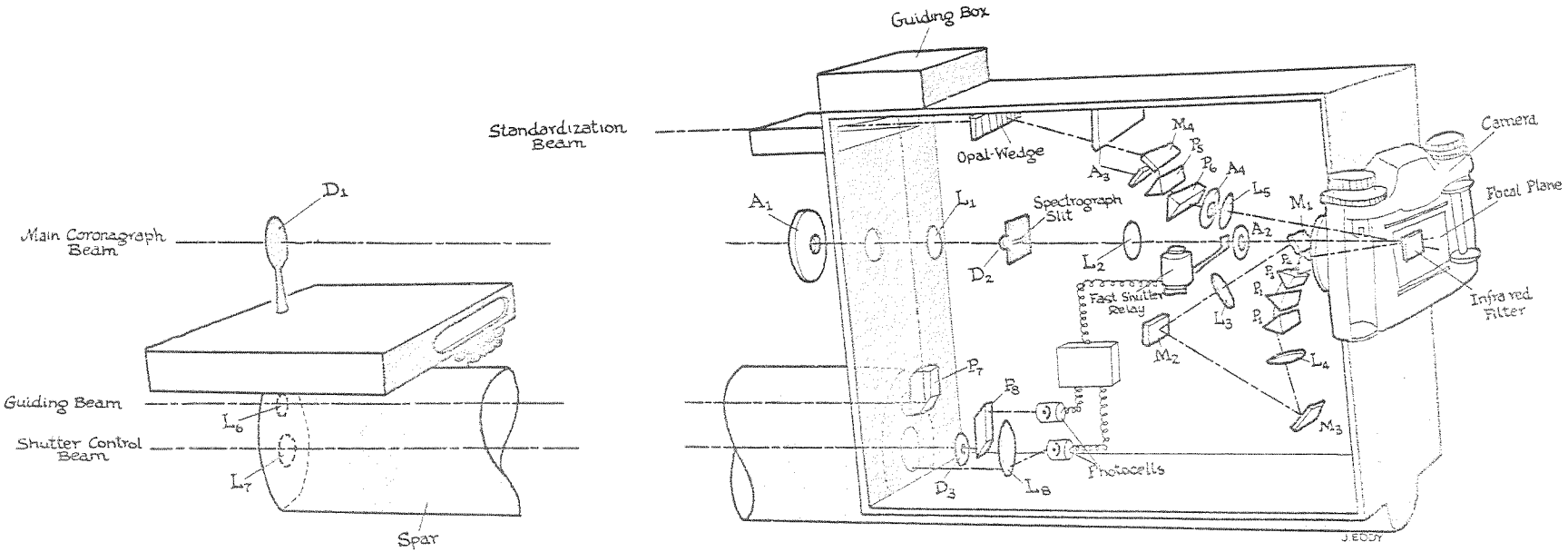

Figure 6

Schematic diagram of flying coronagraph

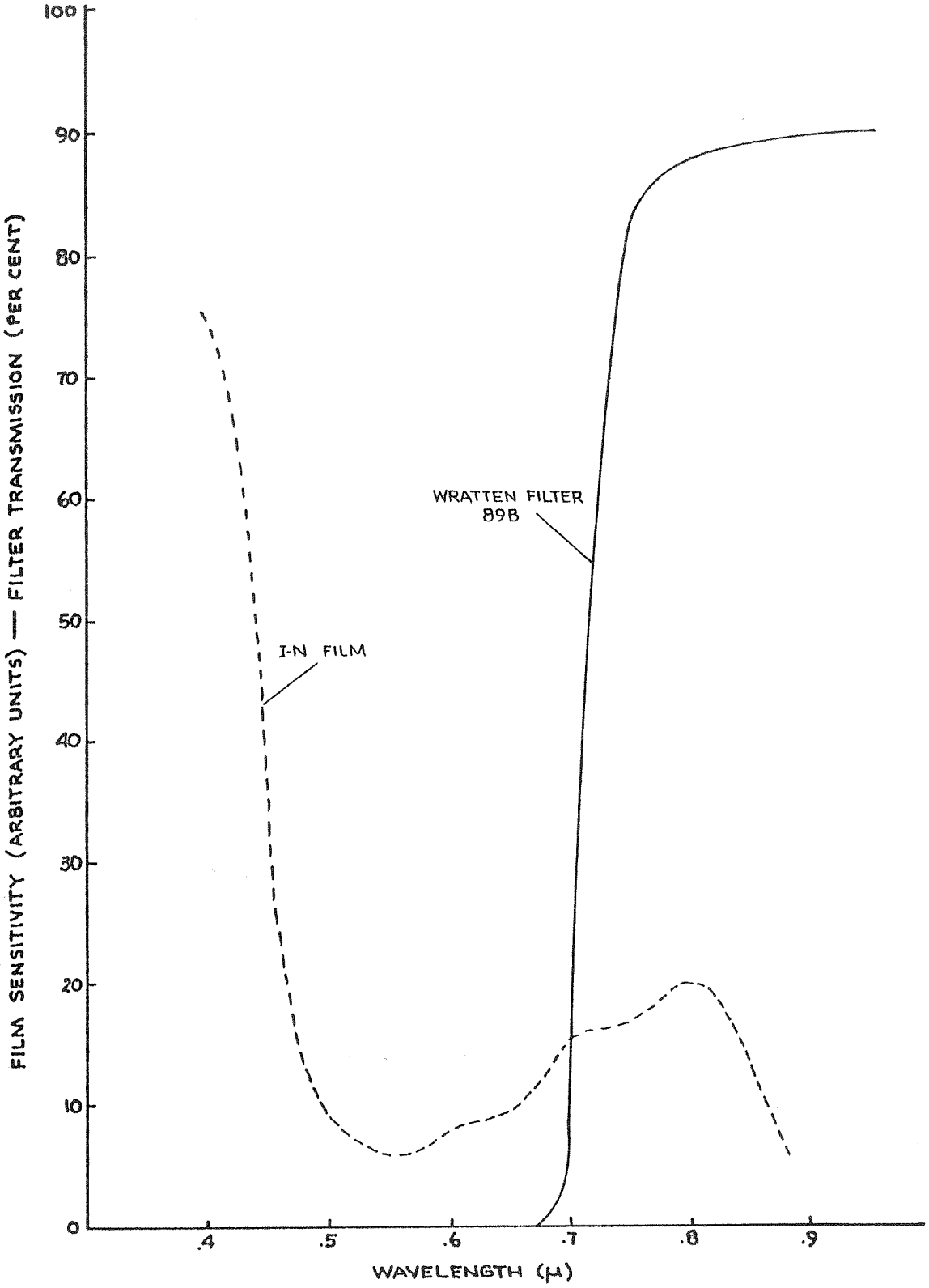

Figure 7

Spectral sensitivity of I-N emulsion and transmission of infrared field filter

The portion of the sky image that is intercepted by M_1 is passed by a series of lenses and mirrors to the main spectrograph, which consists of the four prisms P_1, P_2, P_3, and P_4. The prisms disperse the image of the slit and direct the dispersed image onto the film plane where a spectrum of the sky is recorded. A dispersion curve for the main spectrograph is shown in Figure 8. We note that the dispersion was about 320 Å/mm at 0.40μ and about 2100 A/mm at 0.80μ. The instrument profiles (apparatus functions) that result from the dispersion data are shown in Figure 9. They include the effect of the finite slit width of the microdensitometer used in the data reduction. Correction factors R_λ were derived to compensate for the instrument profile widths; these are given in Table 3.

Table 3. Correction factors for instrument profiles

Wavelength λ	Correction factor R_λ
0.37μ	1.003
0.395	0.998
0.432	0.980
0.47	0.949
0.55	0.965
0.64	1.049
0.72	1.057
0.78	0.891
0.79	1.011

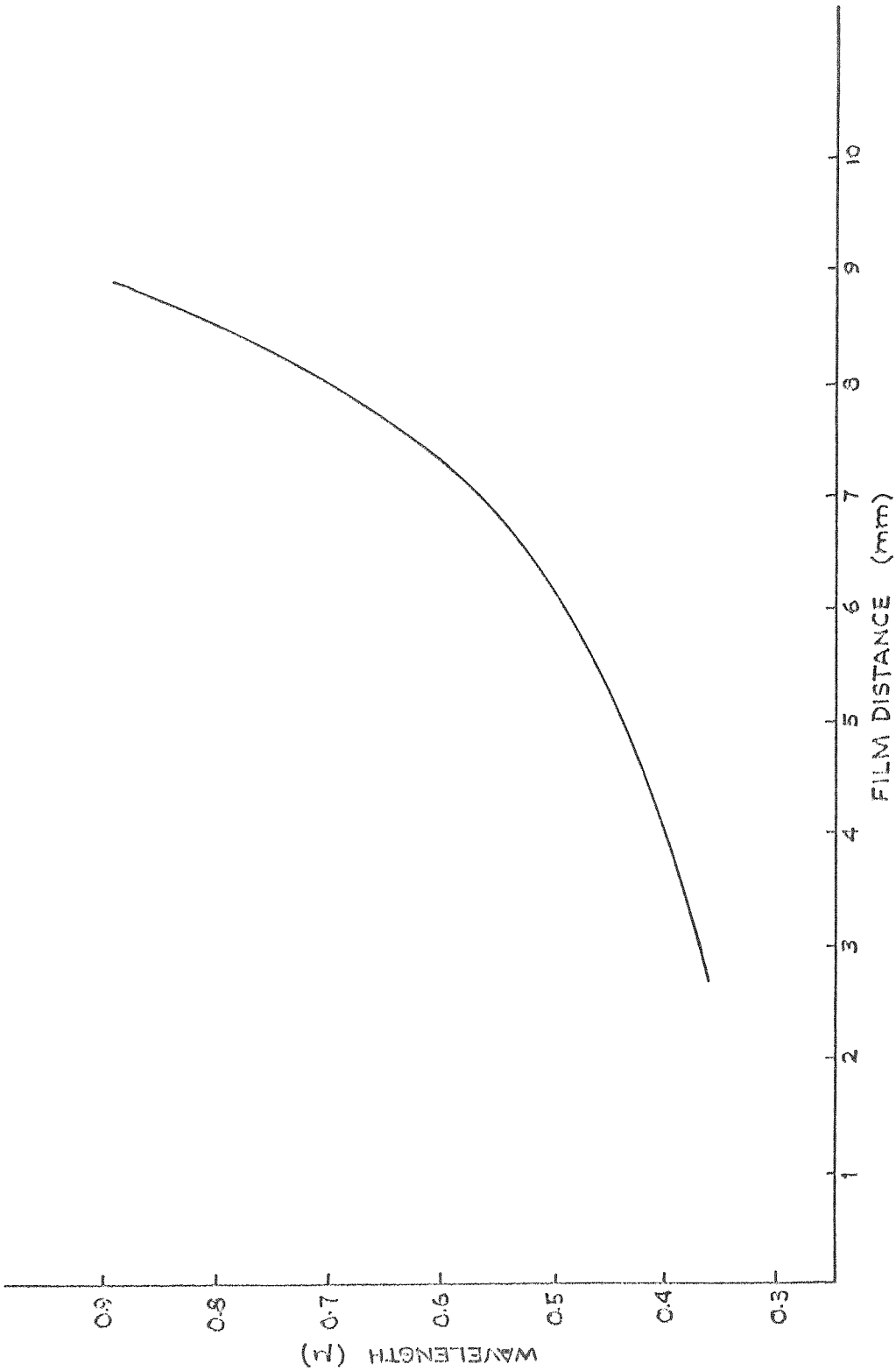

Figure 8

Dispersion curve of flying-coronagraph-spectrograph

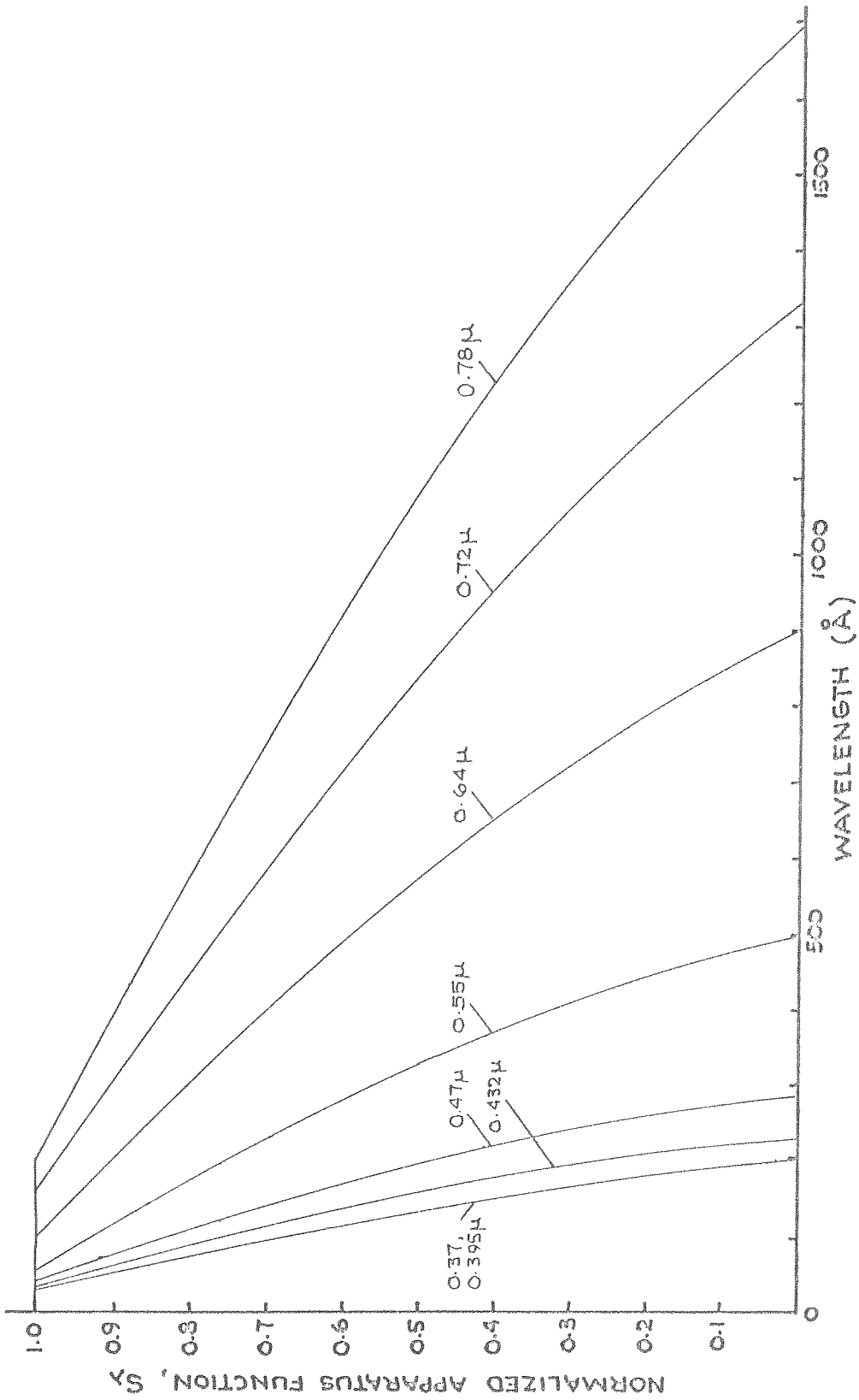

Figure 9

Instrument profiles (apparatus functions) for flying-coronagraph-spectrograph and microdensitometer

The correction factors were calculated by use of the following formula:

$$\frac{B}{B_\odot}\lambda' = R_{\lambda'}\left[\frac{B}{B_\odot}\lambda' \text{ obsvd}\right]$$

where

$$R_{\lambda'} = \frac{I_{\lambda'}\, O_{\lambda'}\left[\int_{\lambda_1}^{\lambda_2} SF d\lambda\right]^2}{\int_{\lambda_1}^{\lambda_2} ISF d\lambda \int_{\lambda_1}^{\lambda_2} OSF d\lambda} \qquad (21)$$

where

$S(\lambda)$ = combined instrument profile of spectrograph and microdensitometer at wavelength λ.

$F(\lambda)$ = film sensitivity

$O(\lambda)$ = brightness of opal-wedge photometric standard

$I(\lambda)$ = brightness of Rayleigh sky

The limits of integration λ_1 and λ_2 are fixed by the width of the instrument function at the wavelength λ'.

The wavelength point 0.79μ was taken from the infrared coronagraph field. The correction factor R_λ for this point was obtained by the formula above but with $S(\lambda)$ taken as the filter transmission. The main coronagraph has an f-ratio of 1/100.

b) Photometric Standardization Beam

The opal wedge combination is illuminated by the direct solar beam; it is a calibrated wedge that was made by placing a neutral photographic step wedge over a small plate of opal glass. The diffuse, attenuated sunlight transmitted by the wedge is passed through an aperture A_3 to a mirror M_4 from which it is directed into the prisms P_5 and P_6. These prisms form an objective spectrograph that disperses the diffuse wedge

image in a direction parallel to the step divisions of the wedge. The dispersed image is focused on the film plane by the lens L_5, impressing on each frame of the film a photometric standard, each step of which is dispersed in wavelength.

The calibration of the step wedge is discussed in Section C.

c) Guiding Beam

The optical path of the guiding beam is through the hollow spar of the flying coronagraph. An objective lens L_6 at the end of the spar projects the solar beam through the prism P_7 and forms an image of the sun in the guiding control box. The guiding box houses the final set of photocells that provide precise automatic guiding on the solar image. During the Coronascope flights, a pointing accuracy of $\pm$ 2' was realized.

d) Shutter Control Beam

The shutter control beam also passes through the hollow spar. An objective lens L_7 at the end of the spar forms an image of the sun on an occulting disk D_3 that is pierced in the center. Direct sunlight is allowed to pass through the center hole of D_3, through a prism P_8, and into the upper of two photocells. Light that passes around the edge of D_3 is imaged by a condensing lens L_8 into the lower photocell. A balancing circuit is connected to the output of the two cells to close the shutter in the main coronagraph beam whenever the light from around D_3 exceeds a certain fraction of the light from its center. This system interrupts the photographic exposure whenever the flying coronagraph is misguided, thereby preventing direct sunlight from reaching the film in the main coronagraph beam. The shutter so controlled is called the "fast shutter" and is not the shutter that controls the length of the photographic exposures made with the system.

e) Camera and Film

The camera used in the P.S.P. is a 35 mm. Praktina Model FX, equipped with a focal plane shutter that is opened and closed by pulses from an electronic exposure control circuit. The exposure lengths used are governed by a signal from the P.E.P., which acts in this capacity as a photographic light meter. A preset sequence of short and long exposures interrupts and supersedes the P.E.P. exposure signal at fixed intervals. This feature is included to provide a range of exposure lengths should the P.E.P. signal fail. The exposure lengths provided in the two systems of control range from 5 seconds to 25 minutes. The maximum exposure length was used at peak altitude.

The P.S.P. camera was loaded before each flight with 50 feet of Kodak I-N Spectroscopic film that provided usable photographic sensitivity from .35μ to 0.85μ. The short wavelength limit was fixed by the ultraviolet glass cutoff of the optical system. The film was developed for 10 minutes in Kodak Microdol-X, diluted one-half. The spectral sensitivity curve of the I-N emulsion was shown in Figure 7; it was taken from the Kodak catalog.

Figure 10 shows a typical frame taken with the P.S.P. camera during the 3 October 1960 flight. The sky spectrum is in the upper left corner; dispersion is vertical with violet at the bottom. The horizontal extent of the spectrum represents the slit width of the main spectrograph; it extends from about 3 $R_\odot$ on the left to about 11 $R_\odot$ on the right. Below the spectrum is the dispersed image of the opal wedge standard; dispersion is vertical with violet at the top. Six of the ten wedge steps are visible on this print. In the upper right quadrant of the frame is the infrared field; at the lower left corner of the infrared field is the image of the

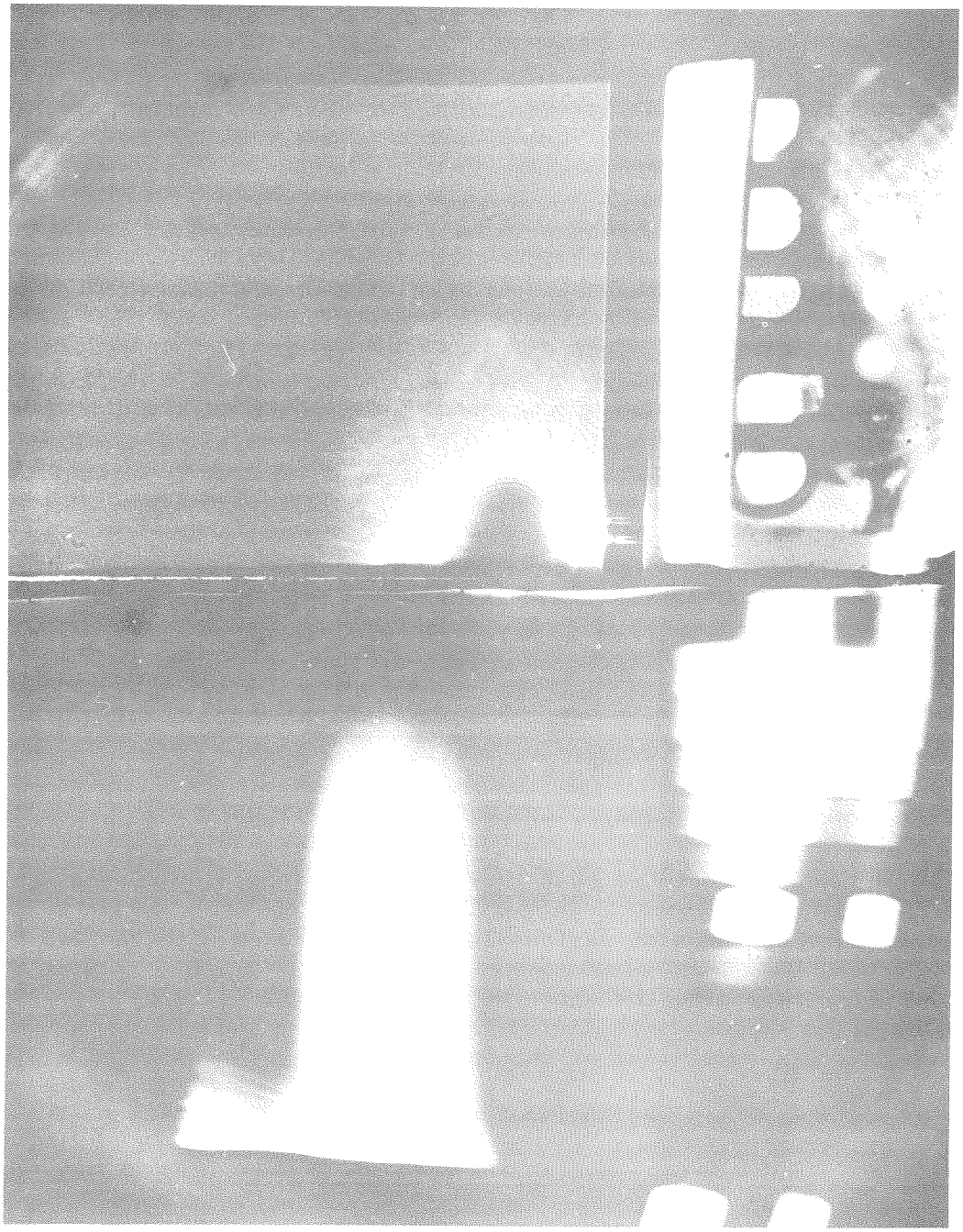

Figure 10

Flying coronagraph frame

internal occulting disk. Light around the disk is diffracted light. In the lower right are the five periscope windows of the wide angle photometer and a set of binary lamps that provide frame identification.

C. Calibration

The dispersed image of the opal wedge provides a photometric standard of brightness on each frame that was taken with the flying coronagraph. Absolute values of brightness (in units of the mean solar brightness, $B_{\odot}$) were determined for eight selected wavelength regions of each step of the dispersed wedge image. This was done by a calibration procedure that was carried out on the ground before each flight. The method of calibration was the following:

a. The flying coronagraph was automatically pointed at the sun.

b. Direct sunlight was allowed to enter the photometric standardization beam.

c. A series of opal glass filters of known spectral radiance were placed next to the occulting disk in the main coronagraph beam so that they were illuminated by direct sunlight.

d. Exposures of various lengths were taken with the P.S.P., recording the spectrum of each of the illuminated opal glass filters on the same frame with the opal-wedge spectrum.

e. The film was analyzed by comparing the density of the opal-wedge spectrum with the density of each opal filter spectrum. The density of the infrared field and the density of the wedge spectrum at a corresponding point in the infrared were also compared.

f. Each wavelength position of each step of the wedge was assigned a value of brightness based on a comparison with corresponding wavelength positions of the opal filters.

The opal-glass filters that were used as the standard of brightness in the calibration of the wedge were eleven 2 x 2" diffusing glass filters. The brightest of these is ground glass; the other ten are opal glass. One of the opal-glass filters is unattenuated; the other nine are cemented to neutral film filters of different densities. The result is a set of diffusing filters, whose radiance relative to the mean radiance of the solar disk can be evaluated. The brightest has a radiance of about $10^{-4}B_{\odot}$ in the violet. The opal-glass standards were calibrated by Dr. Newkirk in the laboratory at Boulder using a photoelectric photometer whose wavelength response was limited by a series of interference filters.

The dispersion curve of the main spectrograph was obtained prior to each flight by placing gas discharge tubes in the spectrograph beam immediately in front of the objective aperture (A_1) and recording the spectrum obtained. Major lines of mercury vapor, neon, and argon were used for this calibration.

The dispersion curve of the calibration spectrograph (standardization beam) was determined by placing a series of narrow band filters in front of the aperture leading to the opal wedge. The spectrum of the sun that was recorded indicated the wavelength positions of the transmitted peaks.

CHAPTER IV

OBSERVATIONS

A. Explanation

Observations of spectral distribution of skylight in the aureole were made on 10 September 1960 and 3 October 1960; 83 photographic frames were analyzed from these two flights. Much of the 10 September spectral data were off the scale of the comparison wedge, so that reliable analysis of this data was not possible. The wedge was modified before the 3 October flight so that complete spectral data were obtained on the second date. A comparison of the usable data of 10 September with corresponding 3 October data showed general agreement in intensity and spectral distribution. Only the 3 October data are shown here.

The data given here represent the first observations of the stratospheric aureole. Since they are unique data that may be of interest to other workers I have shown the observed brightness values in tabular form as Table 4 in Section B. They are compared with other observations in Section D, and interpreted in Chapter V. Column entries are explained below.

Column 1: Photographic frame number.

Column 2: Central Standard Time, at which each observation was made.

Column 3: Altitude of the gondola in kilofeet, obtained from a Wallace and Tiernan Model FA-129 altimeter that was carried on the gondola.

Column 4: Cosine of the solar zenith distance ($\mu_o = \cos Z_o$) for the median time of the observation. Values given were calculated by means of the formula

$$\mu_o = \sin\Phi \sin\Delta + \cos\Phi \cos\Delta \cos H \qquad (22)$$

where Z_o = zenith distance of the center of the solar disk

Φ = latitude of the point of observation

Δ = declination of the sun

H = hour angle of the sun

Equation (22) was evaluated for each point of the balloon track at which an observation was made.

Columns 5-13: observed sky brightness for the effective wavelength indicated, expressed in units of millionths of the brightness of the sun ($10^{-6}B_{\odot}$) at the same wavelength. Thus an entry of 0.34 indicates a brightness of $0.34 \times 10^{-6}B_{\odot}$. The solar brightness referred to is that of the mean solar disk as it appears at the altitude at which the observation was made. It is a reference that changes with height. The data in columns 5 through 12 were obtained from the sky spectrograph; data in column 13 were obtained from the infrared coronagraph. All the brightness values are for the azimuth angle $\phi = 144'$ from the center of the sun, measured in the instrument plane. Brightness data given here are raw data, corrected for the instrument profile using the corrections given in Table 3. Values enclosed in parentheses were obtained from non-linear portions of the characteristic film curve and are of lower weight. Data from columns 5-13 are shown as a function of altitude in Figures 18 to 26 in Chapter V.

Other explanations regarding the data in Table 4 are given below:

1. Vertical Motion - The balloon was moving vertically to some extent during all the exposures; the brightness given for a particular observation represents an integration in time and altitude. The values of time, altitude, and zenith distance for a given frame are therefore mean values. The longest exposures (20 or more minutes in length) were taken at peak altitude when the balloon was floating at nearly constant

height. As the balloon descended to a brighter sky the exposures were shorter. The most serious integration effects occur on the lower portion of the flight, when descent rates as high as 600 feet per minute were encountered. A diagram of the altitude profile for the 3 October flight is shown in Figure 11. Numbers shown on the curve are photographic frame numbers. Even-numbered frames are drawn with a heavy line.

2. Horizontal Motion - A chart of the ground track for the 3 October flight is shown in Figure 12. The ground speed of the balloon was about 30 miles per hour, so that during a single exposure it moved as much as 10 miles over the ground. In computing the zenith distance I used the geographical position of the balloon at the midpoint of each exposure; the error due to averaging over a given exposure is negligible. Another result of horizontal motion was the continuous change of ground conditions beneath the balloon, resulting in a possible change in ground albedo. The terrain beneath the balloon track was reasonably homogeneous in the sense that there was no systematic change in landscape along the flight. The ground could be described as a mixture of dry midwest farmland and deciduous forest in early autumn.

3. Weather Conditions - Figure 13 shows the vertical temperature structure of the atmosphere at St. Cloud, Minnesota, obtained by a temperature sounding at 0502 CST on 3 October 1960. The altitude region in which aureole measurements were made is shown as a shaded rectangle. We note that all the sky brightness data were obtained above the tropopause (40 kft.) in a region in which the temperature variation was less than 10°C.

Figure 14 shows a synoptic map of the surface weather at 1200 CST on the day of the flight; it represents the surface conditions in the

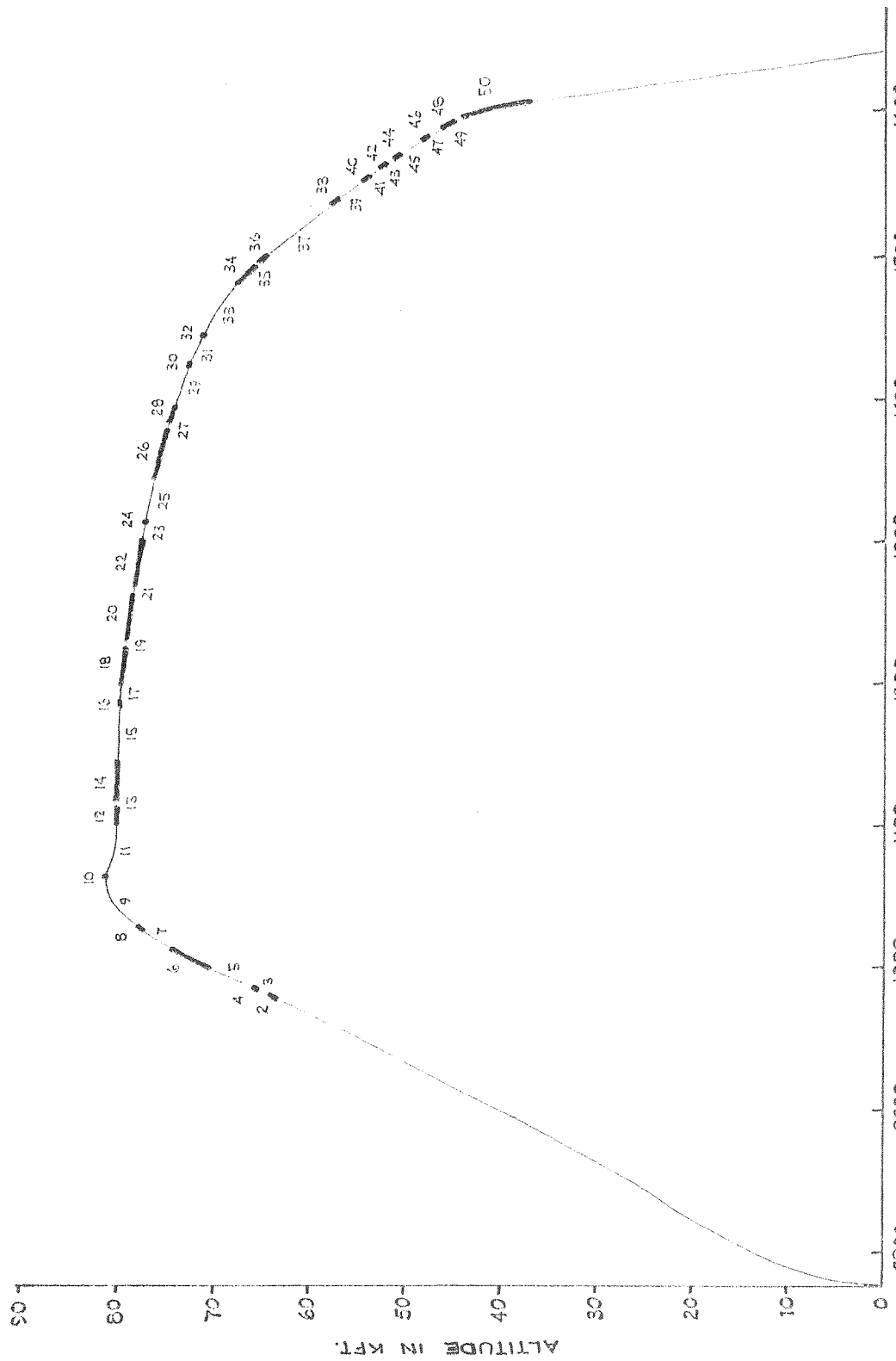

Figure 11

Altitude profile of 3 October 1960 Coronascope flight

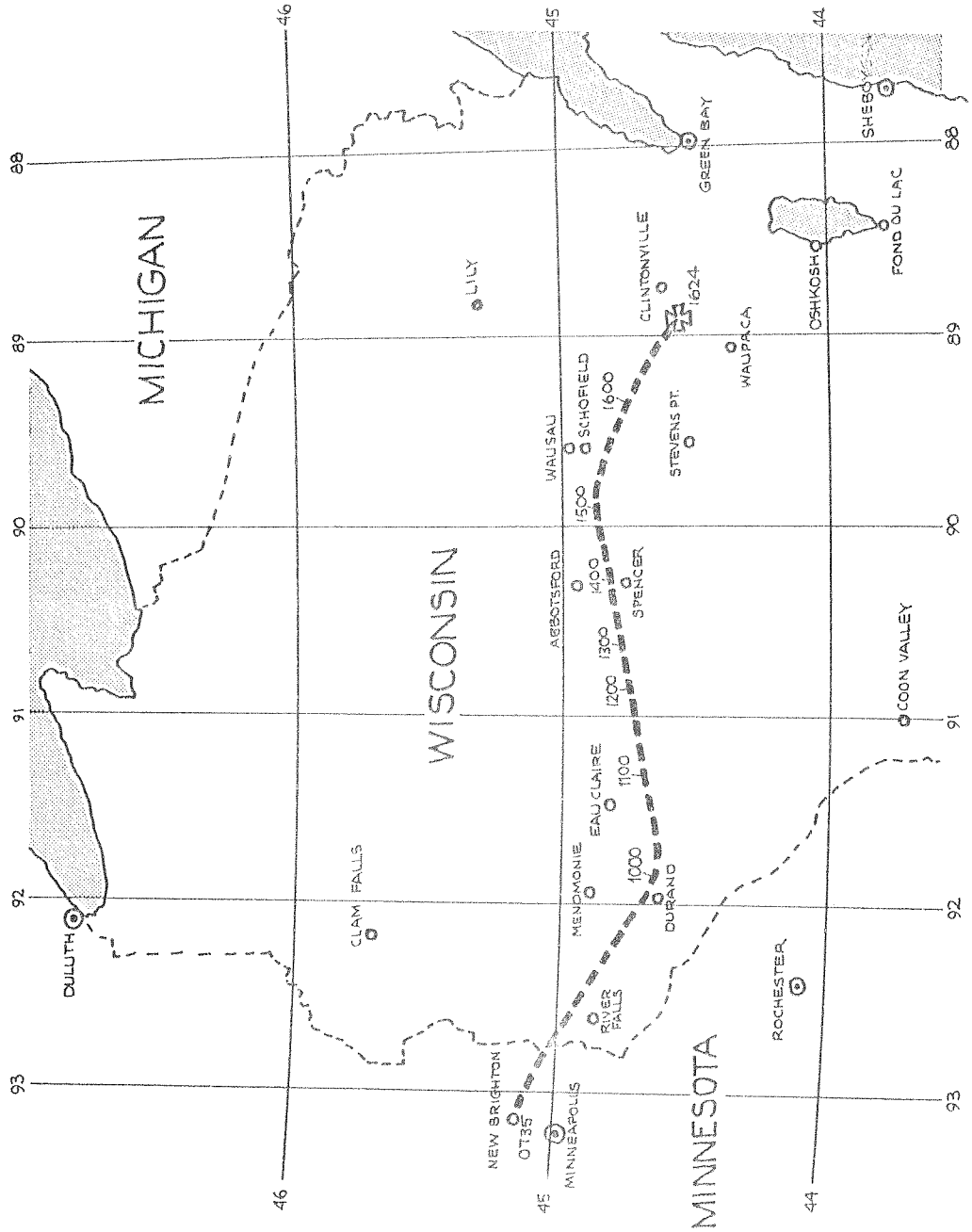

Figure 12

Ground track of 3 October 1960 flight

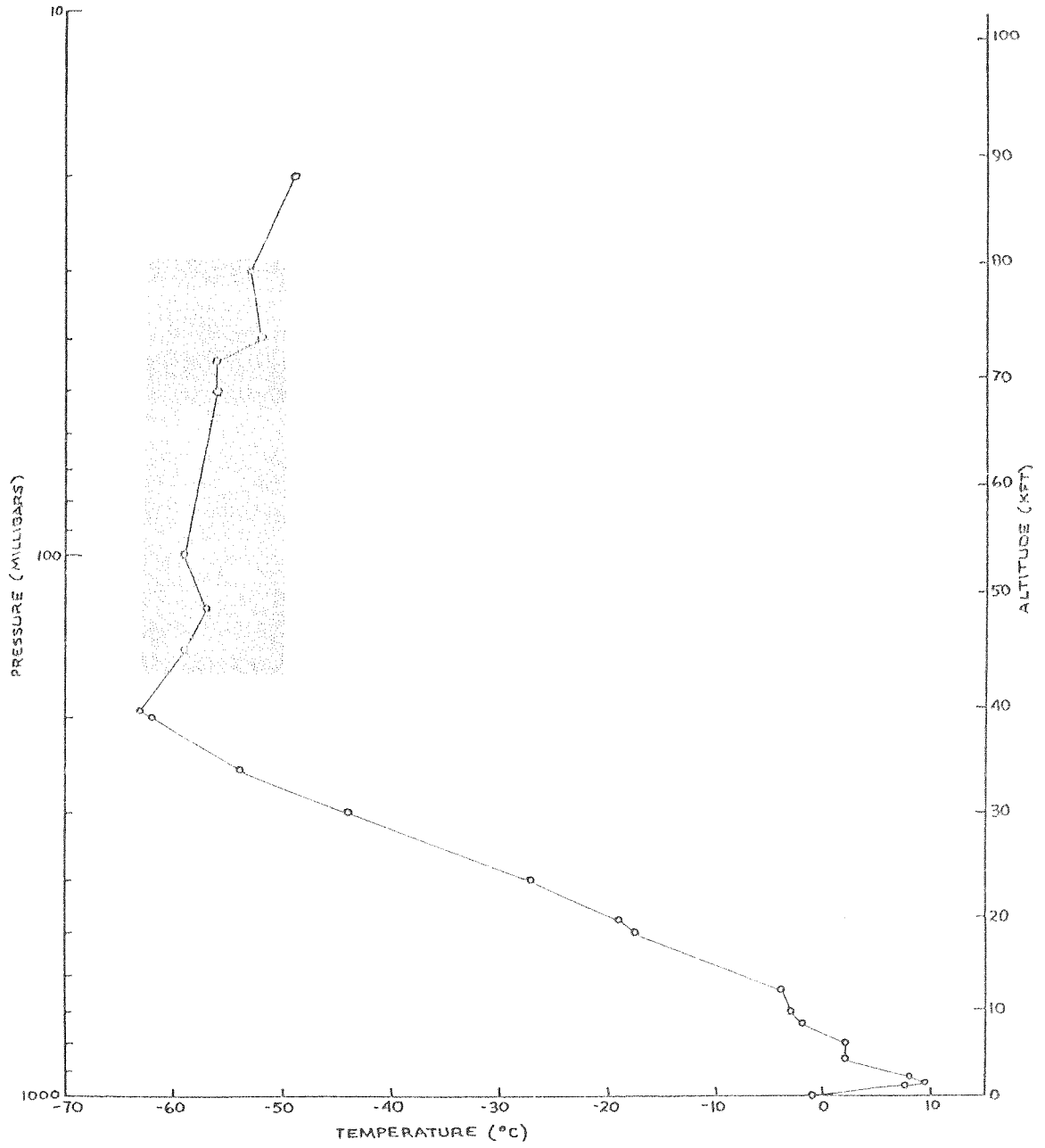

Figure 13

Vertical temperature structure, St. Cloud, Minnesota, 0502 CST,
3 October 1960

Figure 14

Surface pressure map, 1200 CST, 3 October 1960

middle of the 8-hour flight. The track of the balloon, indicated by a large shaded arrow, lies in the center of a high pressure region of polar origin.

A more detailed map of cloud coverage is shown in Figure 15. The cloud reports shown are for 0600 CST on 3 October 1960; they are given using the conventional meteorological symbols for cloud type and coverage. The track of the balloon is shown as a heavy dashed line. In the course of the flight the sky north of the track was essentially clear; south of the track a double cloud layer of cumulus and cirrus was formed. Total cloud coverage beneath the balloon was never more than one-tenth.

4. General Remarks - The values of sky brightness given in Table 4 apply to a particular set of observing conditions. They indicate the sky brightness at one place on one day as it changed with altitude and solar zenith distance. Interpretation of these values in terms of altitude variation must include an accurate correction for the change in solar zenith distance that occurred during the flight. As a first approximation we could correct for the effect of zenith distance variation by multiplying each observed value by the zenith distance cosine given in column 4. This amounts to correcting the atmospheric path length to that at the zenith, in such a way that an observation made at the zenith is uncorrected, while one near the horizon is reduced. I have done this in Section D in order to compare the observed data with other observations. A rigorous correction for the effect of zenith distance must include a complete analysis of the scattering problem, including the dependence of albedo on zenith distance. My interpretation in Chapter V includes these effects.

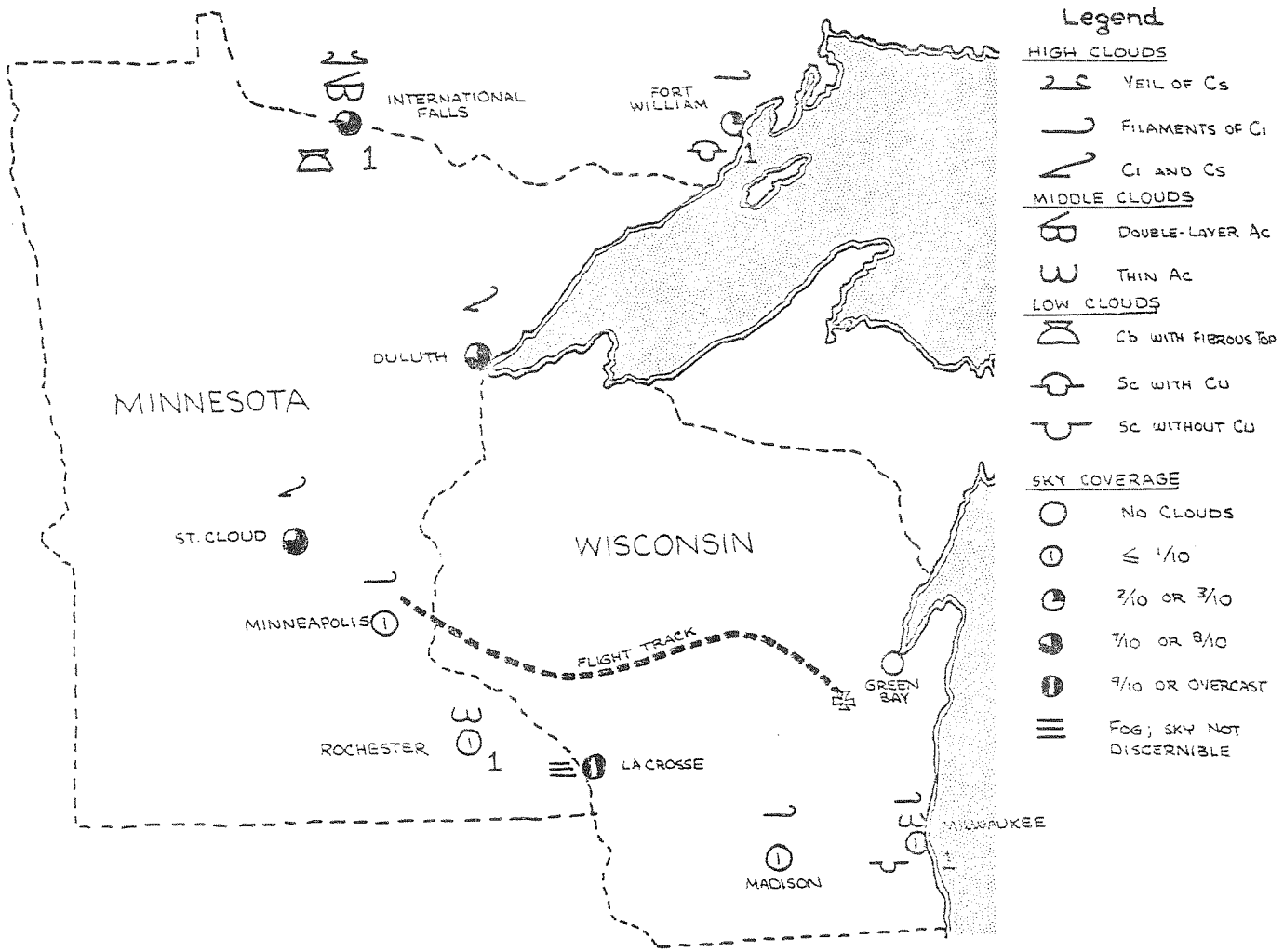

Figure 15

Cloud reports in vicinity of Coronascope flight, 0600 CST, 3 October 1960

B. Tabulation of Data

Table 4. Observed Sky Brightness, 3 October 1960

$(B/B_{\odot})_{\lambda} \times 10^{6}$

Frame	Time	Alt.	μ_o	.37μ	.395μ	.432μ	.47μ	.55μ	.64μ	.72μ	.78μ	.79μ
2	0946	63.0	.5493	1.09	0.97	0.77	0.53	--	--	--	--	0.13
3	0948	64.2	.5528	1.07	0.99	0.73	0.50	(.22)	(.120)	(.120)	--	0.054
5	0954	67.7	.5628	0.86	0.74	0.46	0.33	0.13	0.078	0.051	0.045	0.043
6	1003	72.2	.5771	0.68	0.59	--	0.26	0.076	(.029)	(.028)	--	0.032
7	1010	75.5	.5876	0.52	0.50	0.34	0.23	(.076)	(.055)	(.040)	(.035)	0.031
8	1014	77.1	.5931	(0.45)	0.48	0.30	(.14)	--	--	--	--	--
9	1024	80.0	.6060	0.41	0.38	0.30	0.18	0.074	0.034	0.027	(.024)	--
11	1048	80.2	.6314	0.36	0.35	0.24	0.14	0.059	0.025	0.021	0.015	0.018
12	1103	80.4	.6434	0.36	0.34	0.21	0.14	--	--	--	--	0.019
14	1117	80.1	.6518	0.36	0.34	0.20	0.10	0.051	0.018	0.017	(.015)	0.019
15	1137	80.0	.6592	0.41	0.34	0.23	0.13	0.057	0.029	(.017)	(.015)	0.020
17	1154	79.9	.6605	(.43)	--	0.237	--	--	--	--	--	(0.11)
18	1206	79.3	.6592	0.38	0.36	0.29	0.19	0.073	(.034)	0.027	(.021)	0.023
20	1226	78.9	.6526	0.39	0.38	0.27	0.15	0.062	0.029	0.023	(.019)	0.021
23	1302	77.4	.6267	0.49	0.42	0.27	0.15	(.046)	--	--	--	0.024
25	1316	76.7	.6120	0.48	0.45	0.35	0.21	0.080	0.034	(.027)	(.021)	0.025
26	1335	75.7	.5879	0.50	0.48	0.39	0.28	0.090	--	0.034	0.029	0.030
27	1347	74.8	.5704	0.62	0.58	0.37	0.20	(.25)	(.23)	(.12)	0.10	0.038
28	1352	74.4	.5623	0.56	0.55	0.42	0.31	(.13)	(.086)	(.065)	(.044)	0.031

Table 4 (cont.) Observed Sky Brightness, 3 October 1960

$(B/B_{\odot})_{\lambda} \times 10^{6}$

Frame	Time	Alt.	μ_o	.37μ	.395μ	.432μ	.47μ	.55μ	.64μ	.72μ	.78μ	.79μ
29	1404	73.5	.5423	0.61	0.59	0.53	0.48	0.12	0.060	0.040	0.036	0.038
31	1419	72.1	.5148	0.71	0.64	0.54	0.36	0.12	(.063)	--	--	0.036
33	1436	69.7	.4808	0.87	0.77	0.53	0.39	0.13	0.072	0.054	0.045	0.038
34	1450	67.3	.4506	1.13	0.97	0.61	0.44	0.16	--	(.069)	(.062)	0.052
35	1454	66.5	.4417	1.37	1.27	0.76	0.46	--	--	--	--	(.059)
36	1457	64.9	.4348	1.40	1.19	0.73	0.54	(.22)	(.12)	(.098)	(.077)	.067
37	1510	60.8	.4042	--	1.32	0.71	0.52	0.26	0.16	0.13	--	0.062
38	1522	57.5	.3745	2.51	2.26	1.49	1.02	(.33)	(.31)	(.24)	(.18)	0.14
39	1526	58.4	.3642	4.21	(3.24)	(1.83)	1.20	--	--	--	--	--
40	1531	54.2	.3511	4.00	3.53	2.11	1.21	0.54	0.39	0.29	0.20	0.18
41	1534	53.4	.3430	3.76	3.52	2.37	1.34	(.52)	--	(.31)	--	0.21
42	1536	52.8	.3378	3.94	3.67	2.72	1.72	0.74	0.54	0.40	0.27	0.23
43	1538	52.4	.3323	3.70	3.63	2.60	1.55	--	--	--	--	(.25)
44	1540	51.7	.3270	3.36	3.10	3.21	2.17	0.91	0.62	0.43	0.33	0.25
45	1544	49.5	.3156	4.25	(3.82)	(3.21)	2.58	(.96)	--	0.58	0.37	0.29
46	1549	47.6	.3014	4.37	4.22	3.44	2.24	(.93)	--	(.46)	--	0.30
47	1551	46.9	.2959	4.73	4.01	3.70	2.46	1.15	0.86	0.65	0.44	0.34
48	1552	46.1	.2929	6.19	4.89	5.34	3.05	1.17	1.00	0.71	0.46	0.37
49	1556	45.4	.2815	5.8	5.19	4.86	3.33	1.25	1.00	0.70	0.47	0.37
50	1601	41.4	.2669	(6.7)	5.94	(5.81)	(4.13)	1.38	1.07	0.84	0.51	0.40

C. Limits of Accuracy

The following factors fix the limits of accuracy of the observed data:

1. Stray light in the instrument
2. Inaccuracy of the photographic process
3. Inaccuracy in the wedge calibration
4. Error in the wavelength identification

Each is discussed below.

1. Stray light in the instrument was evaluated by a series of long test exposures in a light tunnel. For all wavelengths the stray light at $\phi = 144'$ was less than the minimum measurable amount, which was $10^{-8}B_{\odot}$. Another estimate of the upper limit of stray light is given by the observations themselves. The wavelength distribution of the observed sky brightness at 60 kft. follows an approximate λ^{-4} relation. Were the stray light as much as $10^{-8}B_{\odot}$, the stray light would equal the observed brightness in the red at 80 kft., and the resulting spectral distribution would fall off less rapidly than λ^{-4}. Such is not the case; the sky brightness in the red continues to decrease with altitude and the wavelength distribution remains as steep as at 60 kft. I have concluded that stray light in the instrument is negligible except for measurements in the red wavelengths, where for high altitudes it could contribute as much as 10% of the observed values.

2. The accuracy of the photographic process is more difficult to assess, but on general principles it can be said to be accurate within 10%. The inherent photographic inaccuracy was minimized in this experiment by impressing photometric standards on each frame. Thus a reference

of known spectral radiance and the sky itself were photographed under the same conditions. In analyzing the film a characteristic curve of film response was determined for each wavelength region of each frame. Only the observed points that lay on the linear portion of the characteristic curves were given full weight in the final data. Furthermore, a number of careful tests were conducted following the flights to determine if there were any systematic photographic or photometric errors in relative wavelength response of the system. For these tests a glass filter of known spectral transmission was placed in the main spectrograph beam. Exposures were taken with the flying coronagraph pointed at the sun, and with normal illumination on the opal wedge. The photographic frames taken in this way were analyzed by the same method used in the reduction of the flight film, and the brightness distribution obtained was compared with the known transmission of the glass filter. The tests covered a range in brightness from 10^{-4} to $10^{-8} B_{\odot}$; in every case the relative wavelength distribution that was obtained matched the known wavelength characteristics of the filter. This indicated that the intensity of skylight measured at different wavelengths during the flight was correct in the relative sense, and that there were no appreciable systematic errors in the wavelength distribution of the measured values of brightness.

3. The wedge calibration has been discussed in Chapter III. It is held to be accurate to within 10%.

4. The wavelength calibration of the sky spectrograph was described in Chapter III. The dispersion curve was accurately determined. However, in the data reduction there is a possibility of error due to non-linearity of the microdensitometer drive. These errors should be least in the violet where the spectrograph dispersion is the highest. The H and K lines of

ionized calcium appear as a blended depression in the spectrum of the sky recorded in flight and serve as a check on the dispersion curve at 0.395μ. In the red wavelengths, however, where the spectrograph dispersion is low, the wavelength identification is subject to an error of as much as ± 200 Å. The post-flight tests mentioned in paragraph 2 indicate that there are no serious systematic errors in the wavelength identification. Moreover, random errors of wavelength identification should tend to cancel in the overall interpretation. Individual errors could not exceed a few per cent.

It is difficult to assess the effect of the combined error on a given measurement. If all the errors acted in the same direction we find that a given observation in the visible spectral region could be in error by as much as 23% and an observation at peak altitude in the near infrared could be in error by as much as 33%. These are maximum possible errors. The stray light error is not random and represents a systematic error that in all cases raises the value of the observed sky brightness. The error in the photographic process is more probably random in the sense that it could raise or lower the recorded photographic density. The error in the wedge calibration is neither random nor determinable; it is a systematic error of some unknown but constant amount for a given wavelength. Because of the indeterminate nature of the individual sources of error it is not possible to assign a numerical value to the standard deviation of the combined error. It is more realistic to take the empirical evidence from the post-flight laboratory tests that were mentioned earlier: from these we concluded that there are no appreciable errors in the relative wavelength distribution of measured brightness. The error in the absolute scale was not determined by this check.

D. Comparison with Other Data

Other data on the spectral brightness of the aureole at elevated altitudes have been given by Volz (1954) and Newkirk (1956). Volz' observations were made at the Arosa Astrophysical Observatory in the Swiss Alps; Newkirk's data were obtained at various stations in the Rocky Mountains in Colorado. In Figure 16 I have compared their observations with those given here for the stratosphere. The abscissa is a logarithmic scale of wavelength in microns; the ordinate is the observed brightness ratio $B/B_{\odot}$. All values shown have been reduced to the zenith by multiplying by the cosine of the zenith distance. The Volz data points represent observations made in August 1951 at 6.5 kft. at an angle $\phi = 1°.75$ from the center of the sun. Newkirk's curves give values obtained on three days in January 1955 at Flagstaff Mountain (6.8 kft.), Severance (8.8 kft.), and Arapahoe Basin (11.2 kft.), Colorado. His data are for $\phi = 2°.4$. Dr. Newkirk also made a series of aureole measurements at $\lambda = 0.82\mu$; I have not shown his infrared data in Figure 16 since they were obtained on dates different from his other observations that are shown. It is not surprising that the Volz and Newkirk curves show different brightness values at the common altitude of about 6.5 kft., since the tropospheric aureole varies in brightness according to surface weather and low-level atmospheric pollution (Volz, 1954; Newkirk, 1956).

We note that the ratio of the ground observations to the balloon observations in every case exceeds the pressure ratio between the two altitudes. Were only the pure Rayleigh sky observed at each point this would not be the case; the greater difference shown here merely indicates the increased turbidity near the surface of the earth.

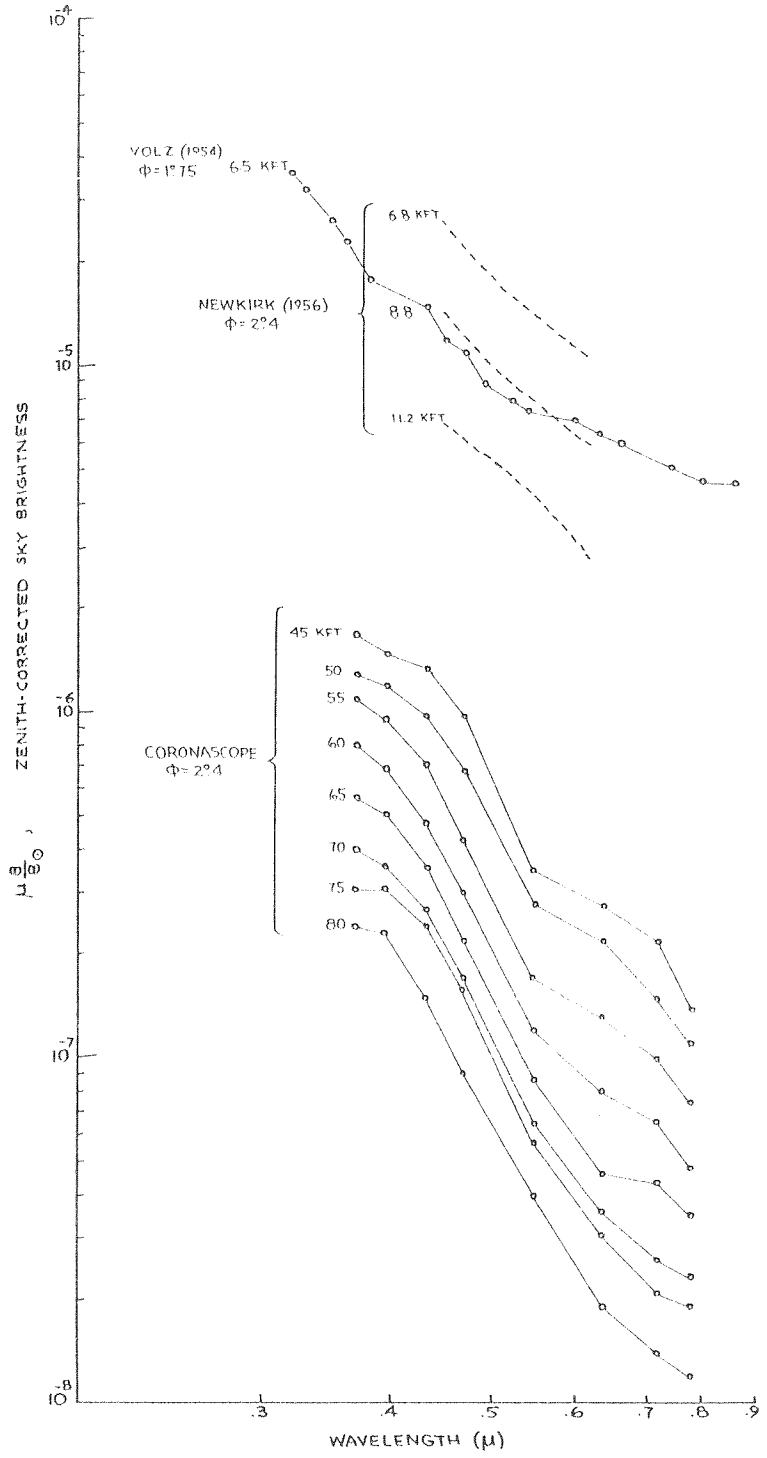

Figure 16

Comparison of high altitude spectral observations of the solar aureole. All values are multiplied by $\mu_o = \cos Z_o$.

A significant conclusion from the comparison is that the wavelength gradient grows steeper with altitude. If the brightness at any altitude is expressed in the exponential form $B = B\lambda^{-M}$, we find that the Volz and Newkirk observations indicate $M \simeq 2.5$. From the Coronascope data the value of the exponent at 45 kft. is about 3.4 and at 80 kft. it is slightly larger than 4. We can anticipate the results in the next chapter by attributing the higher value of M at high altitudes to the decrease in the number of large particles with height in the atmosphere.

CHAPTER V

INTERPRETATION

A. Method

In this chapter I propose an interpretation of the observed spectral sky brightness data in terms of two atmospheric scattering components: a molecular, or Rayleigh component, and a non-molecular, or Mie component. The method I used is outlined below:

1. A theoretical sky brightness due to Rayleigh scattering was calculated for each of the data points of Table 4 of Chapter IV. The result is a table of molecular sky brightness, each point of which is somewhat less in magnitude than the corresponding observed value in Table 4.
2. The Rayleigh brightness values were subtracted, point for point, from the observed data.
3. The difference between the observed and the Rayleigh brightness is called the residual sky brightness; it was presumed to be the result of Mie scattering by non-molecular particles (aerosols) in the atmosphere above the altitude of observation.
4. The Mie theory was used to calculate the sky brightness that would result from a variety of theoretical particle size distributions. These calculated brightness values were compared with the observed residual brightness.
5. A number of different distributions were found that produce sky brightness equivalent to the observed data. The simplest distribution was selected and compared with other estimates of aerosol size distributions.

There are three sources of possible error in the interpretation method. They are:

a. Inaccuracy in the observations

b. Neglect of Rayleigh-Mie interaction and of atmospheric emission

c. Error in the Rayleigh calculation.

A discussion of each is given below. To the list could be added the approximations inherent in the theories of Rayleigh and Mie; these were mentioned in Chapter II and are a minor source of doubt in the interpretation.

a. Observational Inaccuracy - In Chapter IV I made the claim that the observations are correct within a 10 to 20% limit. When we subtract the Rayleigh brightness from the observations the relative inaccuracy of the difference is increased. Thus, if the Rayleigh value is half as large as the observed, and if the observed data are accurate within 10%, the difference is accurate only within 20%. The smaller the difference between observed and Rayleigh brightness, the larger is the inaccuracy in the residual brightness. In every case the difference between observed and Rayleigh brightness is larger than the observational uncertainty. The observations indicate the existence of a definite non-Rayleigh sky brightness at all altitudes.

b. Interaction Terms and Atmospheric Emission - Step three of my method employs the relation,

$$B_{observed} - B_{Rayleigh} = B_{Mie} \tag{23}$$

where B is brightness. A more complete and correct formula would be

$$B_{observed} - B_{Rayleigh} = B_{Mie} + B_{interaction} + B_{emission} \tag{24}$$

where $B_{interaction}$ accounts for the effects of multiple scattering between Rayleigh and Mie particles, and $B_{emission}$ represents the airglow brightness. In using the simpler form I have assumed that the neglected terms contribute a negligible portion of the residual sky brightness.

Order-of-magnitude examples show that the Rayleigh-Mie interaction effects can be ignored in the region of this study. There is no doubt that the Mie particles are exposed to radiation scattered by neighboring Rayleigh particles as well as to direct solar radiation. Rayleigh particles, in turn, receive a fraction of their incident radiation from Mie particle scattering. However, these multiple effects are greatest in the lowest parts of the atmosphere where densities are greatest. At 45 kft. the sky brightness near the sun in the violet is about six millionths of the brightness of the solar disk. We need not consider the source of scattering to conclude that the ratio of scattered to direct radiation incident on a particle at that altitude is less than 6×10^{-6}. This represents an upper limit for the region of this study, since for longer wavelengths or higher altitudes the ratio is decreased. We conclude that there is no loss of accuracy in neglecting the Rayleigh-Mie interaction effects.

The airglow is less easily extinguished. Theoretical estimates of the intensity of the day airglow are in general agreement (Chamberlain, 1961) but there have been no precise measurements that confirm the predicted levels. It is well established that during the day atomic and molecular emission occurs in the upper stratosphere producing visible radiation that shows the same spectral features, and with intensities at least as great as are observed in the twilight airglow (Chamberlain, 1961). The more prominent features expected in the day airglow are the red line of OI at 6300 Å, the sodium D lines at 5890 and 5896 Å, the

green line of OI at 5577 Å, and the first negative bands of molecular nitrogen, N_2^+, which peak at 3914 Å and spread over the visible spectrum from about 4700 Å to the violet. The N_2^+ system is made up of bands about 50 Å in width with sharp bandheads on the long wavelength ends; the other expected features are narrow atomic emission lines. All the expected dayglow features would be smeared to a continuum level by the wide instrument function of the spectrograph which was flown in our experiment. They would not produce recognizable features in the low dispersion sky spectra. If the intensities of the individual emission lines and bands were of magnitude comparable with the scattered solar radiation, however, they would contribute a significant fraction to the sky continuum recorded on the Coronascope flights. There is general agreement that the atmospheric emission originates in regions between 50 and 150 km. (150-500 kft.) (Dalgarno, 1958). Rocket and satellite measurements made above the stratosphere where scattered light is small should be able to provide brightness estimates of dayglow emission that apply to lower regions as well. Early rocket observations by Miley, Cullington, and Bedinger (1953) indicated that the brightness of the day sky at 135 km., attributed to dayglow, was about 1% of the sea-level brightness. Between 32 and 72.5 km. they measured the sky brightness in narrow spectral bands to be 2 or 3% of the ground value. In the brightness units of my report, these measurements indicate sky brightness values of 10^{-6} to 10^{-5} $B_\odot$. The work of others (Morosov and Shklovsky, 1956; Bates and Dalgarno, 1954) has indicated that the Miley _et al_ results were unreasonably high, probably indicating an instrument brightness level. A later rocket flight by Berg (1955) indicated that the total sky

brightness above 80 km. was less than 10^{-3} times that given by Miley et al. A recent attempt by Wallace (1961) to obtain spectra of the day airglow from a balloon-borne spectrograph at 38 km. failed to reveal any emission features. Wallace concluded from sky continuum measurements that the maximum possible airglow brightness at 38 km. was less than 20% of the "blue-sky intensity" at that altitude. Theoretical estimates by Brandt (1958) and by Chamberlain and Sagan (1960) predict an upper limit of about half this amount. An extrapolation of the "blue-sky" brightness reported here gives a value of about 10^{-8} $B_{\odot}$ for the sky in the violet at 38 km.; using Wallace's estimate this fixes the limiting day airglow brightness at about 10^{-9} $B_{\odot}$. The flying coronagraph data given in this thesis also contradict the Miley et al results, since I find the sky brightness in the aureole at 24 km. to be an order of magnitude less than the brightness reported by Miley et al at higher altitudes and at angles farther from the sun. If the rocket observations represent a true measure of the dayglow intensity it is unlikely that the brightness of the sky at lower altitudes could fall much below it. An emitting region high in the stratosphere or ionosphere would provide a base level of brightness for observations made at lower altitudes. If we adopt the data of Berg and of Wallace, and the estimates of Chamberlain and Brandt, we conclude that the dayglow could account for at most 10% of the residual sky observations obtained with the flying coronagraph.

c. Error in the Rayleigh Calculation - The calculation of the Rayleigh brightness given by Coulson, Dave, and Sekera (1960) was the basis for my interpretation. Their numerical computations of the Chandrasekhar theory present exact solutions of the molecular scattering problem for given conditions of observation. The defining conditions

are (1) position in the atmosphere, (2) direction of observation with respect to the sun and to the zenith, and (3) wavelength of measurement. They are represented by the five parameters τ, μ_o, μ, ϕ, and A discussed in Chapter II. The source of error in adopting the Coulson, Dave, and Sekera computations lies in the assignment of numerical values to the five parameters for each of the points of observation. The three parameters μ_o, μ, and ϕ define the direction of observation and are accurately determined in the flying coronagraph data. The parameter τ, which represents the optical depth due to scattering, is not so well established. In Section B of this chapter I describe the manner in which it was determined; basically, I have used Deirmendjian's theoretical values for the optical depth due to Rayleigh scattering at sea level (1955) corrected by the atmospheric pressure ratio at the altitude of observation. In doing so I assume a constant atmospheric composition from sea level to the top of the stratosphere. Error in this assumption, or in the sea-level optical depths given by Deirmendjian, would have a direct effect on the Rayleigh solutions obtained. I have also neglected the contribution of Mie scattering to the optical depth, since Deirmendjian's values give only the Rayleigh scattering component. However, in the stratosphere the optical depth due to Mie scattering is about an order of magnitude less than the optical depth due to Rayleigh scattering. The effect of the Mie optical depth in the Rayleigh calculation is less than the error in the observations. The albedo, A, is the least certain parameter and represents a serious source of doubt in the Rayleigh calculation. In Figure 17 I have taken some points from the Coulson, Dave, and Sekera solution to illustrate the dependence of the Rayleigh-Chandrasekhar solution on albedo. The abscissa is the albedo, the

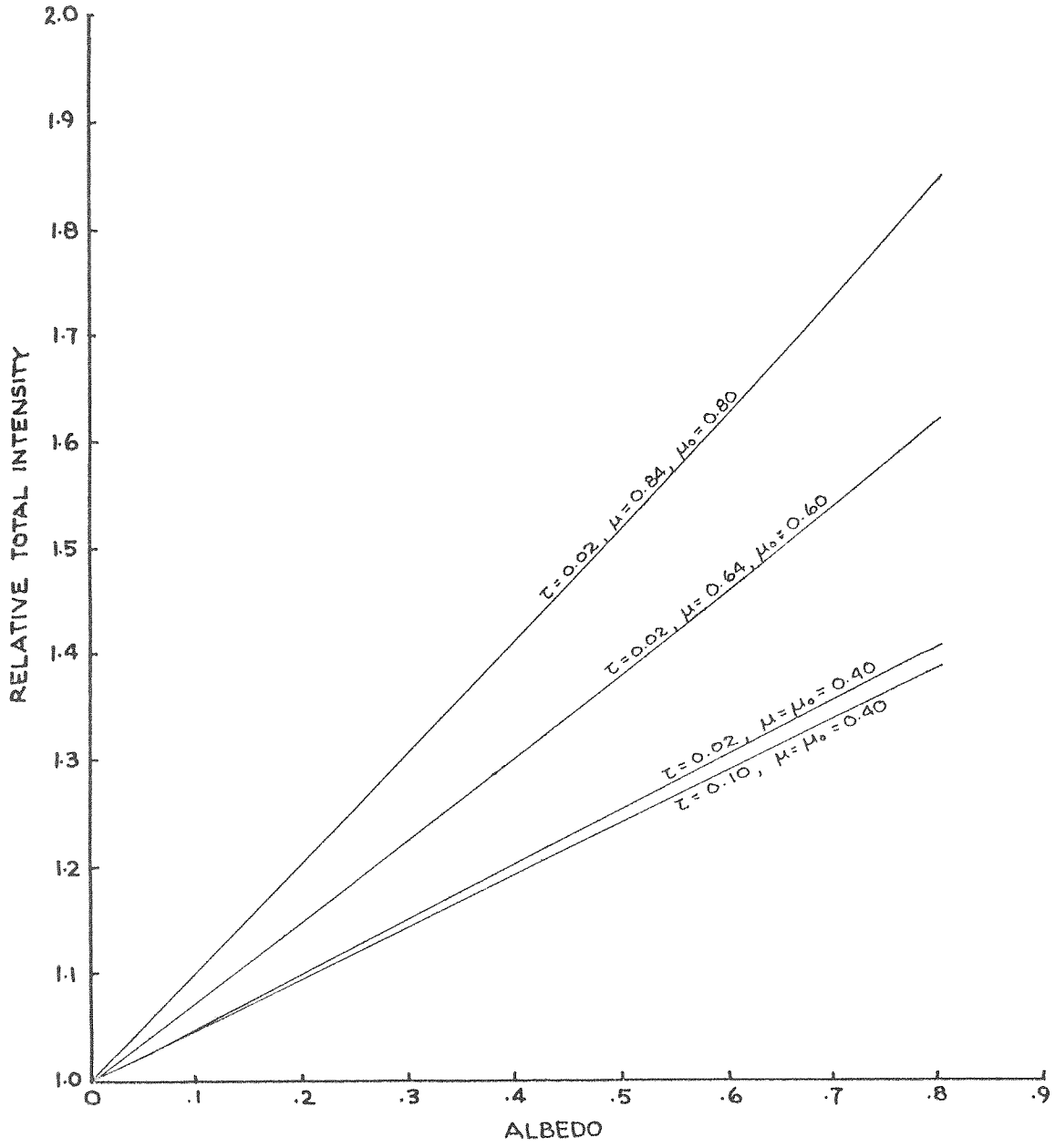

Figure 17

Effect of albedo on Rayleigh-Chandrasekhar calculation for $\phi = 0$
(Coulson, Dave, and Sekera, 1960)

ordinate is total scattered intensity I on a relative scale. Curves are shown for combinations of τ, μ, and μ_o that represent the range of the Coronascope observations. All curves are for $\phi = 0$. We note that the change in the total scattered intensity is approximately a linear function of A and that it is most pronounced for small zenith angles. In the context of the Rayleigh problem applicable to high altitude observations, the albedo represents the reflectivity of the hemisphere beneath the point of observation; it includes the combined and interlocked effects of the ground albedo, the upward Rayleigh radiation, and the upward radiation of haze and clouds beneath the balloon. The albedo was not measured on the Coronascope flights. I have estimated the ground albedo based on the measurements of Krinov (1960) and on my knowledge of the terrain along the flight track. The contribution of the upward Rayleigh radiation was obtained from Coulson's theoretical solution of the problem for a point at the top of the terrestrial atmosphere (1959). The haze and cloud contributions were disregarded. I used a mean albedo that was obtained by interpolating between the Krinov ground albedo and the Coulson extraterrestrial albedo. The definition of the mean albedo, and a discussion of the Krinov and Coulson values used are given in the next section. A cloud correction may have been necessary, since on the flight of 3 October 1960 light cirrus and patches of cumulus drifted beneath the balloon and were concentrated in the sky west of the balloon track. They are shown dramatically in the lapse-camera record taken by the down-pointed camera on the gondola. The cumulus were probably the more serious contaminant, though at no time did they fill more than 1/10 of the 20° field of the down camera. By neglecting the haze and cloud albedo contribution I have possibly underestimated the true albedo that

was effective during the flight. However, the size of this possible error is no more than that of the error introduced by uncertainty in the ground albedo, which is the principal contributor in the red wavelengths. The Krinov albedo, compared with other less extensive measurements, is a high estimate (Penndorf, 1956; Fritz, 1949); the possible error in neglecting the clouds is in the opposite direction. At best the magnitude and wavelength behavior of the albedo used are estimates that lie within 10% of the true values.

An additional uncertainty in the Rayleigh calculation rests in the basis of the Chandrasekhar solution of the planetary scattering problem. In that solution the atmosphere is approximated by a medium in which radiation is scattered without being absorbed. No allowance is made for the effect of optical depth due to absorption. In the visible region of this study the greatest atmospheric absorption occurs in the Chappuis bands of ozone. These bands, which extend from .44 to .74μ, are sufficiently strong to produce an absorption optical depth that exceeds the corresponding scattering optical depth for much of the altitude and spectral range of my data. The solution of the atmospheric transfer problem that includes absorption effects is quite complicated. Were the ozone uniformly mixed through the atmosphere it would be feasible to modify the Chandrasekhar solution in a way that would allow use of the Coulson-Dave-Sekera solutions. But this is not the case. Since the ozone is concentrated in a narrow layer of the stratosphere the ratio of absorption to scattering optical depths through the atmosphere is a strong function of altitude. In order to make use of the Chandrasekhar solution I followed a suggestion by Dr. Sekera and made the approximation that the ozone above the balloon at any altitude acts as a filter that

does no more than attenuate the incoming solar radiation. This treats the overhead ozone as though it were concentrated in a single layer at the top of the atmosphere; it is the same method used by Dave and Sekera as a first approximation of the ozone absorption effect (1959). In a later paper Sekera and Dave modified the filter approximation to allow for primary scattering within the ozone filter layer (1961). By the simple filter approximation the ozone attenuates the solar radiation before it enters the atmosphere of the earth. The amount of attenuation is fixed by the absorption optical depth of the ozone layer at the wavelength concerned and by the zenith angle of the sun. Since the sky brightness is proportional to the incoming solar flux it will be reduced by the same amount as the observed solar brightness. Both sky and sun brightness will be attenuated by the factor $\exp(-\tau_{abs/\mu})$ where τ_{abs} is the optical depth due to absorption in the ozone layer. Since the sky brightness measurements of this study are made relative to the observed sun brightness, and since both sky and sun are attenuated by the same factor, the ozone absorption in the filter approximation is canceled: the ratio of sky to sun brightness at any wavelength is the same whether the ozone is there or not. A question is raised by the fact that the balloon penetrated the ozone layer during the upper portion of the flight. This has little effect on the filter approximation validity since it is only the ozone above the observer that attenuates the direct incoming radiation. The ozone which is, so to speak, "underfoot" acts to reduce the effective albedo by the factor $\exp(-2\tau_{abs/\mu})$. In the most severe case, in which all the ozone is beneath the balloon, the albedo could be reduced by about 10% in the center of the Chappuis bands. This might cancel the additive effect of a cloud or two on the albedo. In any case

the albedo error introduced by the ozone filter approximation is within the range of certainty of the albedo used in the Rayleigh calculation. The filter approximation itself is the more serious cause for doubt.

Departure of the ground from a true Lambert law reflecting surface introduces an additional error in the Rayleigh calculation, since the Chandrasekhar solution is based on this assumption. Lambert's law of diffuse reflection applies to a perfectly diffuse radiator and states that for such a surface the diffusely reflected light is isotropic in the outward hemisphere, independent of the direction of the incident light. By Lambert's law an element of surface appears equally bright when observed from any direction. Obviously, natural terrain is not a perfect diffuser in this sense.

A final uncertainty in the Rayleigh calculation arises from the approximation that the atmosphere is plane-parallel --- a basic assumption in the Chandrasekhar solution. The error of this approximation is greatest for large zenith angles of the sun. All the observations recorded here were made at zenith angles smaller than 75°, at which the sphericity correction should be of minor importance. Fesenkov has considered the effects of sphericity on daytime sky brightness and has concluded that at a zenith angle of 75° the optical depths determined for a plane parallel atmosphere begin to show serious error (1955). According to Deirmendjian (1959a) the error is about 4%. It is not certain that introducing Fesenkov's corrections to the optical depths would result in an improved solution, since his calculations were made for the case of single scattering and zero ground albedo. For the purpose of my analysis the plane-parallel approximation seems adequate.

B. Calculation of the Rayleigh Component

Chandrasekhar's analytical solution of the Rayleigh scattering problem and the numerical solution by Coulson, Dave, and Sekera were mentioned in Chapter II. Coulson, Dave, and Sekera have tabulated the total emergent intensity, I, as a function of 16 different values of μ, 3 values of A, and 7 values each of μ_o, ϕ, and τ. The method of analysis that I have used requires accurate values of I at points of intermediate values of the five parameters given above, necessitating either an interpolation between the Coulson, Dave, and Sekera points or a complete calculation of the Chandrasekhar-Rayleigh solution. I used the first alternative.

The mathematical problem presented by this choice was that of an interpolation in a table of five dimensions in which the arguments of each dimension are given in unequal increments. I required the curve of interpolation to fit four of the tabulated points in each of the arguments τ, μ_o, μ, and ϕ, and to fit all three of the tabulated points in the argument A. The interpolated solution was therefore that of a third order curve in each of four dimensions, and a quadratic curve in the fifth. An interpolation of this sort was required for 837 different data points.

The magnitude of the problem required the use of a large electronic computer. The calculations were done on the CDC-1604 digital computer at the National Bureau of Standards in Boulder. Dr. Sekera kindly supplied the Coulson, Dave, and Sekera table on punched cards. The technique of interpolation used for the problem was the method of divided differences, which is described for the one-dimensional case by Kunz (1957).

The method is extended to the many-dimension case by a process of repeated application, resulting in a geometrical increase in the size of the problem without major change in its complexity.

The values of the five arguments used to define each data point of the solution were obtained as described below:

(1) μ_o = cosine of the zenith angle of the sun at the time of the observation, was obtained from the position and time coordinates of the balloon by the method described in Chapter IV.

(2) μ = cosine of the zenith angle of the direction of observation, was taken as $\mu = \mu_o$.

(3) ϕ = azimuthal angle of the direction of observation, measured from the center of the solar disk, was fixed at $\phi = 144'$ by the region of the sky spectrum that was analyzed.

(4) τ = optical depth at the point of observation = $\tau(\lambda, h')$. The Rayleigh optical depth was used, defined as

$$\tau(\lambda, h') = \int_{h'}^{\infty} \kappa_\lambda (h)\, \rho(h)\, dh \qquad (25)$$

where

h' = the height of the point of observation

$\kappa_\lambda(h)$ = mass scattering coefficient according to the Rayleigh law

$\rho(h)$ = atmospheric density

Under the assumptions of an exponential atmosphere in which the scattering coefficient is independent of height we can write the last equation as

$$\tau(\lambda, h') = \tau(\lambda, h=0)\, \frac{p}{p_o}\, (h') \qquad (26)$$

where $\frac{p}{p_o}$ is the ratio of the atmospheric pressure at height h' to the pressure at sea level. Equation (26) was used to obtain the argument τ for the Rayleigh calculation. The values of $\tau(\lambda, h=0)$ were taken from Deirmendjian (1955), who computed the normal optical depth of the atmosphere at sea level from vertical density and composition data. The h=0 values that were used are given in Table 5.

Table 5. Normal optical depth of the Rayleigh atmosphere at sea level (Deirmendjian, 1955)

λ	$\tau(\lambda, h=0)$
0.37	0.505
0.395	0.382
0.40	0.363
0.432	0.263
0.44	0.243
0.47	0.182
0.55	0.097
0.64	0.051
0.67	0.042
0.72	0.0312
0.76	0.0253
0.78	0.0228
0.79	0.0218
0.80	0.0208
0.82	0.0190

The pressure ratio, $\frac{p}{p_o}$, was obtained from the record of the altimeter that was carried on the balloon gondola. The minimum τ given in the Coulson, Dave, and Sekera table is $\tau = 0.02$. For values of $\tau < 0.02$, I used a linear extrapolation to $I = 0$ at $\tau = 0$.

(5) A = albedo, representing the combined reflectivity of the air and ground beneath the point of observation. Three different values of A were used for the analysis of each data point. These were: A ground albedo, $A_k(\lambda)$ as given by Krinov (1960). Ground conditions beneath the Coronascope flights most closely fit Krinov's Class C, Curve 1b classification, described as "coniferous forests in summer, dry meadows, grass in general." The Krinov values used are given in Table 6. A theoretical albedo, $A_c(\lambda,\mu_o,A_k)$ computed by Coulson (1959) for the top of the terrestrial atmosphere and based on the complete solution of the transfer problem for radiation that emerges from a Rayleigh atmosphere. The albedo computed by Coulson is a function of wavelength, solar zenith angle, and ground albedo; it is in general greater than the ground albedo. It does not include the effect of ozone absorption. The Coulson albedo table used is given in Table 7; an interpolation in this table was carried out to find the Coulson albedo for each point of observation. This interpolation was included within the major interpolation program in the electronic computer calculation. The divided difference interpolation method was also used for this sub-interpolation.

Table 6. Krinov ground albedo, A_k, for conditions of Coronascope flights (Krinov, 1960)

λ	A_k
0.37μ	0.030
0.395	0.032
0.432	0.039
0.47	0.044
0.55	0.088
0.64	0.078
0.72	0.189
0.78	0.278
0.79	0.282

Table 7. Reflectance A_c of the top of a Rayleigh atmosphere, according to Coulson (1959)

		λ					
A_k	μ_o	0.315μ	0.40μ	0.50μ	0.60μ	0.70μ	0.80μ
0	0.02	0.754	0.638	0.565	0.503	0.430	0.325
0	0.10	0.705	0.552	0.396	0.247	0.154	0.094
0	0.40	0.550	0.304	0.152	0.079	0.044	0.024
0	0.80	0.400	0.181	0.085	0.039	0.022	0.013
0	1.00	0.345	0.148	0.068	0.033	0.017	0.009
0.25	0.02	0.791	0.712	0.665	0.625	0.574	0.494
0.25	0.10	0.752	0.643	0.536	0.427	0.362	0.319
0.25	0.40	0.623	0.445	0.345	0.298	0.276	0.285
0.25	0.80	0.492	0.347	0.293	0.271	0.260	0.257
0.25	1.00	0.450	0.322	0.280	0.264	0.256	0.255
0.80	0.02	0.922	0.910	0.904	0.896	0.885	0.865
0.80	0.10	0.918	0.892	0.866	0.842	0.826	0.815
0.80	0.40	0.860	0.830	0.812	0.805	0.803	0.800
0.80	0.80	0.811	0.798	0.798	0.798	0.798	0.799
0.80	1.00	0.794	0.792	0.794	0.796	0.798	0.799

A mean albedo, A_m, which lies between the values A_c and A_k at a point fixed by the atmospheric pressure ratio at the altitude of observation. The relation that defines A_m is

$$A_m\,(h,\lambda,\mu_o,A_k) = A_c - \frac{p}{p_o}\,(A_c - A_k) \qquad (27)$$

for the case $A_c > A_k$

and

$$A_m\,(h,\lambda,\mu_o,A_k) = A_c - (1 - \frac{p}{p_o})\,(A_c - A_k) \qquad (28)$$

for $A_c < A_k$

The computed Rayleigh sky brightness is shown in Figures 18 through 26, along with the observed brightness values. Each figure shows the data for one wavelength region; all refer to the flight of 3 October 1960. The abscissa is altitude in thousands of feet above sea level. The ordinate represents sky brightness in units of $B_\odot$ (the brightness of the mean solar disk seen at the altitude of observation in the wavelength concerned). The ordinate scale is logarithmic. Each observed point refers to one photographic frame. All data are for a scattering angle of 2.4° from the center of the sun. The observed points have been corrected for the effect of instrument function. The Rayleigh calculated brightness curves are shown as solid lines. The Rayleigh curve labeled K was calculated for the Krinov (ground) albedo; the curves labeled C and M were calculated for the Coulson albedo and mean albedo respectively. To the scale of the diagrams the C and M curves coincide. The effect of the albedo choice is evident in each of the figures. We note that the K and

C curves are most widely separated in the short wavelengths, where for $\lambda = .37\mu$ they differ by about 20%. For wavelengths longer than $.64\mu$ they are nearly coincident. This behavior is not surprising; it results from the choice of albedo values used. We expect little difference between the Krinov and Coulson albedos in the red because of the increased transparency of the atmosphere in the longer wavelengths of the visible region. This can be seen in Table 7 where the Coulson albedo was given; there we note that in the long wavelengths the atmosphere contributes little to the albedo, except at large solar zenith angles. As a consequence the Rayleigh solution is especially sensitive to the ground albedo in the red spectral range. The bifurcation of the curves between 60 and 80 kft. is a consequence of the changing zenith angle during the flight. The lower branch consists of points observed during balloon ascent while the upper branch shows data obtained in descent when the zenith angle of the sun was increasing. The earliest observations were made at mid-morning at about 65 kft. The difference between the observed and the Rayleigh brightness points represents the non-Rayleigh or residual sky brightness.

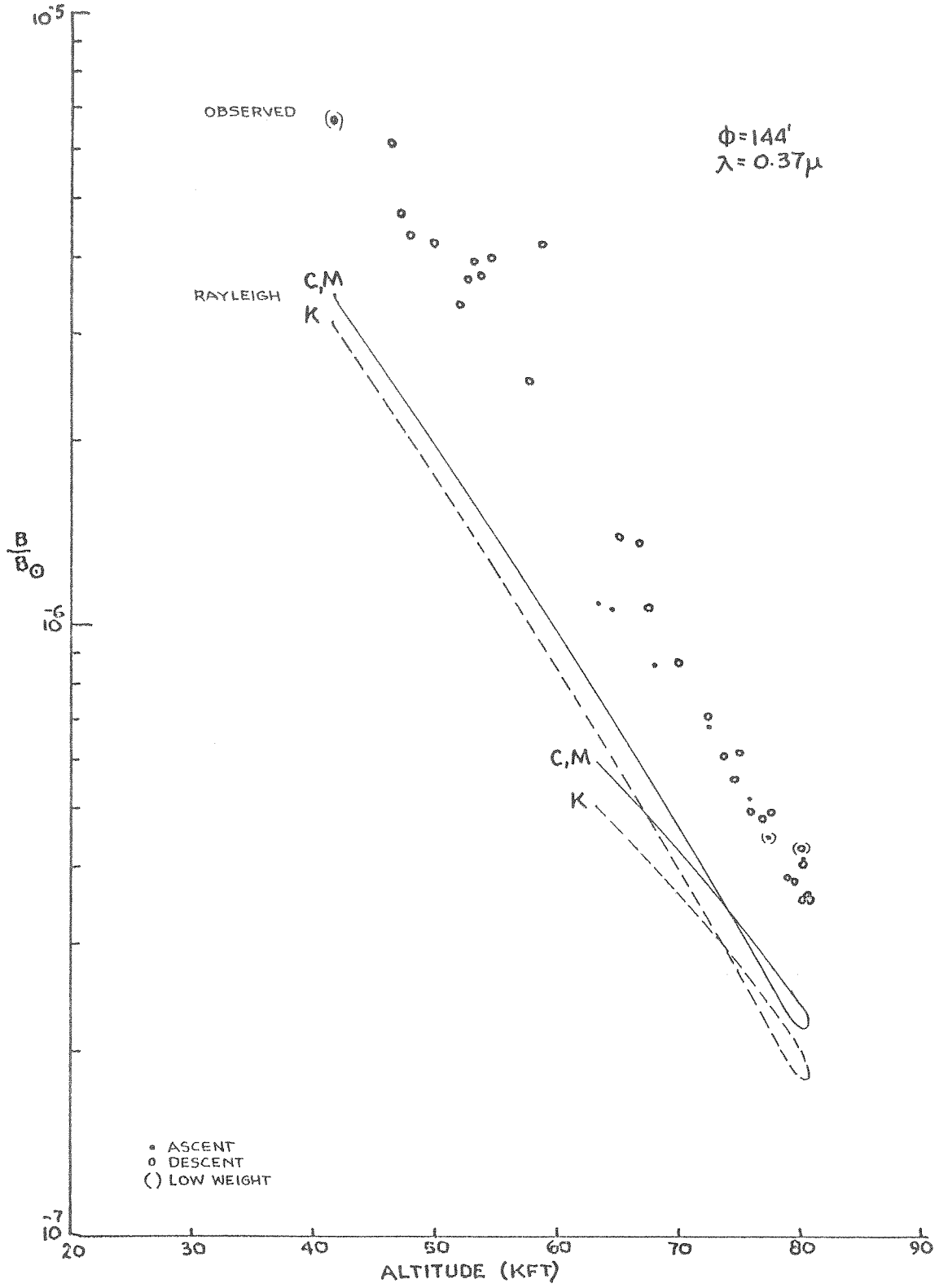

Figure 18

Observed and Rayleigh sky brightness for $\lambda = 0.37\mu$

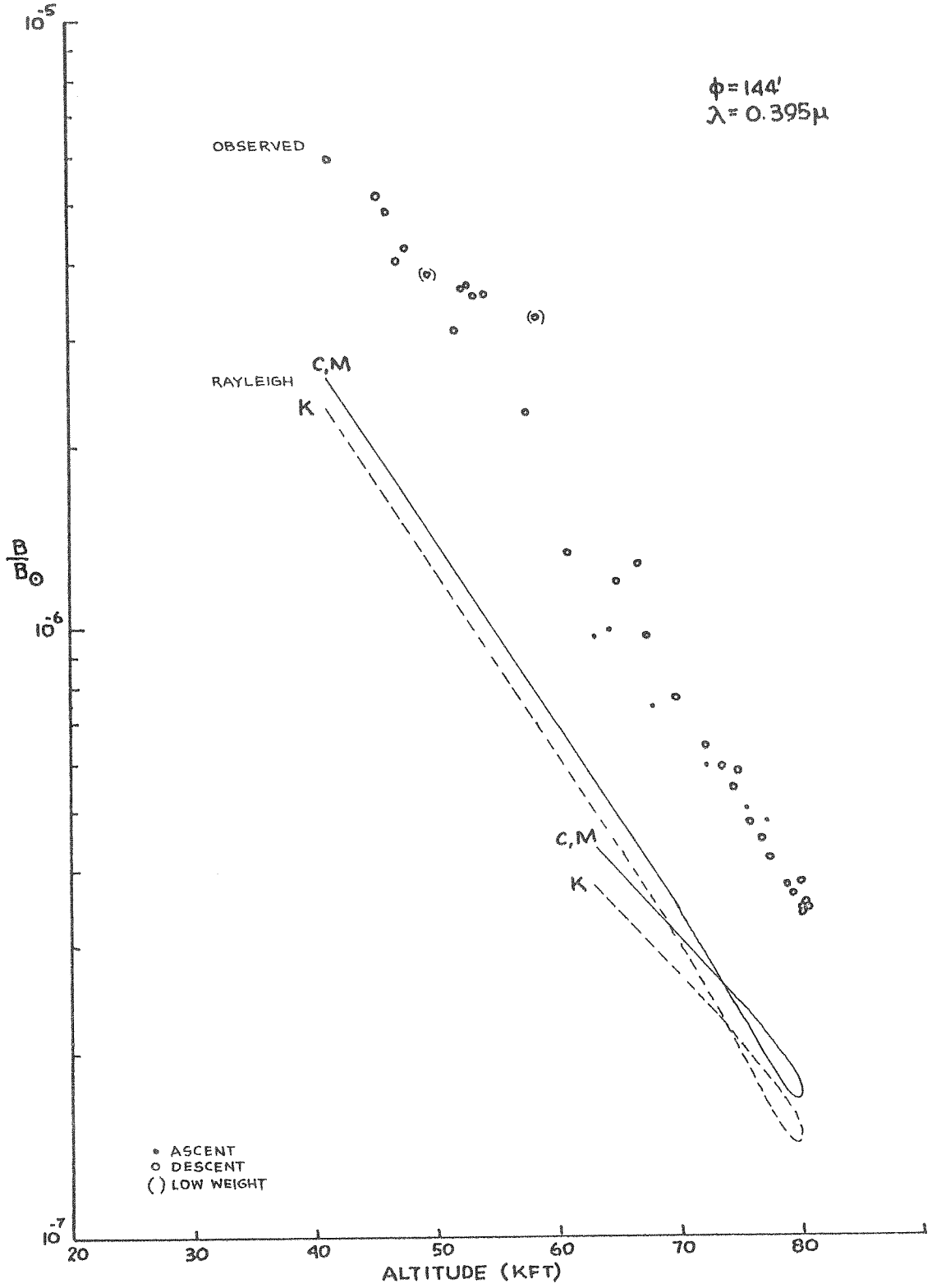

Figure 19

Observed and Rayleigh sky brightness for $\lambda = 0.395\mu$

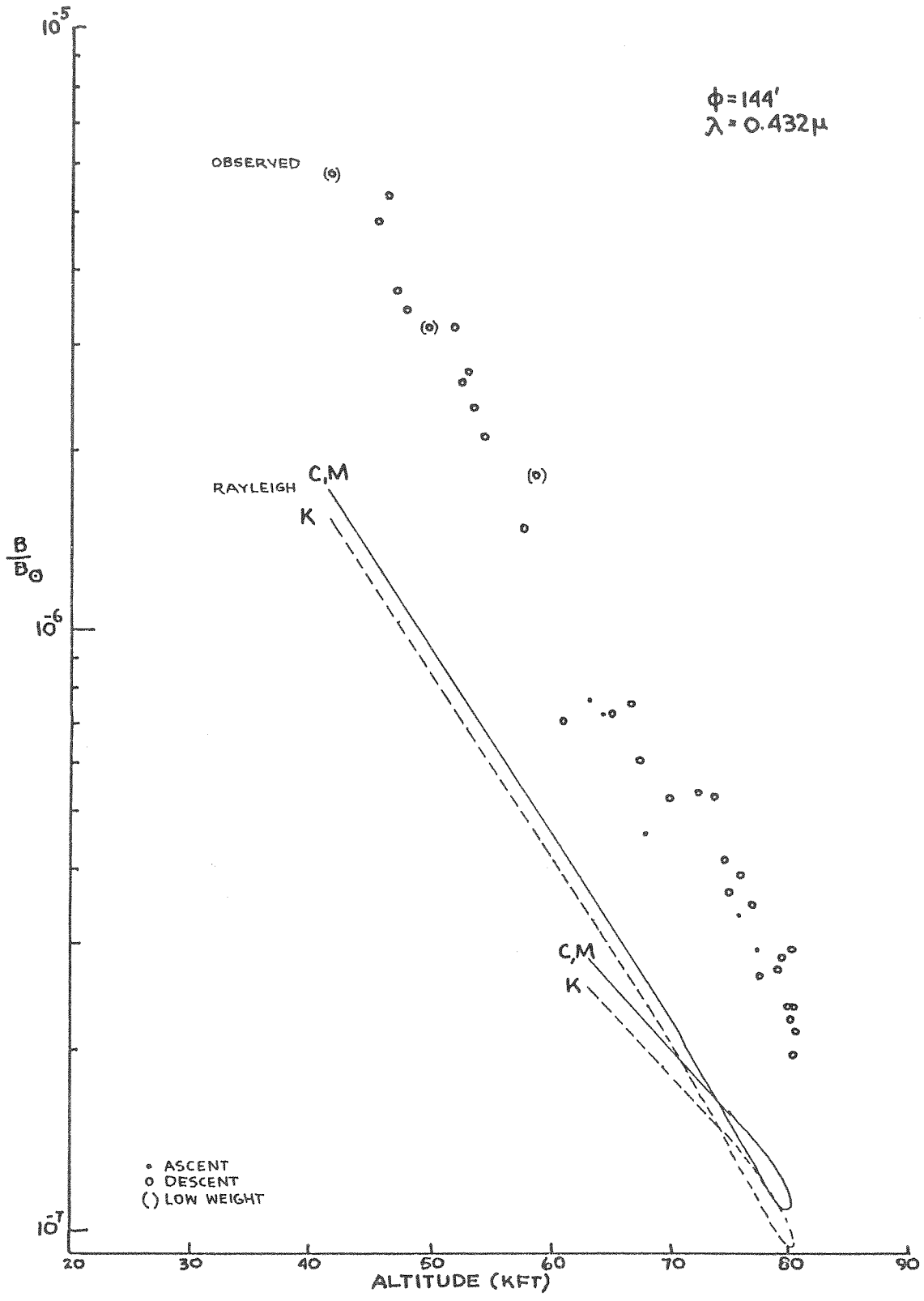

Figure 20

Observed and Rayleigh sky brightness for $\lambda = 0.432\mu$

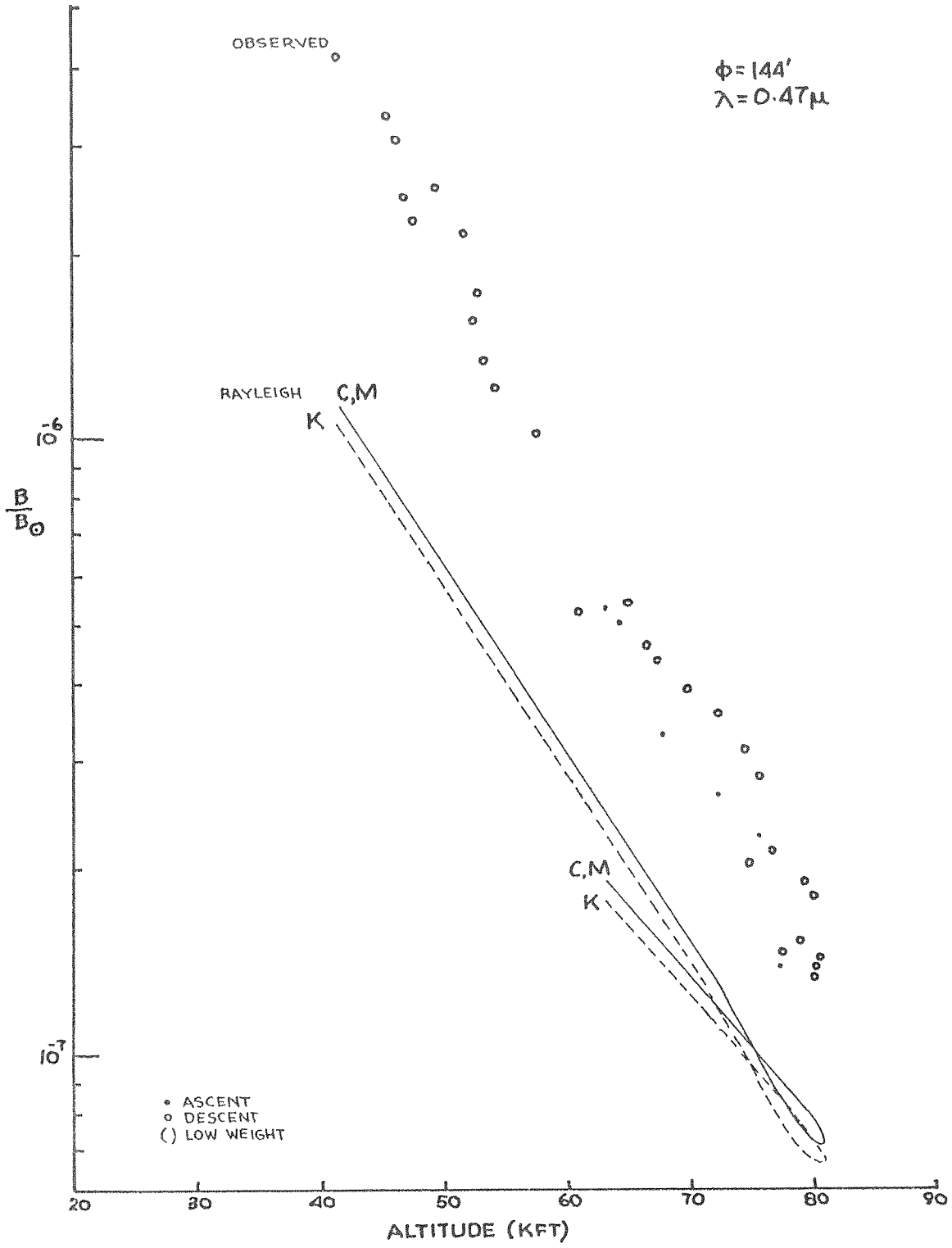

Figure 21

Observed and Rayleigh sky brightness for $\lambda = 0.47\mu$

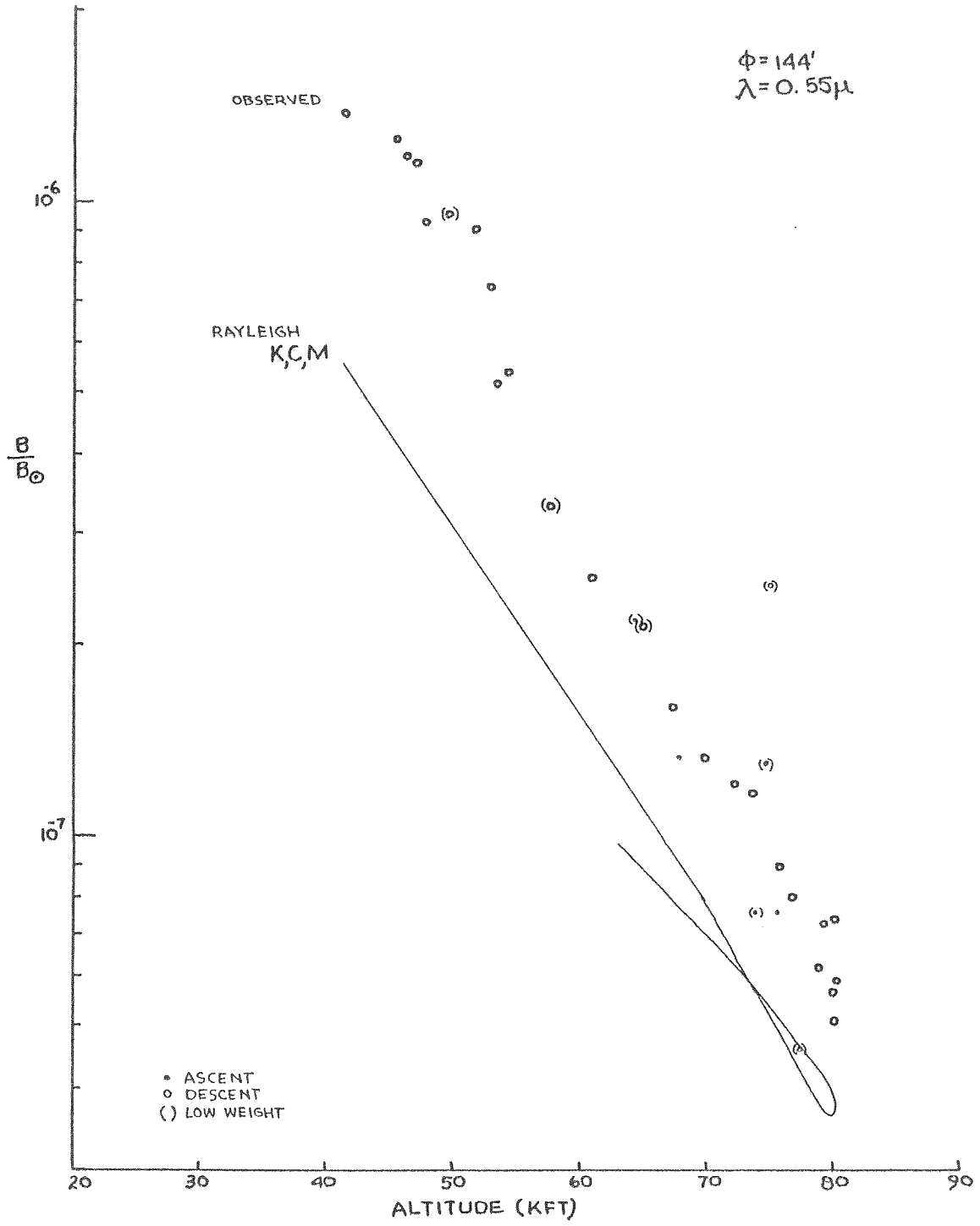

Figure 22

Observed and Rayleigh sky brightness for $\lambda = 0.55\mu$

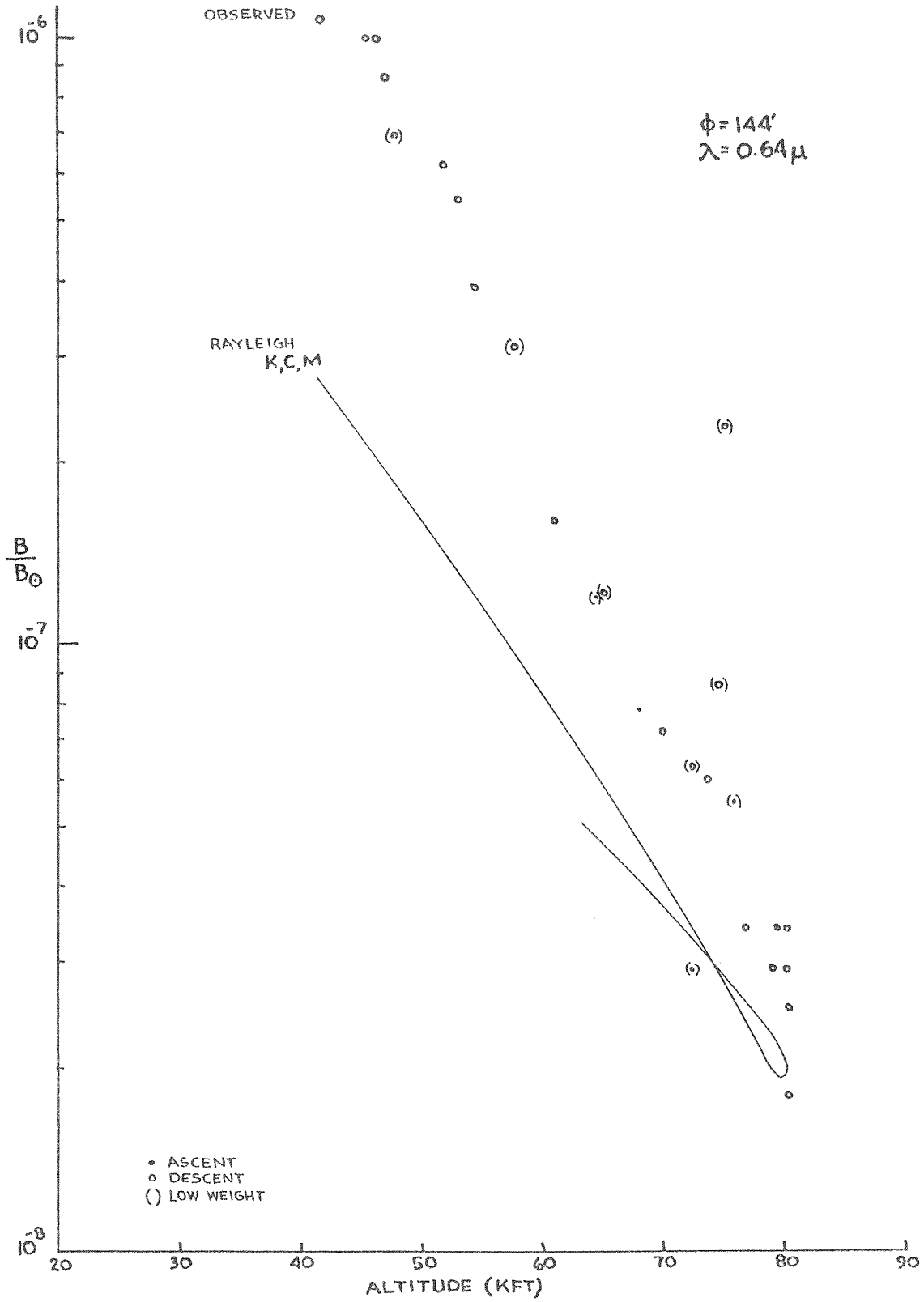

Figure 23

Observed and Rayleigh sky brightness for $\lambda = 0.64\mu$

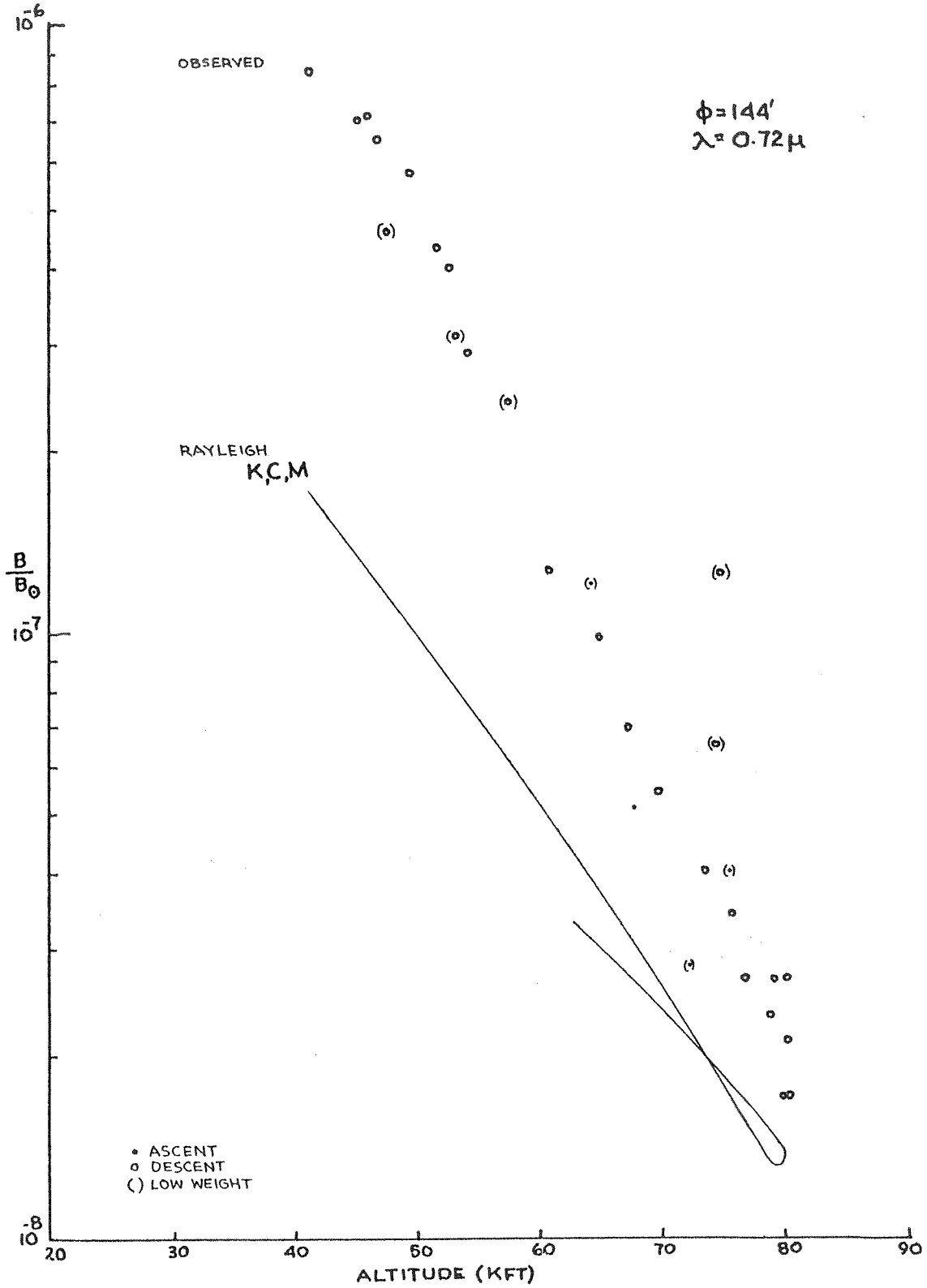

Figure 24

Observed and Rayleigh sky brightness for $\lambda = 0.72\mu$

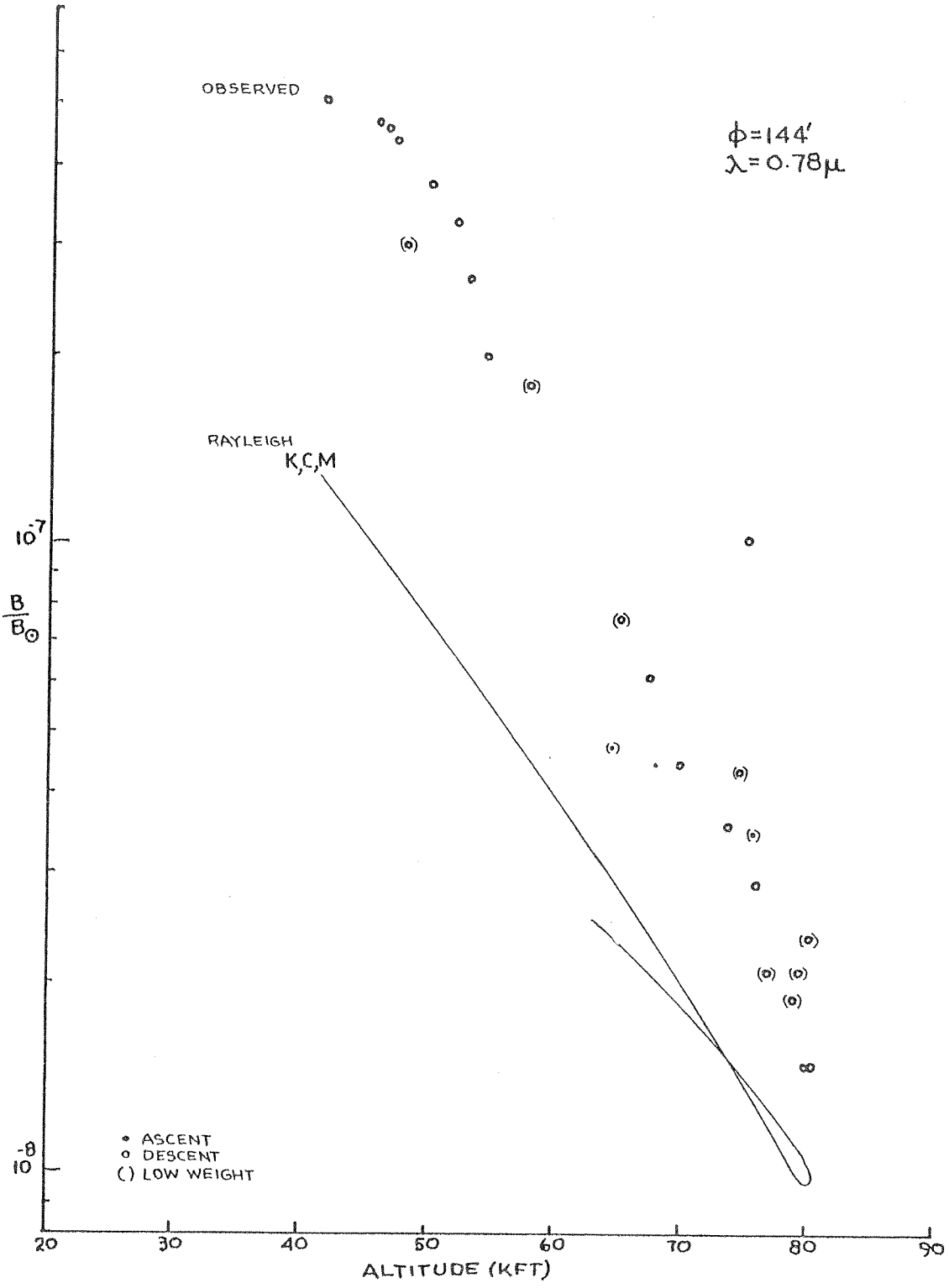

Figure 25

Observed and Rayleigh sky brightness for $\lambda = 0.78\mu$

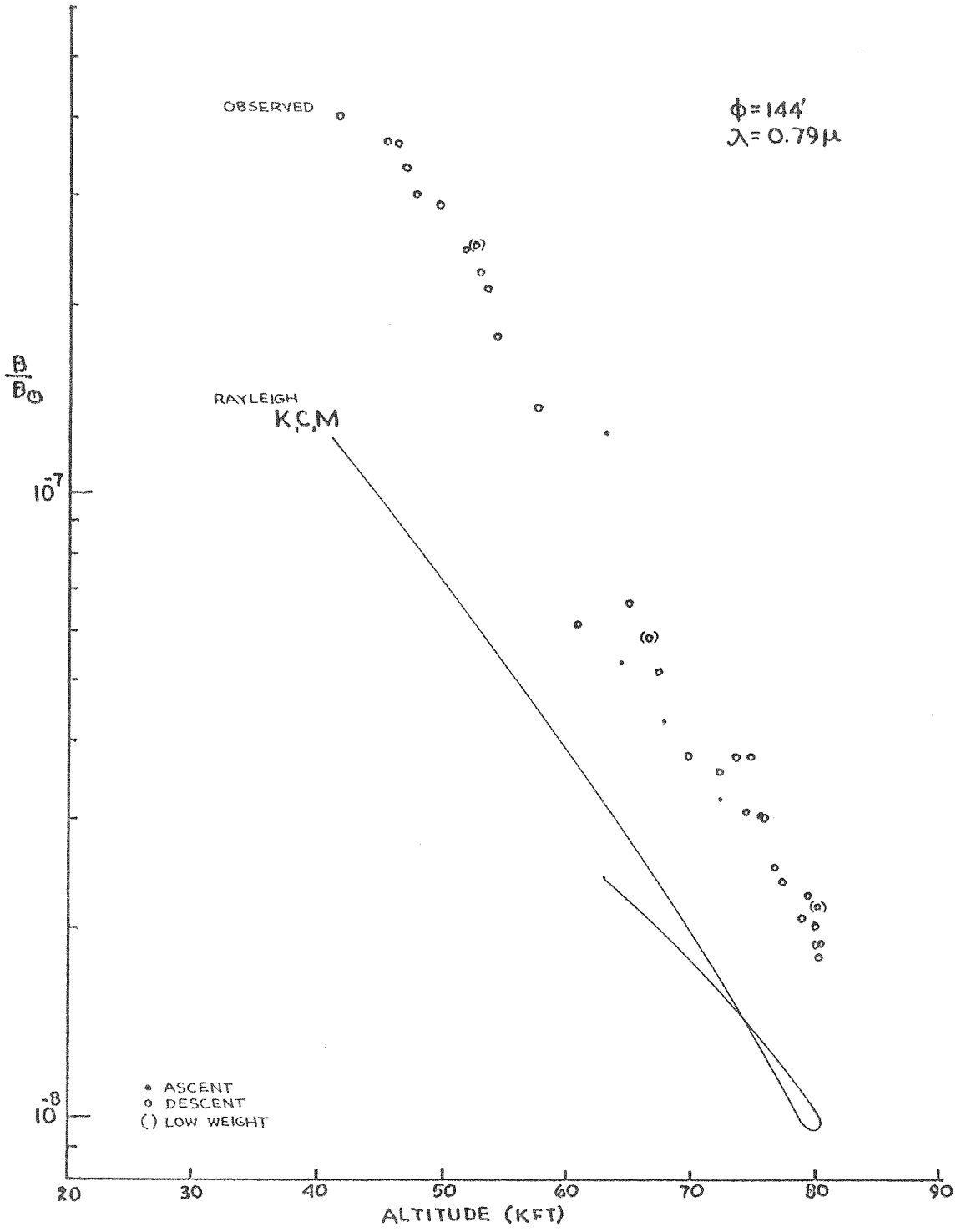

Figure 26

Observed and Rayleigh sky brightness for $\lambda = 0.79\mu$

C. The Residual Sky Brightness

For each observed point the residual sky brightness is defined as

$$B_{residual} = B_{observed} - B_{Rayleigh}. \tag{29}$$

The Rayleigh sky brightness that I have used in this definition is the Chandrasekhar solution obtained for the mean albedo, A_m, given by equations (27) and (28). Figures 27 through 35 show the residual sky data that were derived in this way for nine wavelength positions on the flight of 3 October 1960. The abscissa and ordinate scales are the same as for Figures 18 through 26. The residual brightness values have been multiplied by the factor $\mu_o = \cos Z_o$ to remove in the first approximation the zenith angle dependence. On each diagram is also shown a dashed curve indicating the level of 10% of the observed sky brightness. We see that the residual values are well above the observational uncertainty. All residual values exceed the maximum uncertainty of 33%. The residual points define mean curves that indicate the change in residual sky brightness with height at each wavelength region. The mean curves are shown as smooth lines through the residual data points. This step, of drawing an approximate curve through the residual points, marks the first smoothing of the observed data. I have taken points from the smoothed curves at eight fixed altitudes to plot the information in Figure 36. Shown there is the wavelength dependence of the residual sky, $\mu B/B_\odot$, for altitude intervals of 5 kft. The abscissa is wavelength in microns. The ordinate is a logarithmic scale of the residual sky, $B/B_\odot$.

In Figure 36 I have shown for reference the slopes taken by curves of $d\log B/d\lambda$ = 2 to 8. They are drawn to the same scale as the main diagram.

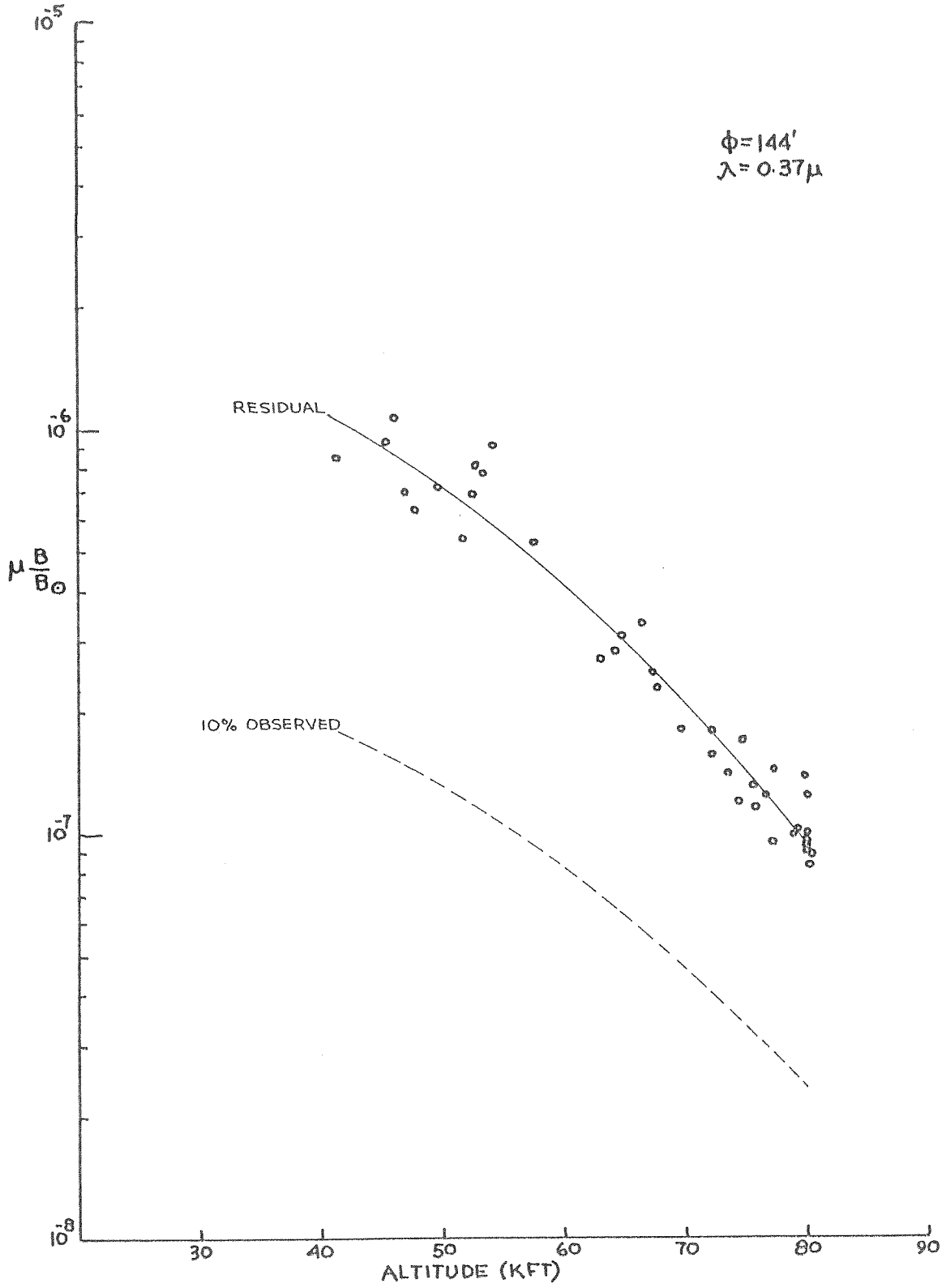

Figure 27

Residual sky brightness for $\lambda = 0.37\mu$

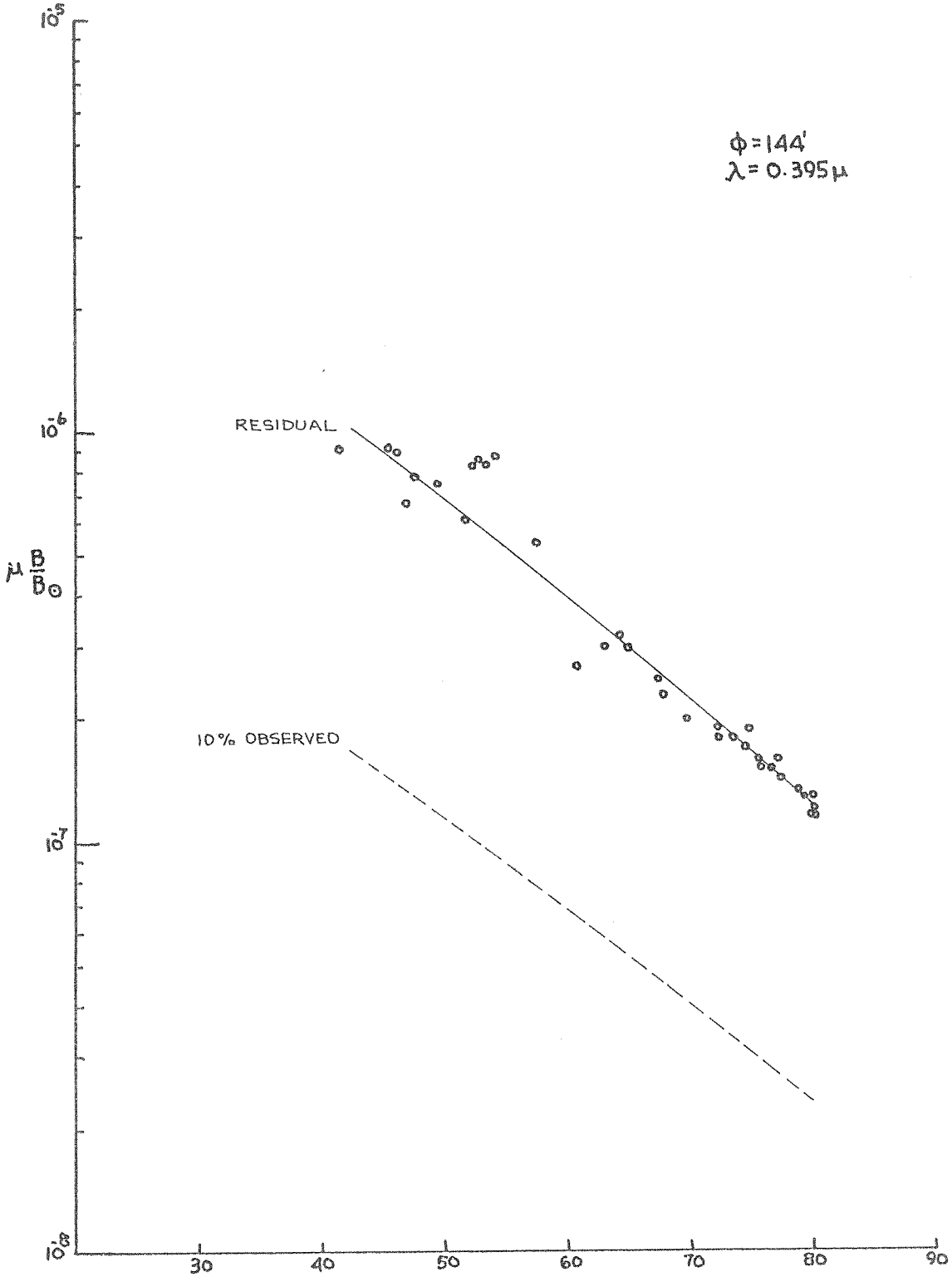

Figure 28

Residual sky brightness for $\lambda = 0.395\mu$

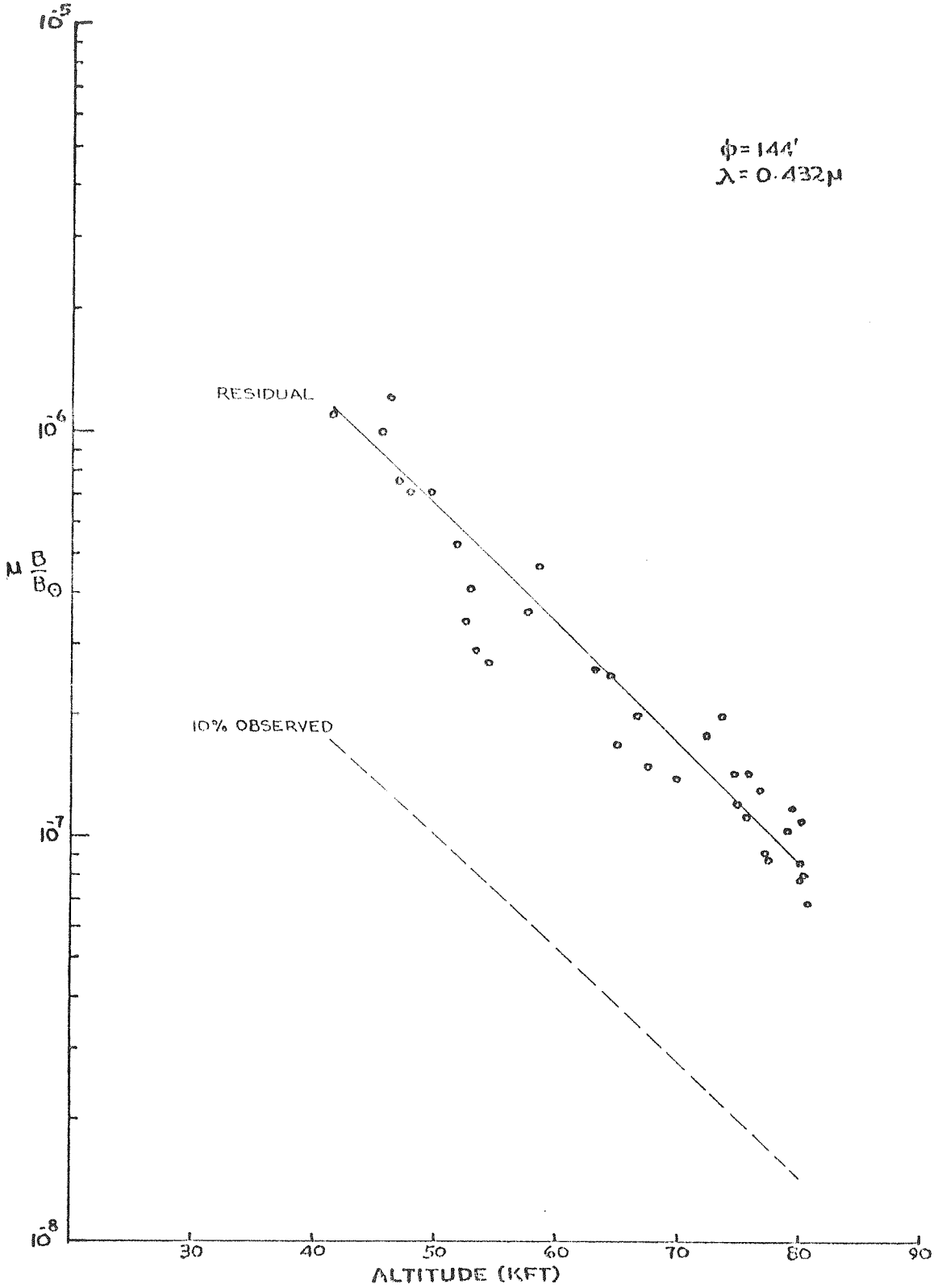

Figure 29

Residual sky brightness for $\lambda = 0.432\mu$

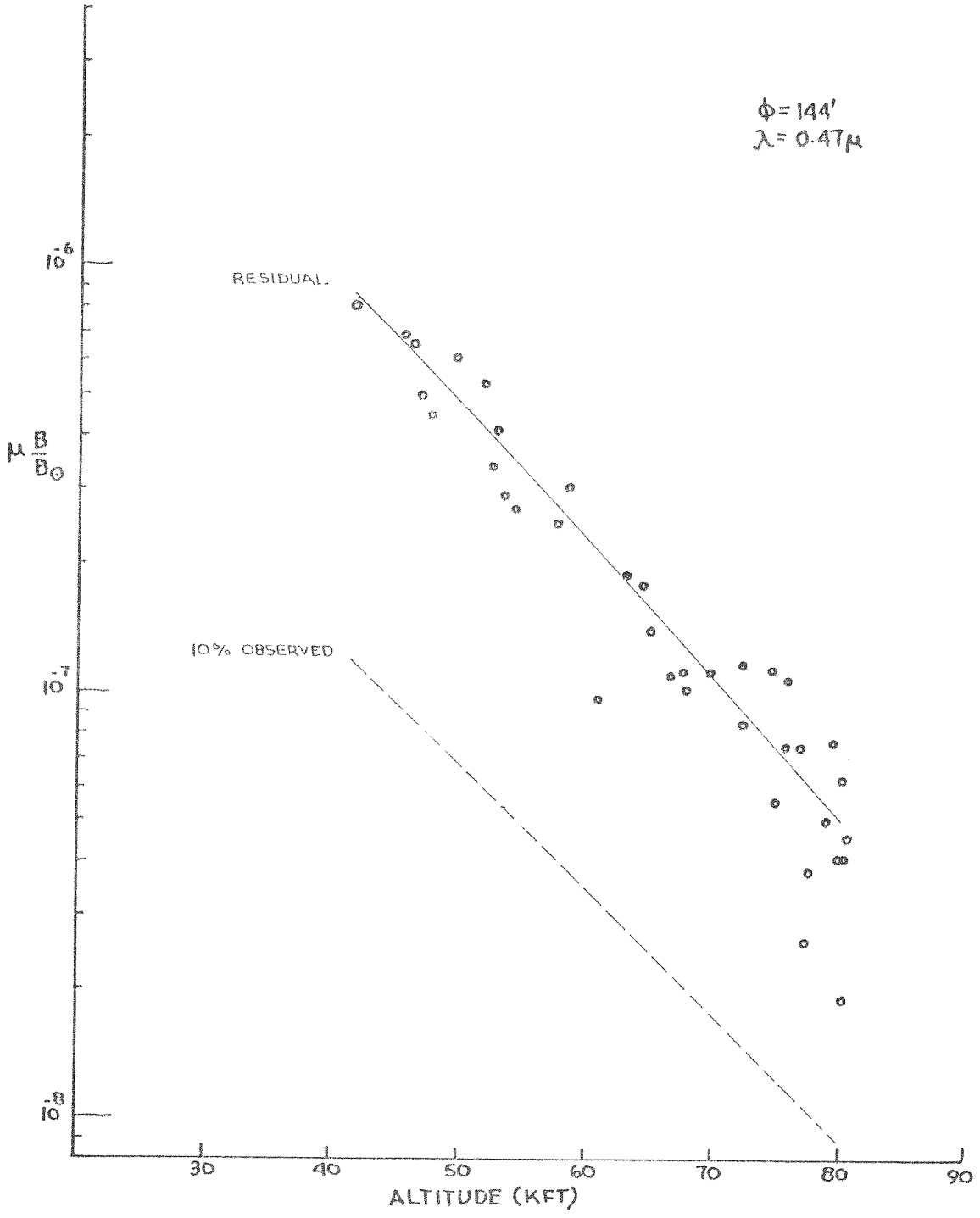

Figure 30

Residual sky brightness for $\lambda = 0.47\mu$

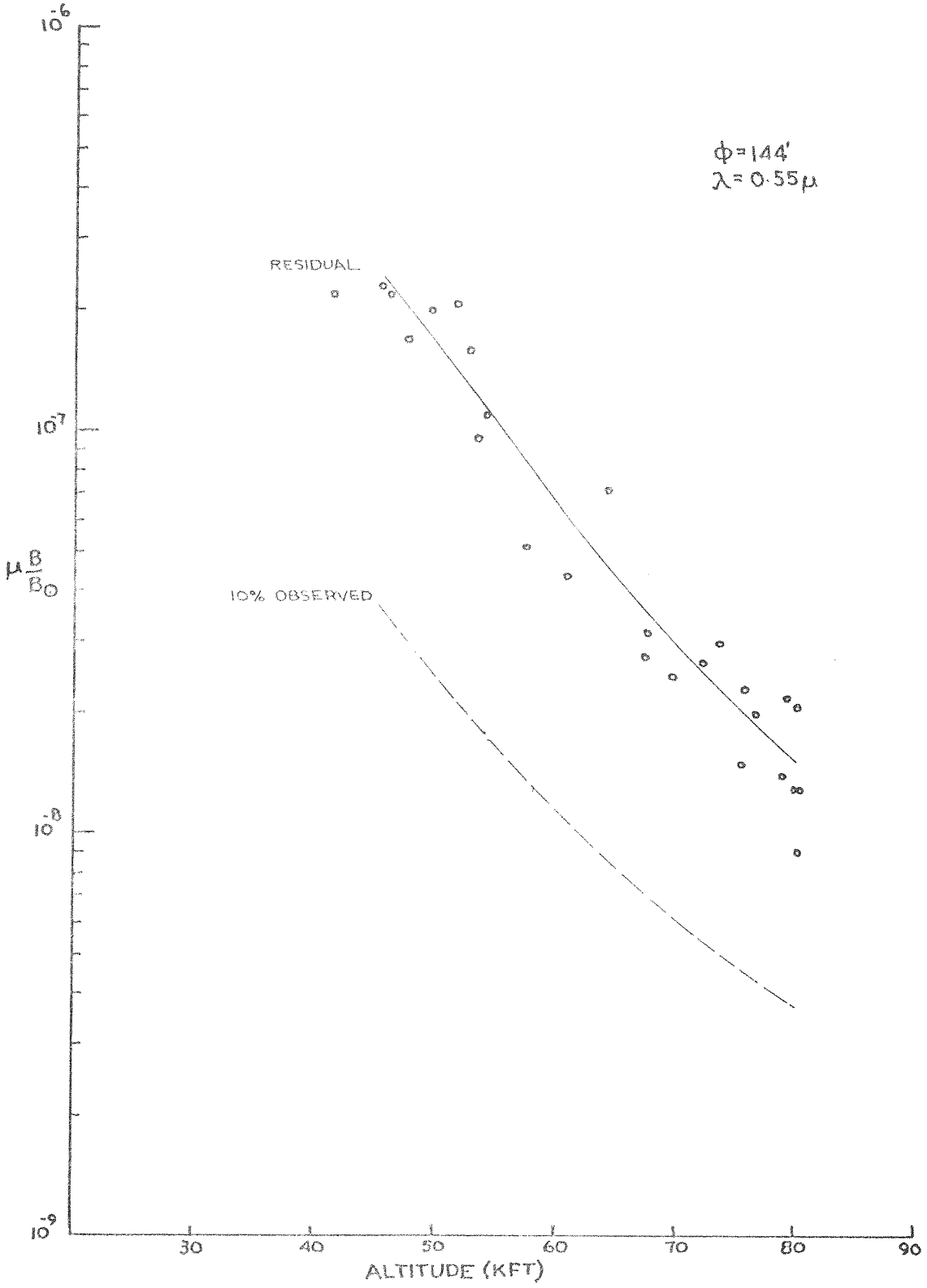

Figure 31

Residual sky brightness for $\lambda = 0.55\mu$

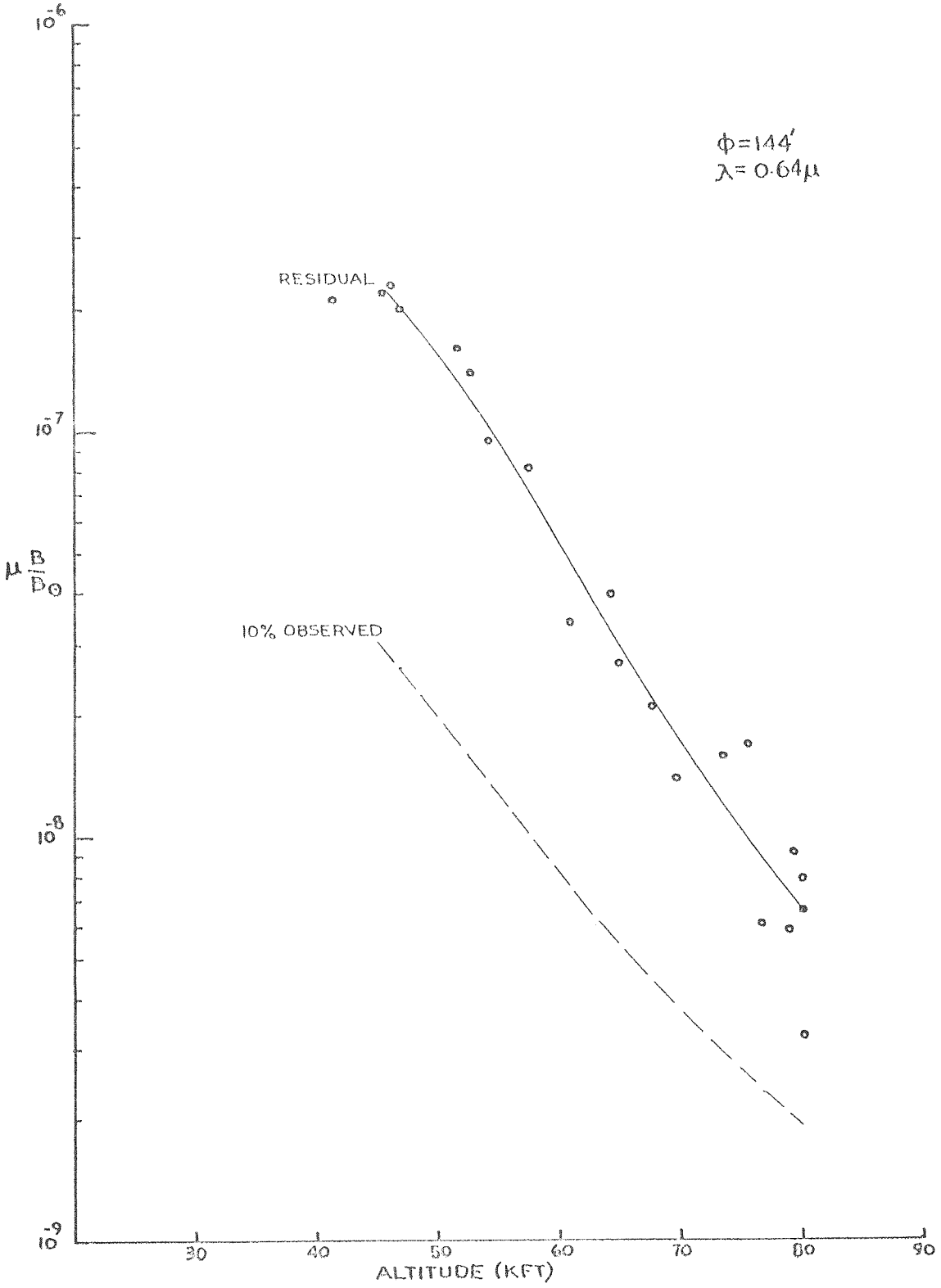

Figure 32

Residual sky brightness for $\lambda = 0.64\mu$

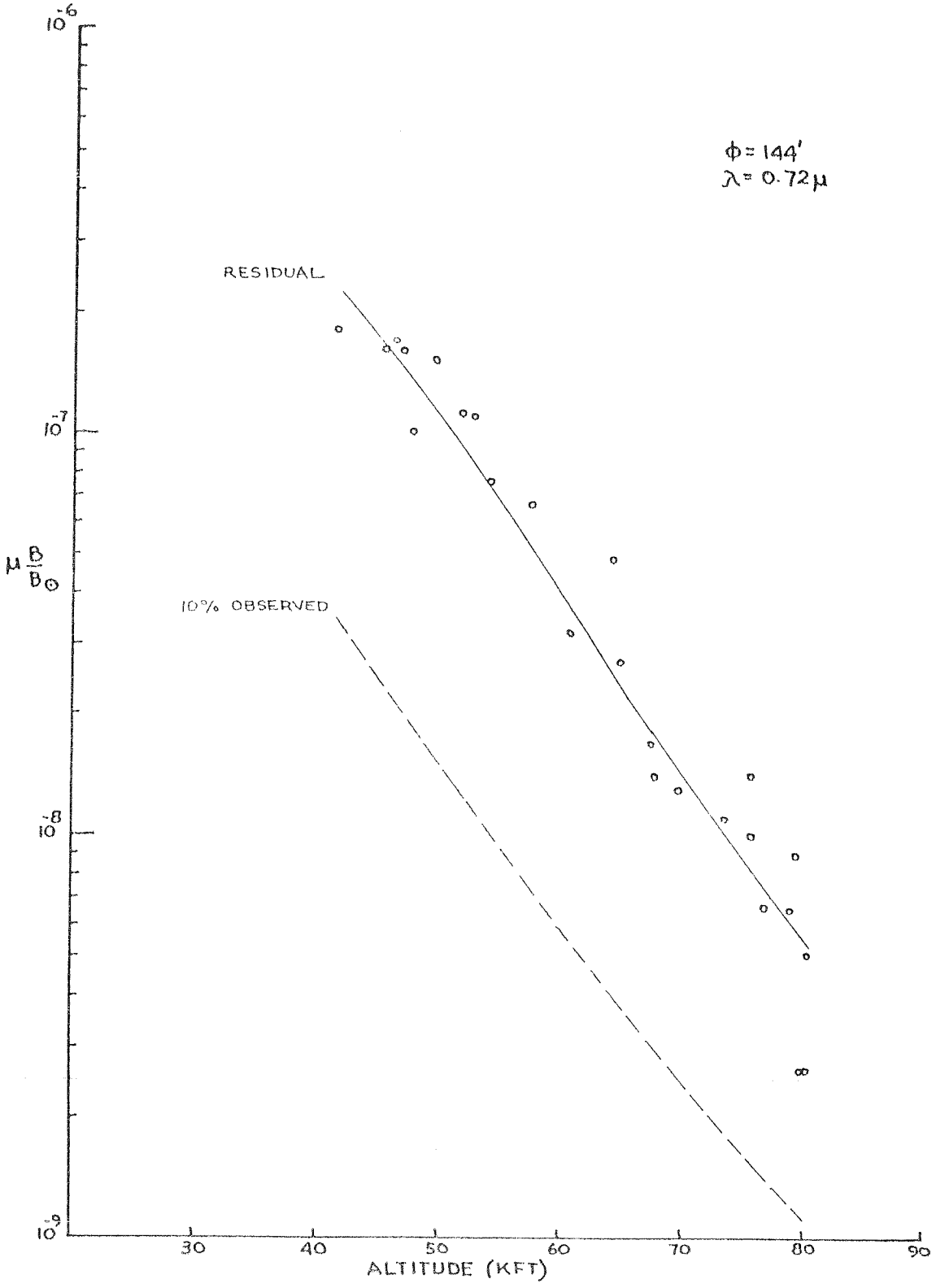

Figure 33

Residual sky brightness for $\lambda = 0.72\mu$

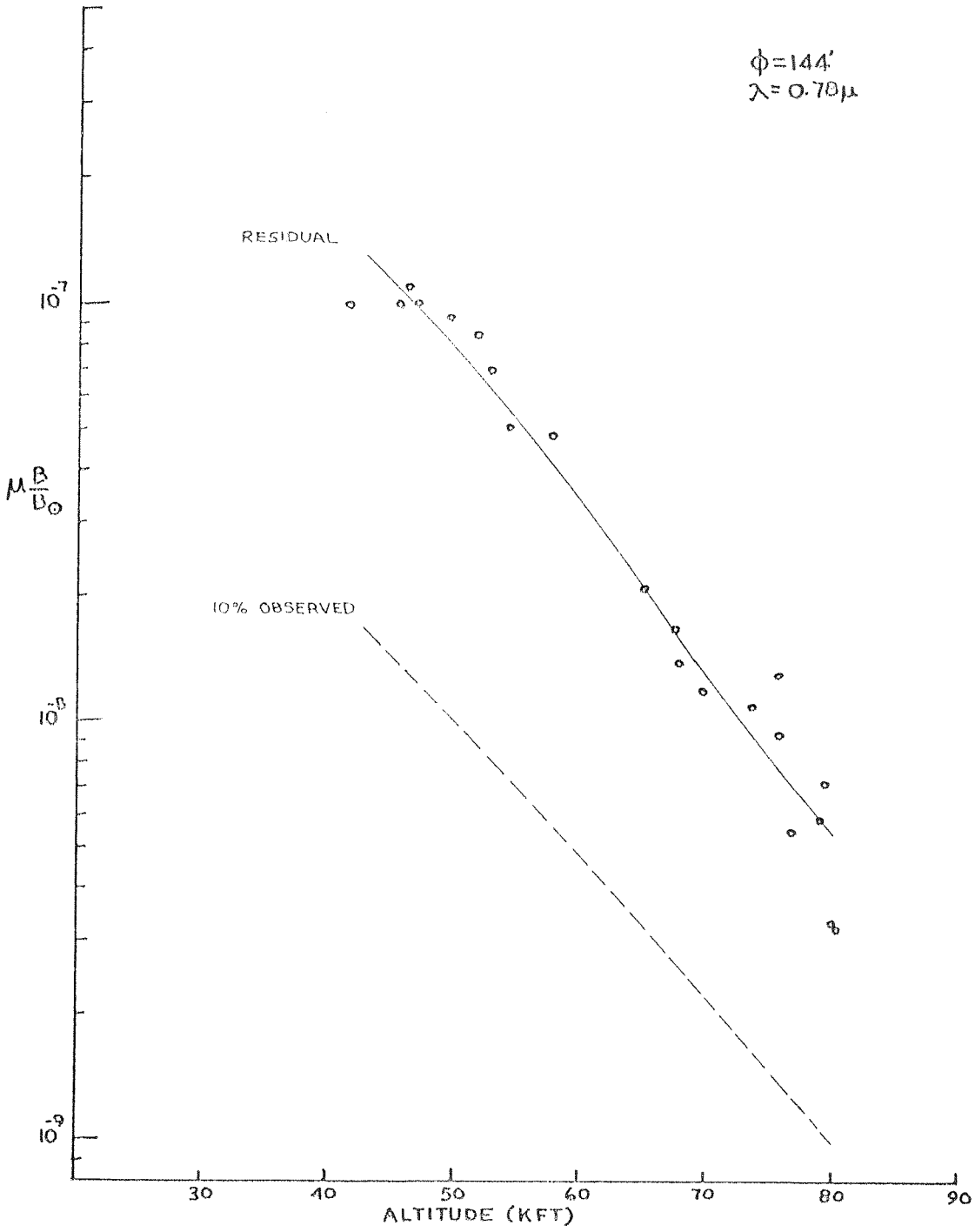

Figure 34

Residual sky brightness for $\lambda = 0.78\mu$

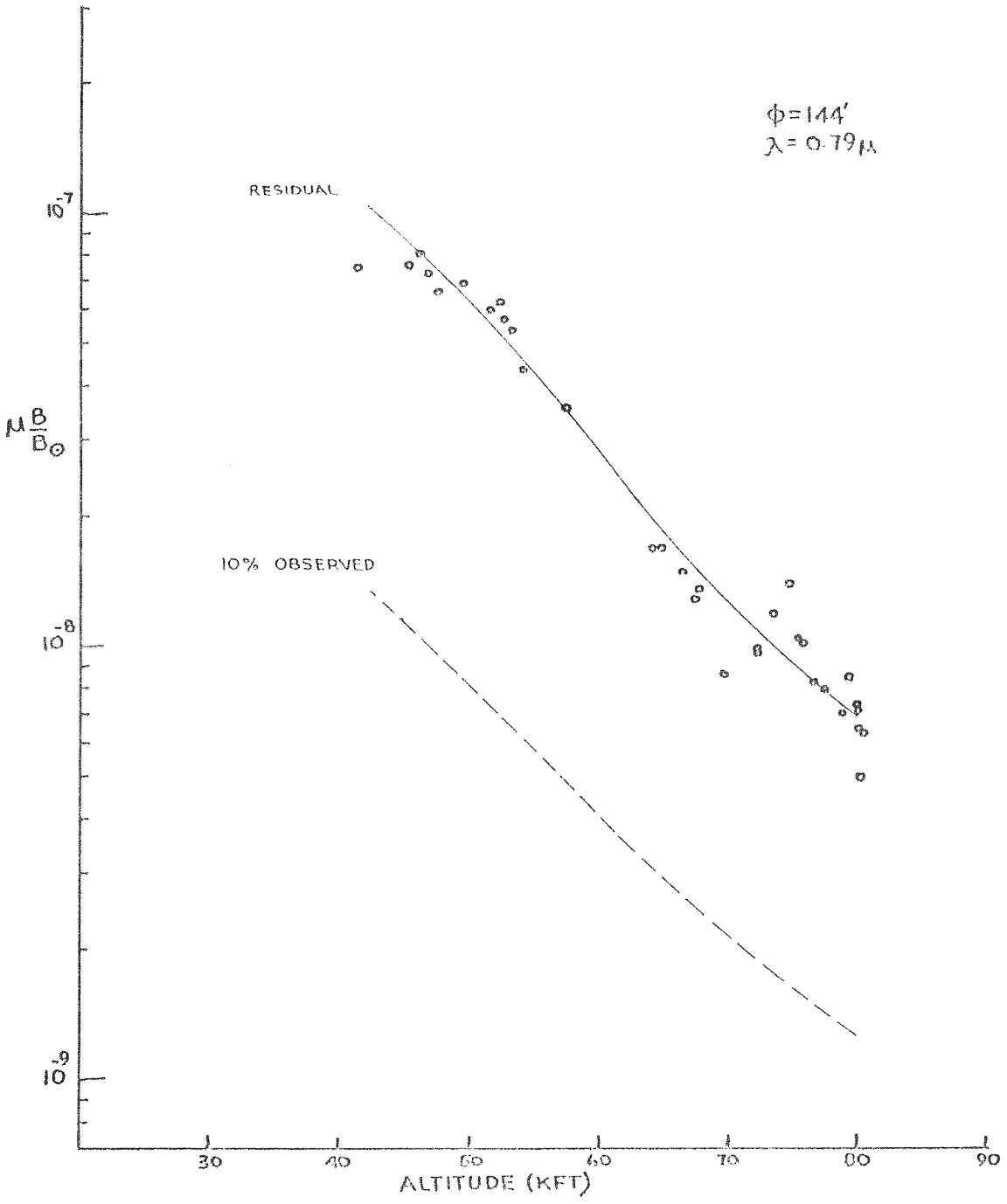

Figure 35

Residual sky brightness for $\lambda = 0.79\mu$

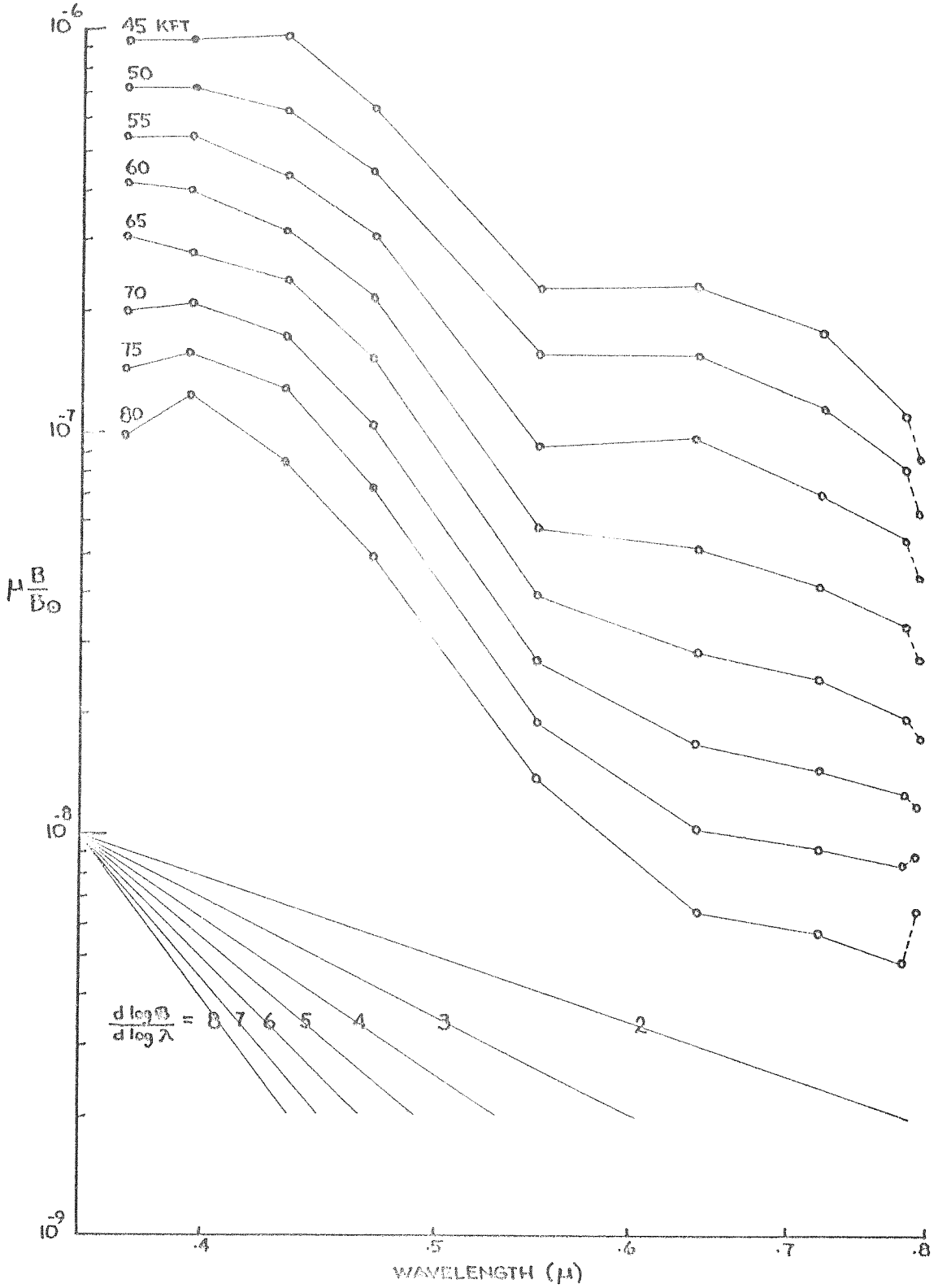

Figure 36

Residual sky brightness as a function of wavelength for selected altitudes

The curves shown in Figures 27 through 36 are reliable to $\pm$ 20%. Making allowance for this inexactitude, we can draw several conclusions from them:

1. For altitudes between 45 and 80 kft. the residual sky brightness decreases with altitude for all wavelengths, following an exponential law. From this we can say that there was no significant dayglow emission observed. A possible exception for $\lambda = .395\mu$ is discussed later.
2. The decrease with altitude is most marked for the long wavelength end of the visible spectrum. The same effect was noticed by Packer and Lock (1950) in their observations of the sky far from the sun. It results from the decrease in the population of larger Mie particles with height. Larger particles scatter more of the long wavelength radiation than do smaller particles. The scattered radiation at long wavelengths is a sensitive indicator of number of large particles present, as evidenced by the consistent decrease of the "red excess" with altitude in the curves of Figure 36.
3. The wavelength dependence of the residual brightness at each altitude follows the same general form as did the wavelength dependence of the observed sky brightness. If we allow for the limits of observational and theoretical uncertainty and smooth out the curves of Figure 36 to straight lines, we can represent the residual sky brightness data by the expression,

$$\frac{d \log \mathcal{B}}{d \lambda} = M(h) \qquad (29)$$

where $\mathcal{B} = \mu B/B_{\odot}$ and M is a function of height.

For h = 45 kft., M ≃ 3.4; for h > 65 kft., M≃4, which is the Rayleigh law exponent. It is not surprising that the wavelength dependence of the residual brightness above 65 kft. takes the form of the Rayleigh law; it indicates that the scattering particles above that altitude are mostly of Rayleigh size.

4. The inflection point at $\lambda = 0.55\mu$ in the lower altitude curves of Figure 36 may not be a real feature of the residual sky. At this wavelength the film sensitivity is at minimum (see Figure 7) and the instrument function that was used may not adequately compensate for it. Moreover, the film densities of the sky spectrum in this region were frequently near the background level. The behavior of the residual curves between 0.78μ and 0.79μ is also most likely an indication of observational error. The 0.79μ point was obtained from the record of the infrared filter; all other points were derived from the sky spectrograph. The spectrograph points are more reliable.

5. The consistent change of the shape of the residual curves between 0.37μ and 0.432μ in Figure 36 is of interest. We note that the residual sky brightness at 0.395μ relative to that at 0.37μ and 0.432μ increases uniformly with height above 65 kft. This feature is less than the limits of observational certainty and therefore may not be real. Nevertheless the uniformity of the trend and its coincidence with the head of the N_2^+ (0 - 0) emission band tempts one to attribute this increase to the dayglow. It could indicate the brightness threshold of N_2^+ emission; if so, it would indicate emission of about 10^{-8} $B_\odot$--- less than the value given by Miley et al (1953) but greater than the prediction of Chamberlain and Sagan (1960). The evidence, however, is weak

indeed. The other expected dayglow features show no indications of threshold levels.

D. Particle Size Distribution

I have assumed that the residual sky brightness at each altitude is the result of single Mie scattering by a size distribution of aerosols above that altitude. Let N'(a) be the number of particles of radius a that populate a column 1 cm^2 in cross section that extends from the observer to the top of the atmosphere. Then as was shown in Chapter II, the brightness at wavelength λ and scattering angle Θ that is produced by this distribution is

$$\mu \frac{B}{B_\odot}\lambda = \int_{a_{min}}^{a_{max}} \sigma_\lambda (a,m,\Theta)\, N'(a)da \qquad (30)$$

where σ_λ (a,m,Θ) is the Mie scattering cross section for a particle of radius a and index of refraction m at scattering angle Θ and wavelength λ. Given the scattering cross sections, the problem is to find the solution or solutions of Equation (30) in terms of size distributions N'(a) that satisfy the observed residual brightness data. A single distribution N'(a) must explain all the spectral observations at a given altitude; the problem is indeterminable for observations at a single wavelength and scattering angle. When data are available at several wavelengths the problem is soluble but the solutions are extremely sensitive to small changes in the observed data and to the accuracy of the numerical values of scattering cross sections that are used. There is no promise of a unique solution to the set of integral equations of the type (30). This same problem of determining a size distribution of aerosols to explain observed optical scattering data was studied for the case of ground observations by the

Armour Research Foundation (1956). They concluded that observational errors greater than about 1% could lead to non-existence of an exact solution, or to non-uniqueness of a solution, if one exists. Before finding the published Armour result I made numerous attempts at finding exact solutions using the NCAR IBM-1620 computer to perform the numerical integration and to solve the simultaneous equations. I found that the equations were invariably ill-conditioned and that changes in the sixth significant figure of the cross sections would produce marked changes in the solutions. The principal difficulty is in the extreme numerical range of the scattering cross sections used in the integrand and in the inaccuracy of the available cross sections. I found no physically realistic solutions by this method.

We can avoid the perplexities of an exact solution and also allow for non-unique solutions by solving the problem in reverse, namely, by guessing at a distribution N'(a) and solving Equation (30) for the resultant brightness as a function of wavelength. If enough solutions are tried, one can map out the effects of parameter changes in the size distributions and in this way isolate the area of possible solutions that fit the observations. If a family of non-unique solutions exists, their limits can be defined. The cut-and-try method is not an elegant one; with electronic computation it is even less sophisticated and might more appropriately be named the Method of Over-Kill. It was by this method that I obtained families of particle size distributions to fit the residual sky observations.

Distributions were studied for three values of the refractive index for which cross sections were available: $m = 1.20$ ($\approx$ ice), $m = 1.33$ (water), and $m = 1.50$ ($\approx$ glass). The integral in Equation (30) was evaluated for a minimum of 60 steps in the radius, a. In a preliminary study,

cross sections for $\Theta = 0°$ were used for the three refractive indices to determine the general variation of the solution with change in refractive index. Scattering cross sections for these calculations were obtained from the data published by Penndorf (1960). I then recalculated the $m = 1.33$ case for the scattering angle $\Theta = 2°.4$ using cross sections obtained by interpolation between values for $\Theta = 2°$ and $\Theta = 3°$, also obtained from Penndorf (1954a). The form of the particle distribution function that I used is based on that suggested by Junge (1955; Junge, Chagnon, and Manson, 1961). It is shown in Figure 37. All particles are presumed to have radii in the range $a_1 < a < a_3$. For $a_1 < a < a_2$ the size distribution is given by

$$\frac{dN(a)}{d\log a} = C_1 \qquad (31)$$

while for $a_2 < a < a_3$ it is given by

$$\frac{dN(a)}{d\log a} = C_2 a^{-\delta} \qquad (32)$$

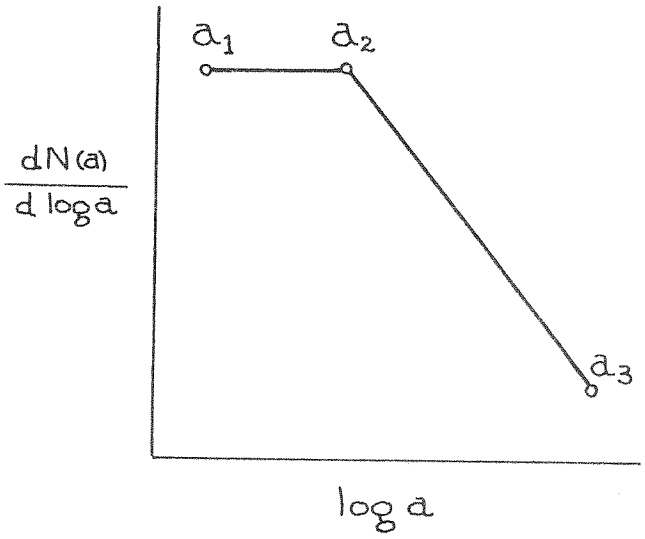

Figure 37
Particle size distribution

In Figure 37 the abscissa is the logarithm of the particle radius in microns; the ordinate is dN(a)/dloga, Junge's peculiar expression for particle concentration. Junge's concentrations N(a) are in units of particles per cm^3 while in our formulation the concentration N'(a) refers to the particles per cm^2 column. These quantities are related by

$$N'(a) = N(a)\, H' \qquad (33)$$

where H' is the scale height in cm of the particle atmosphere. It represents

the height that would include all the particles were the particle density constant at N(a). Since the scale height H' is itself a function of a it is not precisely true that $\frac{dN(a)}{d\log a} = \frac{dN'(a)}{d\log a}$. Since the formulae (31) and (32) were used only to define trial size distributions I used N'(a) and N(a) interchangeably in them. In later comparisons with numerical size distributions given by Junge I have used the properly defined N(a).

The expressions (31) and (32) can be considered to be ordinary first-order differential equations whose solutions are, respectively,

$$N(a) = C_1 M \ln a + C_3 \tag{34}$$

and

$$N(a) = C_2 M \frac{a^{-\delta}}{\delta} + C_4 \tag{35}$$

Here C_3 and C_4 are constants and $M = \log_{10} e$. The physically realistic case is that in which $C_4 = 0$; the constant C_3 is then determined by the requirement of continuity at $a = a_2$. The equations in this form were used in the numerical solutions of the integral in Equation (30).

I varied the parameters δ, a_2, and a_3 and computed 534 different solutions of Equation (30), each for six wavelength positions between $\lambda = 0.395$ and $\lambda = 0.85\mu$. The calculations were performed on the IBM-1620 computer. A constant value of $a_1 = 0.02\mu$ was used for the minimum particle size; the other parameters were varied systematically over the ranges given below:

δ : 0.0 to 30.0

a_2 : 0.02 to 1.0μ

a_3 : 0.7 to 10.0μ

The solutions, representing values of $\mu\frac{B}{B}\lambda \equiv \mathcal{B}_\lambda$ were catalogued

according to the resulting value of the derivative

$$\frac{\Delta \log \mathcal{B}}{\Delta \log \lambda}$$

between $\lambda = 0.395$ and $\lambda = 0.85\mu$.

It was soon apparent that the solutions were relatively insensitive to change in the parameter a_3, the upper limit of particle size. For $\delta < 5$, a change in a_3 from 1 to 10μ results in a slight decrease in $\Delta \log \mathcal{B}/\Delta \log \lambda$. For all other values of δ the derivative is unaffected by change in a_3.

In Figure 38 I have shown the map of solutions obtained for $m = 1.33$, $\Theta = 2\overset{\circ}{.}4$, and $a_3 = 1$. The abscissa is the value of a_2 in microns. The ordinate is the index δ. The contour lines designate the regions of a_2 and δ for which the derivative $\Delta \log \mathcal{B}/\Delta \log \lambda$ equals the value given. The points from which the diagram was constructed were obtained by solving Equation (30) for $\mu \frac{B}{B} \lambda \equiv \mathcal{B}_\lambda$ at different wavelengths for a given choice of δ and a_2. Thus for a size distribution characterized by $a_2 = .1$ and $\delta = 5$, the value of $\Delta \log \mathcal{B}/\Delta \log \lambda$ is 2.5. The region in the upper left corner represents the upper limit of $\Delta \log \mathcal{B}/\Delta \log \lambda$; its value is about 4, corresponding to the Rayleigh limit. The region at the bottom and in the bottom right corner indicates a lower limit to the derivative of about 1. However, here the definition of the derivative is of reduced meaning since the brightness versus λ curve that is obtained for values in this area is not a simple curve but shows wiggles due to the increased influence of large particles. It is in the lower region that the effects of change in a_3 are noticed. However, the region of interest in the residual sky interpretation is that in the upper left.

Diagrams similar to Figure 38 were constructed for $\Theta = 0$ and $m = 1.20$, 1.33, and 1.50. The $\Theta = 0$, $m = 1.33$ diagram is the same as Figure 38. The

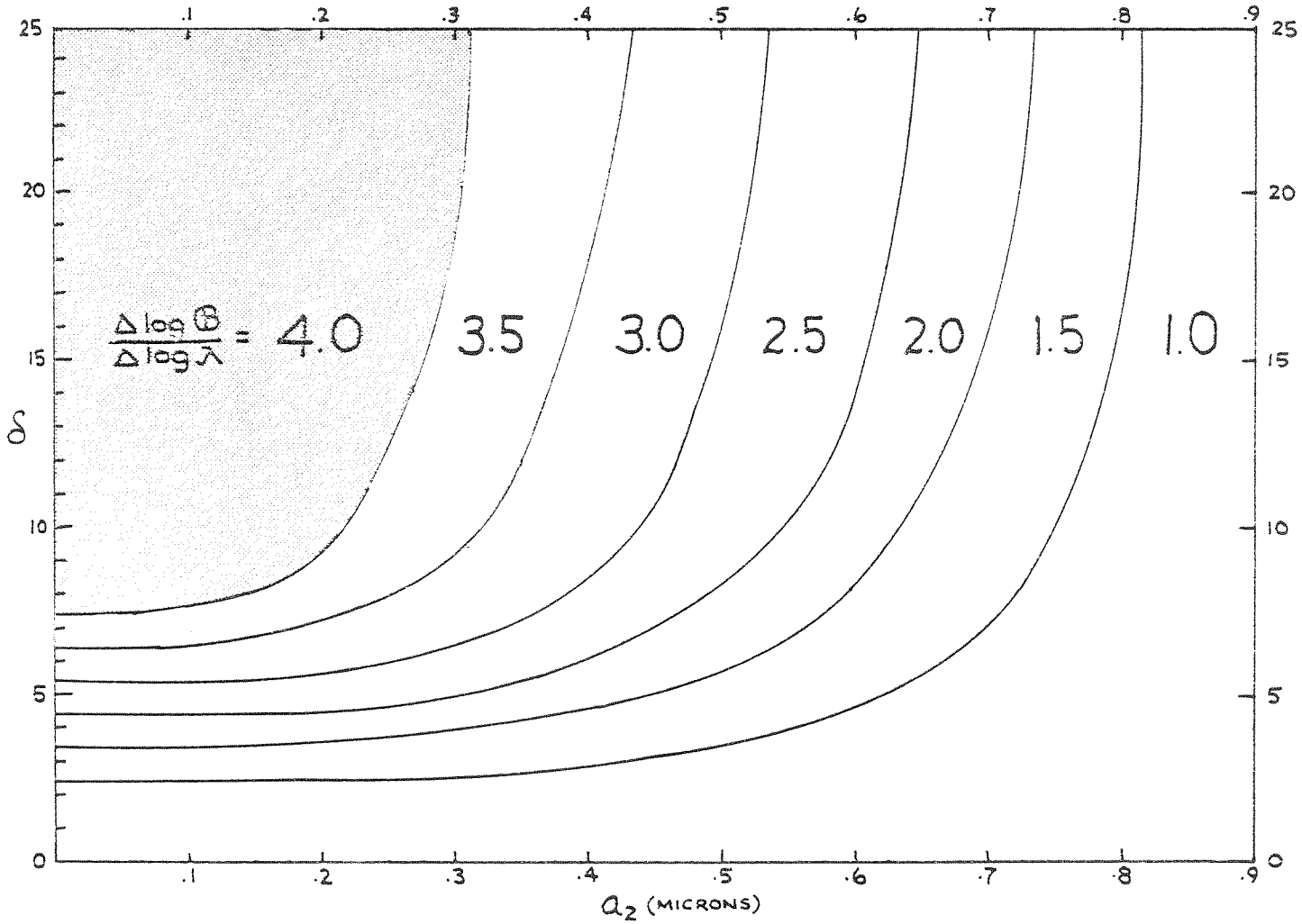

Figure 38

Map of $\Delta\log\mathcal{B}/\Delta\log\lambda$ solutions for various particle size distributions. m = 1.33, θ = 2°.4, a_3 = 1.0μ.

diagram for m = 1.20 shows the same solution contours shifted to the right; for example, the region of solution for which $\Delta \log \mathcal{B} / \Delta \log \lambda = 4$ represents a larger area for m = 1.20 than for m = 1.33. The diagram for m = 1.50 shows a shift to the left, such that the area for which $\Delta \log \mathcal{B} / \Delta \log \lambda = 4$ is more compressed than for m = 1.33. This can be interpreted as indicating an increase in scattering efficiency with refractive index for very small particles --- a result also shown by Volz (1954), van de Hulst (1957), and Penndorf (1960). Varying the refractive index produced no change in the region of the curve that lies to the left of $a_2 = 0.2\mu$. The general appearance of all the solution maps was essentially the same.

In Section C of this chapter we saw that the overall slope of the residual sky brightness curve took the form

$\Delta \log \mathcal{B} / \Delta \log \lambda \cong 3.4$ for observations at 45 kft.,

and $\Delta \log \mathcal{B} / \Delta \log \lambda \cong 4$ for observations between 65 and 80 kft.

We can now interpret each result in terms of a family of possible particle distributions, making reference to Figure 38. The observations above 65 kft. can be explained by any size distribution of Mie particles whose parameters δ and a_2 lie in the "4" (dark-shaded) region of the figure. The observations at 45 kft. can be explained by any of the distributions in the "3.5" (light-shaded) region.

The simplest model in each region or family of solutions is that for which $a_1 = a_2$, in which case the size distribution curve shown in Figure 37 takes the form of a single straight line. If we take this case, the residual sky observations are explained by the size distributions outlined in Table 8.

Table 8

h	Distribution	δ	a_1	a_2	a_3	m
45	A	7	.02μ	.02μ	1-10μ	1.20, 1.33, 1.50
65	B	8	.02μ	.02μ	1-10μ	1.20, 1.33, 1.50
80	C	8	.02μ	.02μ	1-10μ	1.20, 1.33, 1.50

I have listed the value a_3 = 1-10μ since the choice of a_3 makes no difference in the resulting brightness in this range; particles larger than 1μ make a negligible contribution. I have also listed the three possible values of m, since the same solution was given for all three values of m in this region. In Figure 39 I have plotted the actual distributions A, B, and C for the m = 1.33 case. The abscissa is a scale of the particle radius in microns; the ordinate is the log of the particle column density N'(a). The slopes of distributions B and C (65 and 80 kft.) are the same, indicating that the form of the size distribution is constant in this range. For a given particle radius the distance between any two of the curves in Figure 39 represents the population of particles of that radius in a 1 cm^2 column of height $\triangle$ h between the altitudes of the bounding curves. Thus the distance between the curves B and C represents the particle population $\triangle N'(a)$ in a cm^2 column between 65 and 80 kft., where

$$\triangle N'(a) = N'_{h_1}(a) - N'_{h_2}(a) \tag{36}$$

The mean particle density in particles per cm^3, N(a) over the height range $\triangle$ h is given by

$$N(a) = \frac{\triangle N'(a)}{\triangle h} \quad . \tag{37}$$

Values of the populations N(a) so obtained and of the column populations N'(a), are given in Table 9. The first column is particle radius in

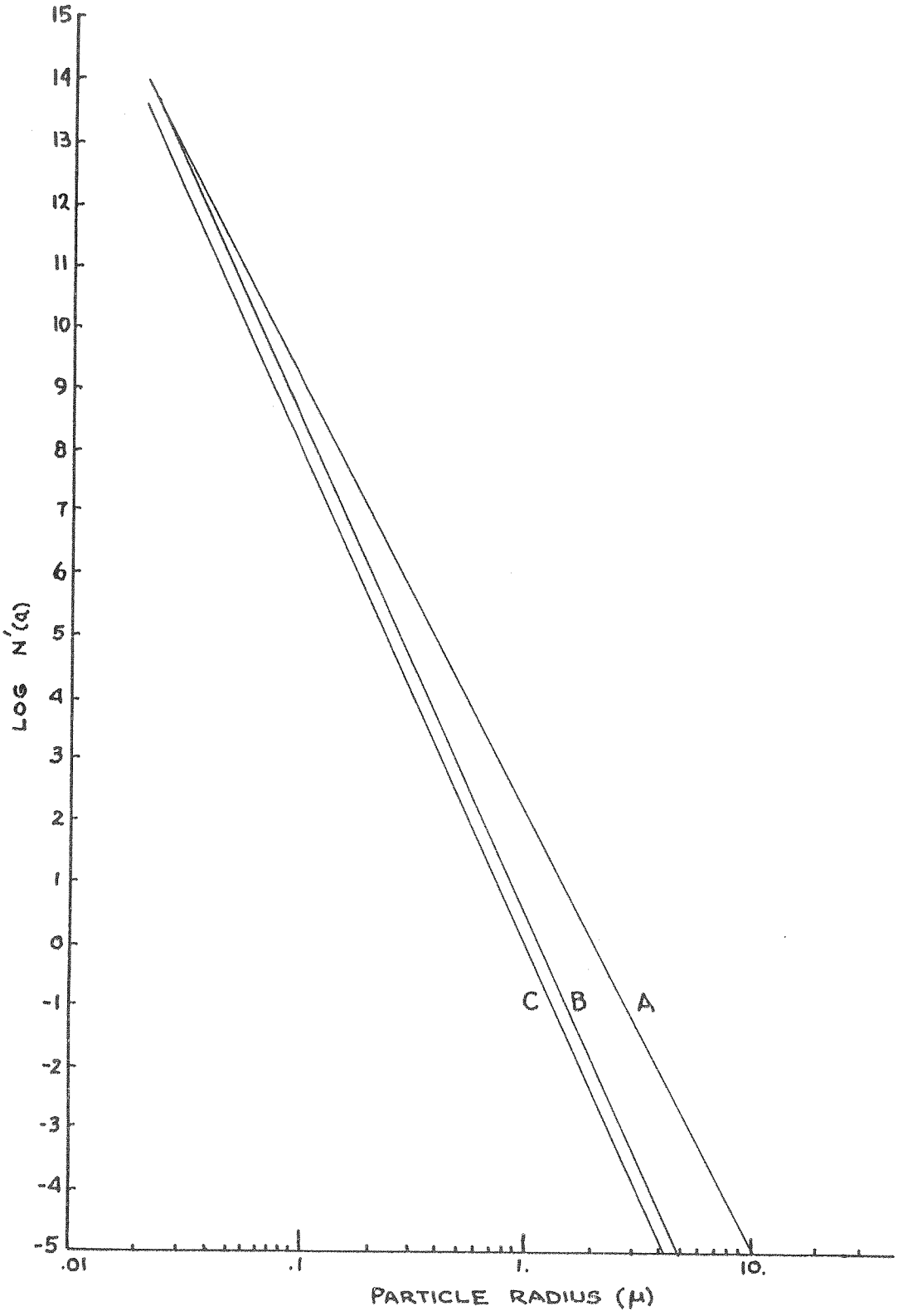

Figure 39

Three particle size distributions that fit the Coronascope data

Table 9. Particle number densities derived from Coronascope spectral data.

Particle radius a	Column Density (cm^{-2}) $N'_A(a)$ (45 kft.)	$N'_B(a)$ (65 kft.)	$N'_C(a)$ (80 kft.)	Volume Density (cm^{-3}) N(a) (45-65)	N(a) (65-80)
.02μ	9.5×10^{13}	1.1×10^{14}	4.1×10^{13}	-3.2×10^{7}	1.5×10^{8}
.03	5.6×10^{12}	4.3×10^{12}	1.6×10^{12}	2.0×10^{6}	5.9×10^{6}
.04	7.4×10^{11}	4.3×10^{11}	1.6×10^{11}	5.1×10^{5}	5.9×10^{5}
.05	1.6×10^{11}	7.2×10^{10}	2.7×10^{10}	1.4×10^{5}	1.0×10^{5}
.06	4.3×10^{10}	1.7×10^{10}	6.2×10^{9}	4.4×10^{4}	2.3×10^{4}
.07	1.5×10^{10}	4.9×10^{9}	1.8×10^{9}	1.6×10^{4}	6.8×10^{3}
.08	5.8×10^{9}	1.7×10^{9}	6.2×10^{8}	6.8×10^{3}	2.3×10^{3}
.09	2.5×10^{9}	6.6×10^{8}	2.4×10^{8}	3.1×10^{3}	9.1×10^{2}
.1	1.2×10^{9}	2.8×10^{8}	1.0×10^{8}	1.5×10^{3}	3.9×10^{2}
.2	9.5×10^{6}	1.1×10^{6}	4.1×10^{5}	1.4×10^{1}	1.5×10^{0}
.3	5.6×10^{5}	4.3×10^{4}	1.6×10^{4}	8.4×10^{-1}	6.0×10^{-2}
.4	7.4×10^{4}	4.3×10^{3}	1.6×10^{3}	1.2×10^{-1}	6.0×10^{-3}
.5	1.6×10^{4}	7.2×10^{2}	2.7×10^{2}	2.4×10^{-2}	1.0×10^{-3}
.6	4.3×10^{3}	1.7×10^{2}	6.2×10^{1}	6.9×10^{-3}	2.3×10^{-4}
.7	1.5×10^{3}	4.9×10^{1}	1.8×10^{1}	2.4×10^{-3}	6.8×10^{-5}
.8	5.8×10^{2}	1.7×10^{1}	6.2×10^{0}	9.2×10^{-4}	2.3×10^{-5}
.9	2.5×10^{2}	6.6×10^{0}	2.4×10^{0}	4.1×10^{-4}	9.1×10^{-6}
1.0	1.2×10^{2}	2.8×10^{0}	1.0×10^{0}	2.0×10^{-4}	3.9×10^{-6}

microns. Columns 2, 3, and 4 give the column densities N'(a) for the three size distributions A, B, and C that fit the residual sky data. The last two columns give the mean particle densities N(a) (per cm^3) for the altitude regions between 45 and 65 kft. and between 65 and 80 kft. respectively. The negative density in column 5 for a = 0.2 is of no physical meaning; it appears in Figure 39 as the overlap of curves A and B at the upper left. Though the value of the difference is about 10^7, it represents the difference between two numbers whose orders of magnitude are 10^{14}.

We should bear in mind that the size distributions A, B, and C used in this analysis were non-unique results of the observed data. The zones of solutions given in Figure 38 afford a wide variety of possible interpretations. We should also remember that the column densities N'(a) derived from the Coronascope data are more accurate than the volume densities N(a). The column densities are as accurate as the residual sky observations, which were shown earlier to be accurate to about $\pm$ 20%.

E. Comparison with Other Data

1. Aerosol sampling measurements

The most extensive data relating to the composition and distribution of stratospheric aerosols are those of Junge (1955, 1961; Junge, Chagnon, and Manson, 1961); there are little other data available. Junge's data were obtained by atmospheric sampling techniques; he has made many measurements in the stratosphere using particle impactors and Aitken nuclei counters carried aloft by balloons and aircraft. Fortunately his observations cover the approximate latitude, time, and altitude of the Coronascope flights and thus are of especial interest for comparison. In a recent paper Junge and Manson (1961) give particle size distributions

derived from impactor collections made in a series of U-2 (aircraft) flights in the spring of 1960. In Figure 40 I have shown the distributions that were obtained from five flights at about 20 km. (65.6 kft.) altitude. The abscissa is a logarithmic scale of particle radius in microns; the ordinate, also on a logarithmic scale, is the quantity dN/dloga per cm^3. The shaded area labeled "Balloon Impactors" marks the limits given by Junge and Manson to include all data from their balloon sampling flights in 1958 and 1959 for altitudes of 20 to 30 km. Their estimates from nuclei counters for the small particle range $.01 < a < .1\mu$ are shown as a second shaded area; however, Junge states that at stratospheric altitudes the limitations of the counter restrict such data to an approximation (Junge, 1961). The line marked "HAO-1" gives a size distribution obtained from the residual sky brightness data reported here; it was derived from column 6 of Table 9 and gives mean particle densities dN/dloga for the region 65-80 kft. based on distributions B and C. I have shown the distributions resulting from two other choices of allowed solutions as "HAO-2" and "HAO-3". The "HAO-2" curve is representative of an allowed compound distribution curve with a knee at the small particle end; it was calculated for $a_2 = 0.1\mu$ and $\delta = 10$. The curve "HAO-3" shows the extreme limit of the allowed solutions for which $a_2 = 0.3\mu$ and $\delta \rightarrow \infty$, corresponding to a size distribution in which there are no particles of radius larger than 0.3μ. All allowed solutions of the optical data lie between the general limits of the "HAO-1" and "HAO-3" curves.

Because of the ambiguity in the interpretation of the Coronascope data it is difficult to make a definitive comparison with the sampling data. However, the following general conclusions can be drawn:

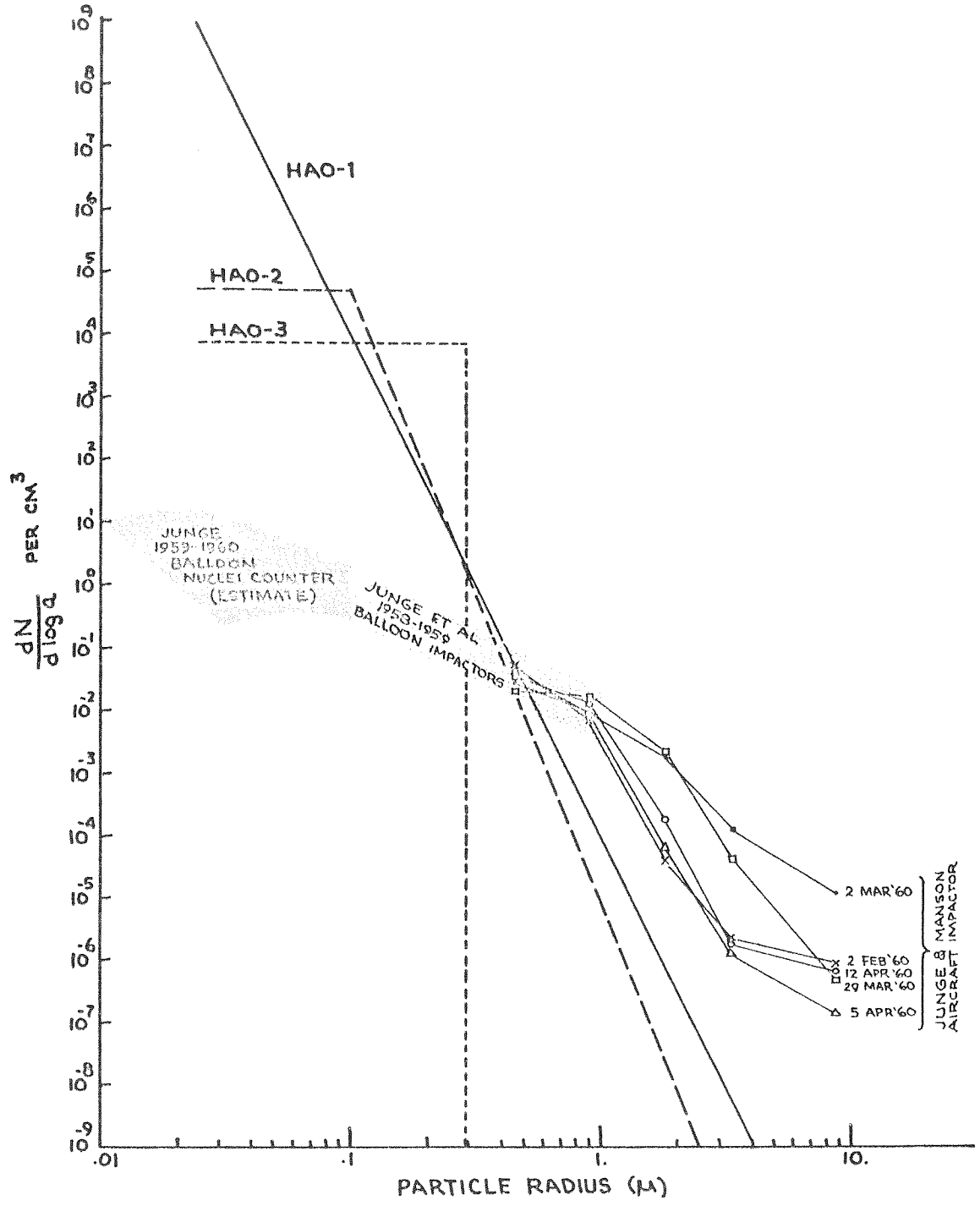

Figure 40

Comparison of particle size distributions obtained by optical and sampling techniques

1. If we take the less extreme (smaller δ) solutions there is general agreement with the 1960 sampling observations as to the slope of the main branch ($a > .5$) of the size distribution curve. This agreement is best for the "HAO-1" model and the April 1960 data of Junge and Manson. Both indicate a stratospheric size distribution characterized by $\delta = 7$ or 8. This higher δ contradicts the value $\delta = 3\text{-}4$ given by Junge for his earlier observations (1955; Junge, Chagnon, and Manson, 1961) and which is indiscriminately adopted for all altitudes in the literature (Volz and Goody, 1960; Curcio, 1961; Penndorf, 1954b). While the result $\delta = 3\text{-}4$ seems established for the lower troposphere the present indication is that a higher δ applies to the stratospheric population. This possibility was recently mentioned by Volz and Bullrich to account for anomalous infrared sky measurements made at Mainz (1961).
2. In the size range between 0.3 and 1.0μ there is coarse agreement in the particle populations but definite disagreement on the slope of the distribution curve. The sampling data indicate a change in slope of the curve in this region; the optical observations do not require it.
3. There is a fundamental disagreement on the particle populations of particles smaller than about 0.3μ. The optical observations do not show the small-particle cutoff that has been a consistent feature in the sampling measurements. Rather, a continued increase is suggested.

It is conceivable that the reason for variance between the two sets of data is a seasonal variation in the stratospheric aerosol content. However, the long residence times of particles of radius less than 0.1μ

($\tau \sim 1$ year) imply that the populations of these small particles should be a reasonably constant feature of the stratosphere. The only known injection of nuclear debris during the year was the French test in February, 1960.

It is more reasonable to attribute the disagreement to errors in one or both of the methods. The optical method depends upon a theoretical estimation of the Rayleigh brightness and does not give a unique solution for the particle size distribution. The sampling method relies on aerodynamic correction factors and large extrapolations, since only a small volume of air is sampled by the impactors or nuclei counters. A proper question is, which method is more accurate? If we consider the size range in which there is the most serious disagreement ($a < 0.3\mu$), the answer seems clearly in favor of the optical data. The impactors used by Junge, Chagnon, and Manson drop in collection efficiency from 80% at 0.2μ radius to 10% at 0.12μ radius, and are insensitive to particles of radius less than 0.1μ (Junge, Chagnon, and Manson, 1961). Nuclei counters, though capable of counting particles in the range 0.1 to 0.01μ radius, are of limited use in the stratosphere. Scattering measurements, on the other hand, are uniformly sensitive to particles of several microns in radius down to the Rayleigh limit of about 0.03μ and do not favor a particular size of aerosol as does the sampling technique. For sub-micron aerosols and for low particle concentrations the optical method of determining size distributions is potentially the more reliable technique.

2. Meteoric influx estimates

It is also interesting to interpret the particle size distributions in relation to meteoric influx rates. This interpretation can represent only an upper limit, however, since there is no evidence in the optical

data to indicate the source of the particles. Perhaps none of them is meteoric. Junge, Chagnon, and Manson (1961) have made the premise that the stratospheric aerosols of radius 0.1 to 1.0μ are formed by chemical reaction in the stratosphere, and that particles with radii less than 0.1μ are of tropospheric origin. Their theory is based in part on the small numbers of the sub-micron particles detected in sampling, however, and the optical data do not confirm this observation. Svestka (1954) has made a study of meteoric dust in the atmosphere based on lunar eclipse observations, earth shadow observations, and atmospheric transparency data, and has concluded that meteoric dust is probably formed by particles of radius 0.1 to 0.01μ.

Under the assumption that all stratospheric particles are meteoric, the rate of influx F'(a) is related to the column population N'(a) and to the time of residence in the column, T(a) by the relation,

$$F'(a) = \frac{N'(a)}{T(a)} \tag{38}$$

The residence time is determined by a combined effect of many processes, among which are

(1) gravitational settling as described by Stokes' law,

(2) vertical and horizontal diffusion,

(3) coagulation of small particles to form larger ones,

(4) various vertical and horizontal mixing processes that result from the general atmospheric circulation.

In my approximation I have considered only gravitational settling with an estimated correction for particle coagulation.

Link (1950) has computed times of fall for meteoric particles of different radii, using fall velocities determined by Stokes' law with the Millikan correction for discontinuity in the resisting medium. The curves

in Figure 41 were derived from his calculations; they give the times of fall for meteoric particles to reach an altitude of 80 kft. (24.5 km.). The abscissa is the particle radius in microns, given on a logarithmic scale; the ordinate is the fall time in seconds, also on a logarithmic scale. Values given are for particle densities of 1 gram/cm^3 (water), 3.3 grams/cm^3 (stone) and 8 grams/cm^3 (iron). The effect of coagulation is to decrease the fall times, or equivalently, to decrease the particle population above a certain altitude. This rate of decrease by coagulation can be expressed as

$$\frac{\partial N'(a)}{\partial t} = -KN'^2(a) \tag{39}$$

where K is the coagulation coefficient, a function of atmospheric conditions and of a^{-1}. (Junge, Chagnon, Manson, 1961). For particles of meteoric origin we can replace N'(a) by $F'(a)T(a)$ as a first approximation, in which case the coagulation rate is

$$\frac{\partial N'(a)}{\partial t} \simeq -KF'^2(a)T^2(a) \tag{40}$$

That is, for equal influx rates, the coagulation rate is proportional to the square of the residence time. The effect of coagulation would be to depress the curves of Figure 41 at the small particle end where residence times are high. Junge, Chagnon, and Manson have shown that coagulation assumes importance for stratospheric particles whose residence times are one year or more and that it is the dominant settling process for very small particles (1961). To approximate the effect of coagulation I have introduced an arbitrary correction to Link's values in Figure 41 by decreasing the fall time by 10 for particles of radius 0.01μ and requiring that the coagulation correction is zero for fall times of one year or less.

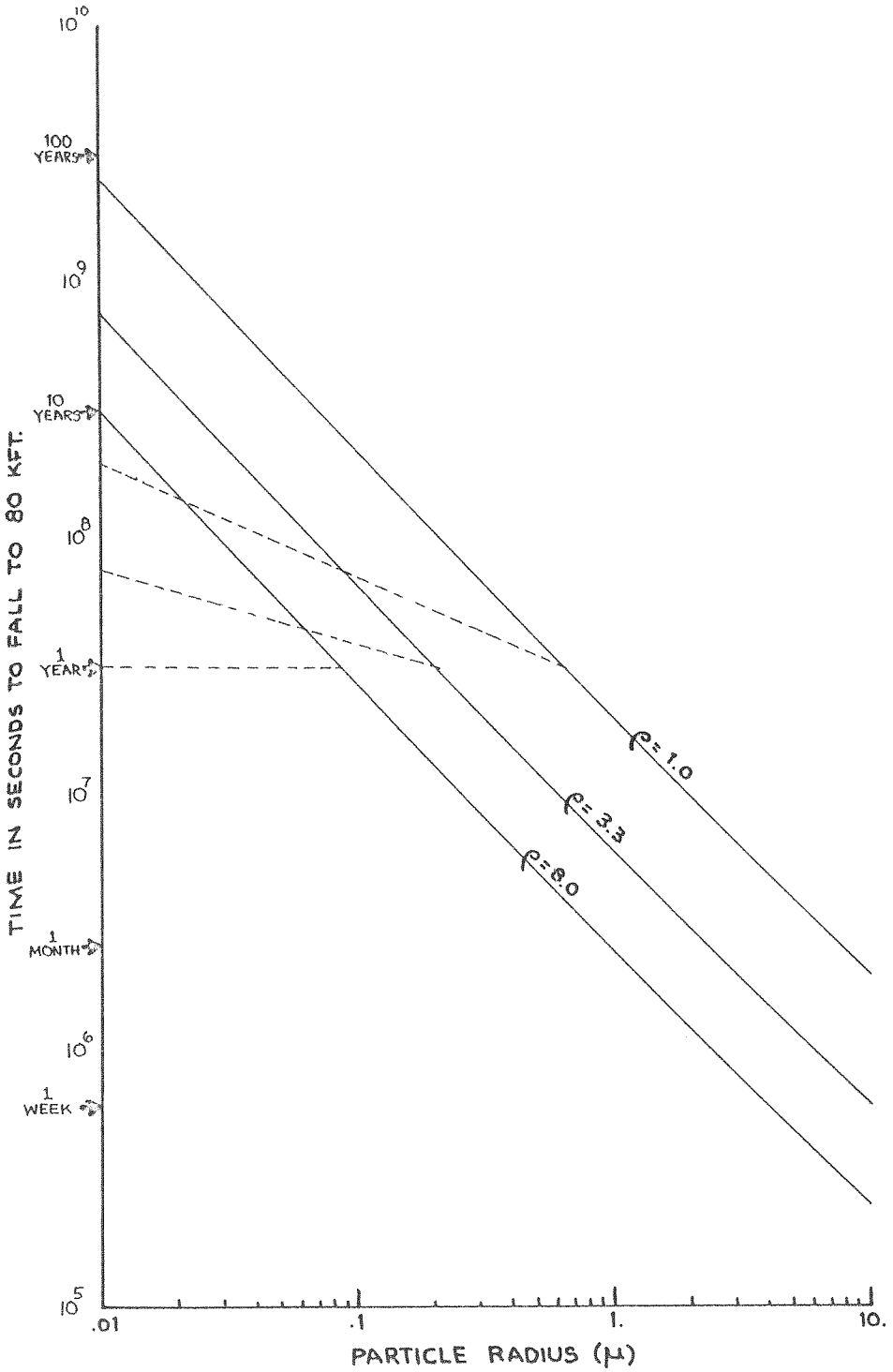

Figure 41

Time required for extraterrestrial particles to reach 80 kft. (Link, 1950).

The corrected fall times are shown as dashed lines in Figure 41. The magnitude of the correction was obtained by extrapolating the coagulation analysis given by Junge, Chagnon, and Manson; the correction represents a rough approximation that is adequate for this analysis.

I have used the corrected estimates of fall time to compute meteor influx rates, using Equation (38) and particle distribution C of Table 9. The results are given in Table 10 for meteoric particles of density 3.3 and 8.0. The rates given are in terms of particles per square meter per second at the top of the atmosphere. The relation of these influx rates to those obtained by other methods is shown in Figure 42, using a diagram taken from Best (1960). The abscissa is the logarithm of the particle radius in microns; the ordinate is the meteor influx rate in particles per square meter per second. I have included my estimated influx rate as a line marked "HAO." The sources of other estimates are designated on the diagram. Points marked "PARKIN" refer to meteor sampling measurements from an aircraft at 10,000 feet. The lines marked "ZODIACAL LIGHT" represent various estimates of the zodiacal light dust cloud. "V2" and "NRL" refer to rocket measurements using microphone counters and particle impactors. Satellite measurements are labelled "EXPLORER" and "SPUTNIK II." The point marked "LINK" refers to an observation of atmospheric absorption at the time of a lunar eclipse. Again, we should remember that the HAO observation refers to a non-unique interpretation of the scattering data; other possible interpretations would reduce the influx rates for particles of radius less than about 0.1 micron. We should also remember that the optical data provide only an upper limit, based on the assumption that all Mie particles above 80 kft. are of meteoric origin. Nevertheless the observations reported here provide a limiting estimate in a size range of particles too small to be measured by most other techniques.

Table 10. Meteoric Influx Rates

Particle radius a	Column density N'(a)	$\rho = 3.3$ Residence time T (sec)	$\rho = 3.3$ Influx rate F'	$\rho = 8.0$ Residence time T (sec)	$\rho = 8.0$ Influx rate F'
.02μ	4.1×10^{13}	6.2×10^{7}	6.6×10^{9}	3.2×10^{7}	1.3×10^{10}
.03	1.6×10^{12}	5.5×10^{7}	2.9×10^{8}	3.2×10^{7}	5.0×10^{8}
.04	1.6×10^{11}	5.0×10^{7}	3.2×10^{7}	3.2×10^{7}	5.0×10^{7}
.05	2.7×10^{10}	4.7×10^{7}	5.7×10^{6}	3.2×10^{7}	8.4×10^{6}
.06	6.2×10^{9}	4.5×10^{7}	1.4×10^{6}	3.2×10^{7}	1.9×10^{6}
.07	1.8×10^{9}	4.3×10^{7}	4.2×10^{5}	3.2×10^{7}	5.6×10^{5}
.08	6.2×10^{8}	4.1×10^{7}	1.5×10^{5}	3.2×10^{7}	1.9×10^{5}
.09	2.4×10^{8}	3.9×10^{7}	6.2×10^{4}	3.2×10^{7}	7.5×10^{4}
.1	1.0×10^{8}	3.8×10^{7}	2.6×10^{4}	2.8×10^{7}	3.6×10^{4}
.2	4.1×10^{5}	3.2×10^{7}	1.3×10^{2}	1.4×10^{7}	2.9×10^{2}
.3	1.6×10^{4}	2.1×10^{7}	7.6×10^{0}	8.9×10^{6}	1.8×10^{1}
.4	1.6×10^{3}	1.6×10^{7}	1.0×10^{0}	7.5×10^{6}	2.1×10^{0}
.5	2.7×10^{2}	1.3×10^{7}	2.1×10^{-1}	5.2×10^{6}	5.2×10^{-1}
.6	62	1.0×10^{7}	6.2×10^{-2}	4.2×10^{6}	1.5×10^{-1}
.7	18	8.8×10^{6}	2.0×10^{-2}	3.6×10^{6}	5.0×10^{-2}
.8	6.2	7.6×10^{6}	8.2×10^{-3}	3.1×10^{6}	2.0×10^{-2}
.9	2.4	6.8×10^{6}	3.5×10^{-3}	2.8×10^{6}	8.6×10^{-3}
1.0	1.0	6.1×10^{6}	1.6×10^{-3}	2.5×10^{6}	4.0×10^{-3}
1.1	.49	5.5×10^{6}	8.9×10^{-4}	2.2×10^{6}	2.2×10^{-3}
1.2	.24	5.1×10^{6}	4.7×10^{-4}	2.0×10^{6}	1.2×10^{-3}
1.3	.13	4.7×10^{6}	2.8×10^{-4}	1.9×10^{6}	6.8×10^{-4}
1.4	.071	4.4×10^{6}	1.6×10^{-4}	1.8×10^{6}	3.9×10^{-4}
1.5	.041	4.1×10^{6}	1.0×10^{-4}	1.6×10^{6}	2.6×10^{-4}
1.6	.024	3.7×10^{6}	6.5×10^{-5}	1.5×10^{6}	1.6×10^{-4}
1.7	.015	3.6×10^{6}	4.2×10^{-5}	1.4×10^{6}	1.1×10^{-4}

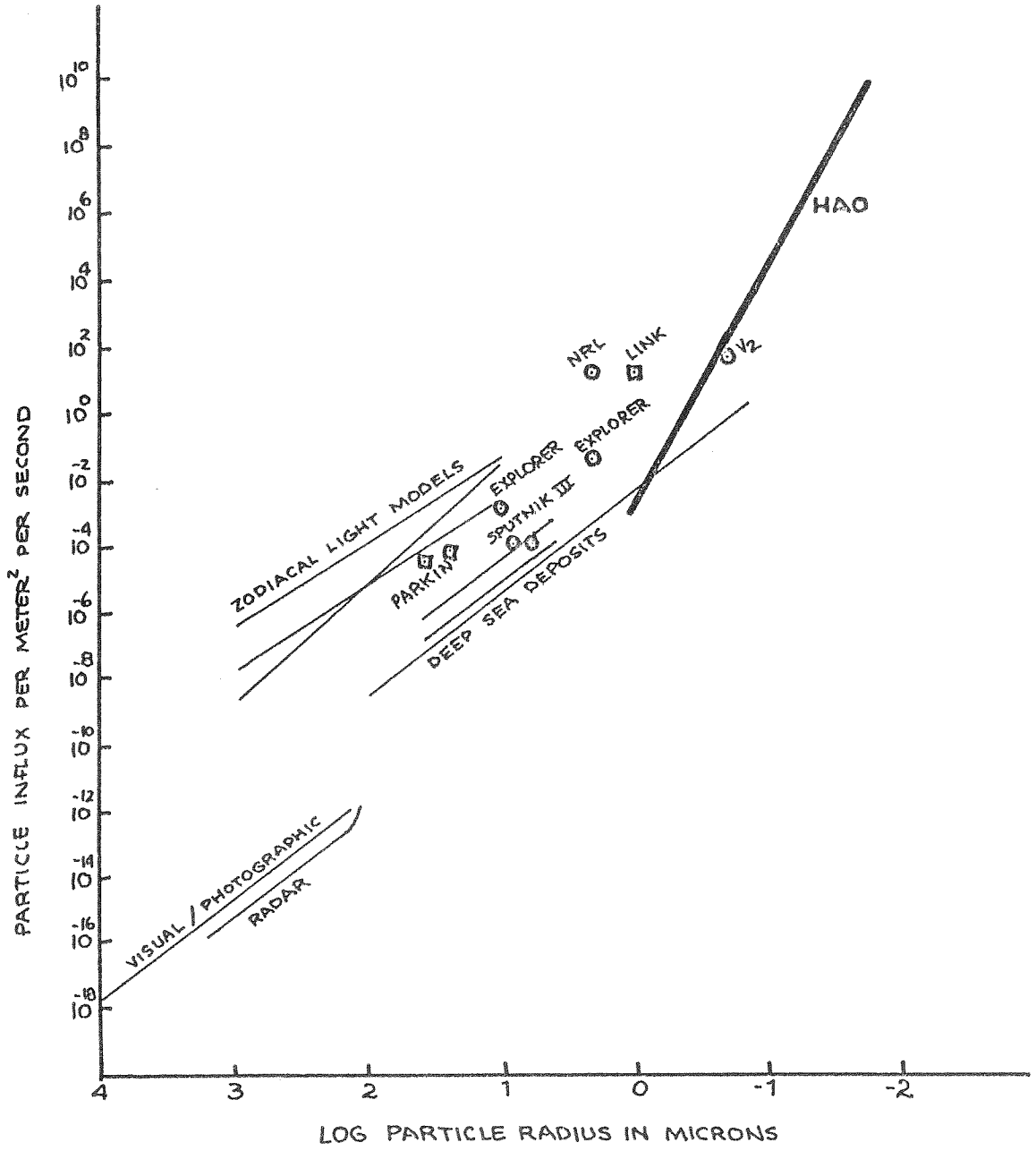

Figure 42

Meteoric influx rates derived from various estimates with an upper limit curve from the HAO Coronascope data.

CHAPTER VI

CONCLUDING REMARKS

Spectral observations of the brightness of the stratospheric solar aureole, obtained by a balloon flight in October 1960, were given in Chapter IV. The theoretical Rayleigh sky brightness was then computed for the conditions of each of the observed data points. The difference between the observed and Rayleigh brightness (called the residual sky brightness) was interpreted as due to scattering by spherical aerosols in the atmosphere above the point of observation. It was found that there was no unique particle size distribution that explained the spectral distribution of the residual sky brightness. Rather, a family of solutions was found to fit the data. The limits of possible distributions were delineated by varying the parameters in Junge-type size distributions and calculating the aureole brightness that would result from each model distribution. The size distributions that fit the observations were all steeper functions of particle radius than those given by sampling measurements, in the sense that relatively more small particles were indicated by the optical measurements than were predicted by the sampling data. Under the assumption that the aerosols were meteoric an upper limit to meteoric influx was then derived.

My thesis contains three results that I consider to be important. First, and most important, are the data themselves. They represent unique and photometrically accurate observations of the spectral distribution of the stratospheric aureole. They are well identified data that should be of value to scientists in several fields. To solar astronomers who wish to study the corona from high altitude the data give the first accurate measurement of stratospheric sky brightness near the sun. To

atmospheric physicists who wish to record the dayglow the Coronascope observations provide an absolute value of the stratospheric background sky brightness. And to physical meteorologists interested in aerosol distribution the data give new and reliable optical measurements that can be interpreted in terms of the stratospheric aerosol content. My method of interpretation is a first approximation; more powerful methods of Mie particle analysis could be applied to the data with promise of an improved solution.

Second, that a family of non-unique solutions was found which satisfied the observations is an enlightening result. There have been many interpretations of scattering observations that purport to explain the observations in terms of a "mean particle size" or a single particle distribution (Liller, 1960; Curcio, 1961). My result shows the possible error in such an interpretation.

Third, my interpretation of the residual sky brightness data indicates that the size distribution of stratospheric aerosols follows a much steeper function of radius than that usually accepted for the troposphere and the atmosphere as a whole. Allowing for the non-uniqueness of the Mie interpretation and for the inaccuracy of the data themselves, the Coronascope observations cannot be made to fit a size distribution of the form that has been proposed in the past. Previous estimates of the stratospheric aerosol distribution have been based solely on sampling measurements. I feel that the Coronascope observations offer the most reliable data to date on the distribution of sub-micron aerosols in the stratosphere. I look forward to the combination of the spectral data with the angular scattering data that Dr. Newkirk has analyzed. A particle interpretation based on the two sets of simultaneous data should eliminate some of the ambiguity in either part alone and give a highly accurate interpretation.

APPENDIX I

Glossary of Symbols

a	Particle radius (microns)
A	Albedo
A_c	Coulson albedo (for top of Rayleigh atmosphere)
A_k	Krinov albedo (for ground)
A_m	Mean albedo
Å	Angstroms
B	Brightness (ergs $cm^{-2}sec^{-1}steradian^{-1}$)
$B_\odot$	Brightness of the mean solar disk
$\mathcal{B}$	Zenith-corrected brightness ratio, = $\mu B/B_\odot$
c	Velocity of light
d	Interparticle distance
F	Flux (ergs sec^{-1})
F'	Meteor influx rate
h	Altitude, or height above sea level
H	Solar hour angle
I	Illuminance (ergs $sec^{-1}cm^{-2}$)
J	Source function
K	Coagulation coefficient
m	Refractive index
M	$\log_{10}e$
N	Volume density of particles (cm^{-3})
N'	Column density of particles (cm^{-2})
p	Atmospheric pressure
p_o	Atmospheric pressure at sea level
r	Distance from scattering particle to observer

$R_\odot$	Solar radius
S	Linear distance
t	Time
T	Residence time
x	Particle size parameter = $2\pi a/\lambda$
Z	Zenith angle
Z_o	Zenith angle of the sun
α	Polarizability
δ	Particle distribution coefficient
Δ	Solar declination
Θ	Scattering angle
κ	Scattering coefficient
λ	Wavelength (microns)
μ	Microns
μ	Cosine of zenith angle (Z)
μ_o	Cosine of solar zenith angle (Z_o)
ρ	Density (grams^{-1}cm^{-3})
σ_Θ	Angular Mie scattering cross section
τ	Optical depth
τ_o	Optical depth at sea level
ϕ	Azimuth angle
Φ	Geographic latitude
ω	Solid angle
$\omega_\odot$	Solid angle subtended by the sun at earth

REFERENCES

Armour Research Foundation 1956, Final Report on Contract AF 19(604)-1428.

Bates, D. R. and A. Dalgarno 1954, J.A.T.P., 5, 329.

Berg, O. E. 1955, J.G.R., 60, 271.

Best, G. T. 1960, Space Research, ed. H. Kallmann Bijl, (Amsterdam: North Holland Publ. Co.)

Boileau, A.R. 1960, Scripps Institute of Oceanography Report 60-32.

Born, M. and E. Wolf 1959, Principles of Optics, (New York: Pergamon Press).

Brandt, J. C. 1958, Ap. J., 128, 718.

Chamberlain, J. W. 1961, Physics of the Aurora and Airglow, (New York: Academic Press).

Chamberlain, J. W. and C. Sagan 1960, Planetary and Space Science, 2, 157.

Chandrasekhar, S. 1950, Radiative Transfer, (Oxford: Clarendon Press).

Cooper, R. H., J. A. Eddy, and G. A. Newkirk 1960, Astro-Geophysical Memorandum No. 142, High Altitude Observatory.

Coulson, K. L. 1959, Planetary and Space Science, 1, 277.

Coulson, K. L., J. V. Dave, and Z. Sekera 1960, Tables Related to Radiation Emerging from a Planetary Atmosphere with Rayleigh Scattering, (Berkeley, California: University of California Press).

Curcio, J. A. 1961, J.O.S.A., 51, 548.

Dalgarno, A. 1958, Ann. de Geophys., 14, 241.

Dave, J. V. and Z. Sekera 1959, J. Meteor., 16, 211.

Deirmendjian, D. 1955, Archiv. Meteor., Geophys. u. Bioklim., Series B., 6, 452.

Deirmendjian, D. 1957, Ann. de Geophys., 13, 286.

Deirmendjian, D. 1959, Ann. de Geophys., 15, 218.

Deirmendjian, D. and Z. Sekera 1956, J.O.S.A., 46, 565.

Duntley, S.C., A. R. Boileau, J. Gordon, and J. L. Harris 1960, Scripps Institute of Oceanography Report 60-12.

Evans, J. W. 1948a, High Altitude Observatory Special Report on AMC Contract W28-099 ac-364, April 1948.

REFERENCES (cont.)

Evans, J.W. 1948b, J.O.S.A., 38, 1083.

Fesenkov, V. G. 1955, Astronomicheskii Zhurnal, 32, 265. (Translated by E. R. Hope for Canada Defence Research Board, T-279-R, April 1958).

Fritz, S. 1949, J. Meteor., 6, 277.

General Mills, Inc. 1960, Final Report, Project Coronascope, GMI Report 2127.

Hart, B. 1960, Ladies' Home J., 77, No. 4, 107.

Hulbert, E. O. 1948, Naval Research Laboratory Report N-3257.

Hulst, H.C. van de 1952, in The Atmospheres of the Earth and Planets, ed. G. P. Kuiper, (Chicago: University of Chicago Press).

Hulst, H.C. van de 1957, Light Scattering by Small Particles, (New York: Wiley and Sons).

Junge, C. E. 1955, J. Meteor., 12, 13.

Junge, C. E. 1961, J. Meteor., 18, 501.

Junge, C. E., C. W. Chagnon, and J. E. Manson 1961, J. Meteor., 18, 81.

Junge, C. E. and J. E. Manson 1961, J.G.R., 66, 2163.

Kano, M. 1958, Pep. Met. Geophys. (Tokyo), 9, 163.

Krinov, E. L. 1960, reproduced in U. S. Air Force Handbook of Geophysics (New York: The Macmillan Co), from original reference in Russian, 1947.

Kunz, K. S. 1957, Numerical Analysis, (New York: McGraw Hill).

Larsen, S. H. H. 1959, Geofysiske Publikasjoner, 21, No. 4.

Liller, W. 1960, Ap. J., 132, 867.

Link, F. 1950, Bull. Astron. Inst. Czech., 2, 1.

Luckiesh, M. 1919, Ap. J., 49, 108.

Marion, F. 1874, Wonderful Balloon Ascents: or, the Conquest of the Skies, (New York: Scribner, Armstrong and Co.).

Middleton, W.E.K. 1960, J.O.S.A., 50, 97.

Mie, G. 1908, Ann. Physik, 25, 377.

REFERENCES (cont.)

Miley, H. A., E. H. Cullington, and J. F. Bedinger 1953, Trans. A.G.U., 34, 680.

Minnaert, M. 1954, The Nature of Light and Color in the Open Air, (New York: Dover Publications, Inc.).

Morosov, V. M. and I. S. Shklovsky 1956, Izv. A.N. U.S.S.R., Geophys. Ser. No. 4, 464.

Newkirk, G. A. 1956, J.O.S.A., 46, 1028.

Packer, D. M. and C. Lock 1951, Naval Research Laboratory Report 3713.

Penndorf, R. 1954a, Private Communication to G. A. Newkirk.

Penndorf, R. 1954b, J. Meteor., 11, 245.

Penndorf, R. 1956, Geophysical Research Paper No. 44, Geophysics Research Directorate.

Penndorf, R. 1960, Technical Report RAD-TR-60-10, Contract AF19(604)-5743, Geophysics Research Directorate.

Lord Rayleigh 1871, Phil. Mag., 41, 107, 274, 447.

Sekera, Z. 1957, J.O.S.A., 47, 484.

Sekera, Z. and J. V. Dave 1961, Ap.J., 133, 210.

Sekihara, K. and K. Murai 1961, Pap. Met. Geophys. (Tokyo), 12, 57.

Stakutis, V. J. 1960, in U. S. Air Force Handbook of Geophysics, (New York: The Macmillan Co.).

Svestka, Z. 1954, Bull. Astron. Inst. Czech., 5, 91.

Teele, R. P. 1936, National Geographic Society, Stratosphere Series, No. 2, The National Geographic Society-U.S. Army Air Corps Stratosphere Flight in the Balloon "Explorer II.", 133.

Tousey, R. and E. O. Hulbert 1947, J.O.S.A., 37, 78.

Volz, F. E. 1954, Ber. Deut. Wetterdienstes, No. 13, Band 2.

Volz, F. E. and K. Bullrich 1961, J. Meteor., 18, 306.

Volz, F. E. and R. M. Goody 1960, Blue Hill Meteorological Observatory Scientific Report No. 1, AF19(604)-4546.

Wallace, L. 1961, J.G.R., 66, 1585.